# STRUCTURE-BASED BAYESIAN COMPRESSIVE SENSING FOR THROUGH-THE-WALL RADAR IMAGING

BY

MOHAMMAD TAMIM ALKHODARY

A Dissertation Presented to the
DEANSHIP OF GRADUATE STUDIES

**KING FAHD UNIVERSITY OF PETROLEUM & MINERALS**
DHAHRAN, SAUDI ARABIA

In Partial Fulfillment of the
Requirements for the Degree of

**DOCTOR OF PHILOSOPHY**
**In**
ELECTRICAL ENGINEERING

May, 2017

KING FAHD UNIVERSITY OF PETROLEUM & MINERALS

DHAHRAN- 31261, SAUDI ARABIA

**DEANSHIP OF GRADUATE STUDIES**

This thesis, written by Mohammad Tamim Alkhodary under the direction of his thesis advisor and approved by his thesis committee, has been presented and accepted by the Dean of Graduate Studies, in partial fulfillment of the requirements for the degree of **DOCTOR OF PHILOSOPHY IN ELECTRICAL ENGINEERING.**

Dr. Ali A. Al-Shaikhi

Department Chairman

Dr. Salam A. Zummo

Dean of Graduate Studies

5/6/17

Date

Dr. Ali H. Muqaibel
(Advisor)

Dr. Tareq Al-Naffouri
(Co-Advisor)

azzedine zergue

Dr. Azzeddine Zerguine
(Member)

Dr. Abdulmalek Zidouri
(Member)

Dr. Maan Abdulgader Kousa
(Member)

In the name of God, the Compassionate, the Merciful

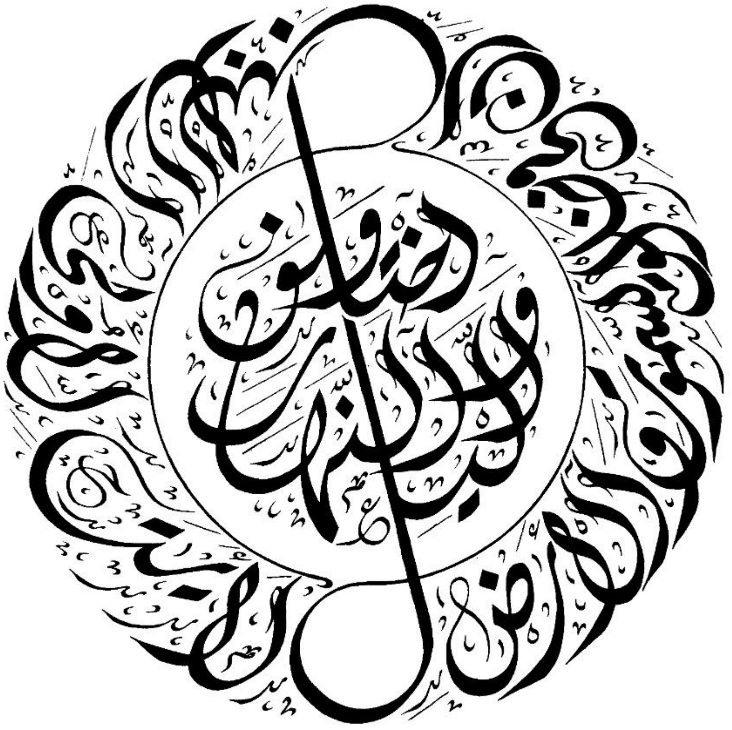

Indeed, in the creation of the sky and the earth and the alternation of the night and the day are signs for those of rationality.

Quran Verse (3:190)

*My beloved parents,*

*Sisters,*

*Brothers,*

# Acknowledgment

In the name of Allah, the Most Gracious, the Most Merciful

All praise is due to ALMIGHTY ALLAH; to whom belongs the vast dominion of the Universe. Peace and mercy be upon His Prophet who showed us the way of peace and real success in our lives and hereafter.

First and foremost, my thanks are due to ALMIGHTY ALLAH who blessed me with essential knowledge and patience to carry out this challenging work.

Secondly, I must acknowledge the continuous motivation and prayers of my beloved parents who have always been there to help me achieve major milestones in my life. I will never be able to reward in the slightest their endless support at every stage of my life. Dear Mother, I wish if words can express how much you mean to me, or how much I admire, appreciate, and feel thankful to you for everything you have given. Dear Father you mean so numerous things to me, an understanding heart, a source of strength and support, a constant readiness to help in a kind thoughtful wise and patient way.

I also acknowledge the love and the encouragement of my sisters and brothers who have helped me immensely in pursuing my studies despite being far away from them.

I would like to offer my indebtedness and sincere appreciation to my advisor Professor Ali Hussein Muqaibel. No words of thanks would be sufficient for his guidance, advice and support. Over the course of my master and PhD degrees, he was always available and ready for support, even on holidays and at his break hours. His advices have improved me in so many levels, personally, academically, professionally, scientifically, and linguistically. This work would not have seen the light without him.

I am full of gratitude to the virtues of my Co-advisor Professor Tareq Al-Naffouri, for his limitless support, guidance, caring and motivation that enlarged my competence on the field. I am thankful for his good cooperation shown over the whole period of my PhD program. His good communication and contribution led to the successful completion of this work.

Bundle of genuine gratitude to Professor Maan Kousa, a caring father have who generously supported me since the beginning of my study in KFUPM.

Special thanks are due to my thesis committee members, Professor Azzedine Zerguine, and Professor Abdelmalek Zidouri for all their cooperation and advice. They have been offering me valuable support and help over the course of my study.

My gratitude and thankfulness are extended to the Chairman of the Electrical Engineering department Dr. Ali Ahmad Al-Shaikhi, and to the Dean for Graduate Studies Prof. Salam Adel Zummo who have offered me a comfortable research environment and atmosphere, and have never hesitated to provide assistance whenever I asked.

I am greatly indebted to my friends Dr. Abdi Talib, Dr. Saleh Alawsh, and Dr. Mudassir Masood for their valuable time spent to support me with many memorable moments. I extend my thanks and appreciation to all my friends who helped me in one way or the other; I was indeed honored to know them.

Finally, I wish to acknowledge King Fahd University of Petroleum and Minerals for providing the various facilities, support and resources utilized in the preparation of this thesis.

Mohammad Tamim Alkhodary

# Contents

# List of Figures

# List of Tables

# List of Abbreviation and Acronyms

| | |
|---|---|
| BP | Basis Pursuit |
| BMP | Bayesian Matching Pursuit |
| BLUE | Best Linear Unbiased Estimator |
| CD | Change Detection |
| CS | Compressive Sensing |
| CSMP | Compressive Sensing Matching Pursuit |
| CRLB | Cramer-Rao Lower Bound |
| EM | Electromagnetic Wave |
| LASSO | Least Absolute Shrinkage and Selection Operator |
| LOS | Line of Sight |
| MP | Matching Pursuit |
| MAP | Maximum a Posteriori Probability |
| MMSE | Minimum Means Square Error |
| ME | Multipath Exploitation |
| MIMO | Multiple Input Multiple Output |
| OMP | Orthogonal Matching Pursuit |
| RI | Radar Imaging |

| | |
|---|---|
| ROMP | Regularized Orthogonal Matching Pursuit |
| SCR | Signal to Clutter Ration |
| SNR | Signal to Noise Ration |
| SR | Sparse Reconstruction |
| SFCW | Step Frequency Continuous Wave |
| SBBCS | Structured Based Bayesian Compressive Sensing |
| SABMP | Support Agnostic Bayesian Matching Pursuit |
| SAR | Synthetic Aperture Radar |
| TWI | Through the Wall Imaging |
| TWR | Through the Wall Radar |
| TWRI | Through the Wall Radar Imaging |
| UWB | Ultra-wide Band |
| URI | Urban Radar Imaging |
| IRI | Indoor Radar Imaging |
| VNA | Vector Network Analyzer |

# List of Symbols

| | |
|---|---|
| $\mathbf{V}_l$ | $\mathbf{V}_l = \mathbf{\Phi}_l \mathbf{\Psi}_l$ |
| $BW$ | Bandwidth of the signal |
| $\mathbf{\Psi}$ | Basis matrix of the radar signal |
| $\mathbf{\Psi}_l$ | Basis matrix of the radar signal at the $l$-th location |
| $\mathbf{\Psi}_{\mathcal{S}}$ | Columns of $\Psi$ selected by $\mathcal{S}$ |
| $\mathtt{C}$ | Covariance Matrix |
| $d$ | Front wall thickness |
| $\mathbf{G}$ | Gramian matrix |
| $\mathbf{I}_M$ | Identity Matrix of size $M \times M$ |
| $A$ | Length of the antenna aperture |
| $l$ | Locations index |
| $\mu(\mathbf{\Phi}, \mathbf{\Psi})$ | Mutual Coherence between the matrix $\mathbf{\Phi}$ and $\mathbf{\Psi}$ |
| $\mathbf{w}$ | Noise vector |
| $L$ | Number of antennas' location |
| $Q$ | Number of frequencies used in stepped-frequency radar |
| $N$ | Number of pixels in the scene |
| $N_t$ | Number of samples after sampling by Nyquest rate. |

| | |
|---|---|
| $G$ | Number of targets in the scene |
| $\boldsymbol{\alpha}$ | One dimensional version of the scene |
| $\mathbf{P}_{\mathcal{S}}^{\perp}$ | Orthogonal Complement Matrix of $\boldsymbol{\Psi}_{\mathcal{S}}$ |
| $n$ | Pixels index |
| $\mathscr{p}$ | Probability of success in Bernoulli process |
| $r_{l,q}$ | Radar return at the $l$-th location and the $q$-th frequency. |
| $\varepsilon_r$ | Relative permittivity |
| $\tau_{l,g}$ | Round-trip delay of the signal traveling from the $l$-th radar location to the $g$-th target. |
| $\mathcal{S}$ | Set of the non-zero elements in the scene |
| $c$ | Speed of light |
| $g$ | Targets Index |
| $\Delta f$ | The frequency step size in the SFCW signal |
| $\boldsymbol{\phi}_{\mathrm{l},i}$ | The $i$-th column of the matrix $\boldsymbol{\Phi}_l$, at the $l$-th location |
| $\boldsymbol{\psi}_{l,j}$ | The $i$-th column of the matrix $\boldsymbol{\Psi}_l$, at the $l$-th location |
| $\sigma_{\mathbf{w}}^2$ | Variance of the noise vector $\mathbf{w}$ |
| $\lambda$ | Wavelength of the center frequency |

# List of Publications

Over the course of the PhD program, the author has contributed to the following publications:

## Journal Publications

1. **Mohammad T. Alkhodary**, Ali H. Muqaibel "Efficient grouping technique for low mutual-coherence basis-matrix in radar imaging", IET Electronics Letters, November 2016.
2. Ali H. Muqaibel, Abdi T. Abdalla, **Mohammad T. Alkhodary**, Saleh A. Alawsh, "Through-the-wall radar imaging exploiting Pythagorean apertures with sparse reconstruction", Digital Signal Processing, Available online 4 August 2016.
3. A. H. Muqaibel, A. T. Abdalla, **M. T. Alkhodary**, S. I. Al-Dharrab, "Aspect Dependent Efficient Multipath Ghost Suppression in TWRI with Compressive Sensing", International Journal of Microwave and Wireless Technologies (Accepted).
4. **Mohammad T. Alkhodary**, Ali H. Muqaibel "Low Complexity Sparse Bayesian Estimation for UWB Radar Imaging" IET Radar, Sonar & Navigation (Under review).
5. A. H. Muqaibel, A. T. Abdalla, **M. T. Alkhodary**, Indoor Target Localization using Single Marginal Antenna with Virtual Radars Support, International Journal of Microwave and Wireless Technologies (Minor revision).
6. **Mohammad T. Alkhodary**, Ali H. Muqaibel "Cooperative Bayesian estimation for compressed through wall radar imaging", to be submitted to IEEE Transactions on Geoscience and Remote Sensing.
7. **Mohammad T. Alkhodary,** Entao Liu, Abdullatif Al-Shuhail, Ali-Muqaibel, James McClellan, Ali H. Muqaibel “Compressive Sensing Method for Microseismic-events Localization”, to be submitted to IEEE Geoscience and Remote Sensing Letters.

## Conference Publications

1. **Mohammad T. Alkhodary**; Salah Z. Hosny, Ali H. Muqaibel "Experimental Evaluation of UWB Indoor Radar Imaging", 2016 IEEE Asia-Pacific Conference on Applied Electromagnetics (APACE 2016).
2. **Mohammad T. AlKhodary,** Tarig Ballal, Tareq Y. Al-Naffouri "Low Sampling Technique for M-ary Multiple Access UWB Communication in Multipath Channel", to be submitted to ICUWB 2015
3. Saleh A. Alawsh; **Mohammad T Alkhodary**; Ali H Muqaibel, and Mohammad S. Sharawi "Experimental Evaluation of Coprime Sampler in Direction of Arrival Estimation". MECAP 2016 IEEE Middle East Conference on Antennas and Propagation, Beirut, Lebanon.
4. Kousa, Maan A.; Muqaibel, Ali H.; Williams, Doug; **Alkhodary, Mohammad T**.; Mayyala, Qadri, "Developing Electrical Engineering Course in an Active Cooperative Learning (ACL) Platform", 19th International Conference on Interactive Collaborative Learning (ICL2016), Belfast, UK.

## Previous Publications

1. Muqaibel, A.H.; **Mohammad T. Alkhodary**, "Practical application of compressive sensing to ultra-wideband channels," Communications, IET , vol.6, no.16, pp.2534,2542, November 6 2012
2. **Alkhodary, M.T.**; Muqaibel, A.H., "Practical implementation of compressive sensing to UWB signals," Information Science, Signal Processing and their Applications (ISSPA), 2012 11th International Conference on , vol., no., pp.1365,1370, 2-5 July 2012doi: 10.1109/ISSPA.2012.6310506

# Abstract

Full Name : Mohammad Tamim Alkhodary
Thesis Title : Structure-Based Bayesian Compressive Sensing for Through-the-Wall Radar Imaging
Major Field : Electrical Engineering
Date of Degree: May 2017

Through-the-wall radar imaging (TWRI) is the technology that utilizes electromagnetic waves to provide high-resolution images of objects from behind an obscured obstacle. Compressive sensing (CS) has been recently proposed to overcome many challenges in TWRI applications. This dissertation solves the root causes for the deterioration of the image-recovery performance of CS algorithms once applied to TWRI.

In sparse reconstruction framework, the basis-matrix of TWRI problem demonstrates high mutual-coherence, which is inversely proportional to the quality of the reconstructed image. The high mutual-coherence also weakens the noise immunity in the sparse reconstruction. This work proposes a technique for building a basis-matrix with low mutual-coherence which preserves the high-quality of the resultant image and enhances the performance in low signal to noise ratio (SNR).

Applying the existed CS-algorithms on TWRI is challenged by the complexity of the reconstruction process. Exploiting the structure of the basis-matrix of TWRI, a low complexity Bayesian-based estimation algorithm is proposed. The algorithm takes advantage of the statistics of the radar-return to find an approximate minimum mean-square error estimate of the radar-image. The developed algorithm leverages the correlation between the antenna element of the synthetic aperture radar (SAR) to enhance the reconstruction performance. Furthermore, the algorithm enables sharing statistical information about the scene between the antenna for eliminating the effect of multipath cause by walls.

For evaluation of the proposed algorithm, a TWRI MATLAB$^{\copyright}$-based simulator is developed. The simulator includes most of the TWRI effects based on state-of-the-art models. Additionally, a practical SAR system was built which is equipped with ultra-wideband (UWB) antennas. The system is used to provide realistic data for algorithm evaluation.

The results out of the simulated and the measured data show that the developed algorithms outperform other known algorithms in the literature, with 56% enhancement at SNR=0dB with much less processing time.

# ملخص الرسالة

**الاسم الكامل** : محمد تميم الخضري

**عنوان الرسالة** : الاستشعار المضغوط المبني على نظرية بايزن والمستغل للتركيبة النمطية لمصفوفة الأساس لتقنية التصوير الراديوي من خلال الحائط

**التخصص** : الهندسة الكهربائية

**تاريخ المناقشة** : مايو 2017

يُعرّف التصوير الراديوي عبر الجدار بأنه التكنولوجيا التي تستخدم الموجات الكهرومغناطيسية لتزويد صور عالية الدقة للأجسام من وراء حواجز معتمة. اقتُرحت مؤخرا تقنية الاستشعار المضغوط للتغلب على العديد من التحديات في تطبيقات التصوير الراديوي. إن هذه الأطروحة تبحث وتحل عن الأسباب الجذرية لتدهور أداء بناء الصور في خوارزميات الاستشعار المضغوط.

في إطار إعادة البناء المتناثر، فإن مصفوفة الأساس لإشارات التصوير الراديوي تُظهر نمطاً بنائياً مما يؤدي إلى مشكلة تدعى ارتفاع الترابط المتبادل بين أعمدة المصفوفة. وهذه المشكلة تتناسب عكسياً مع جودة الصورة التي سيتم بناؤها. كما أن ارتفاع الترابط المتبادل يضعف مناعة خوارزمية البناء ضد الضوضاء في عملية البناء. إن هذا العمل يقترح خوارزمية لبناء مصفوفة أساس ذات ترابط متبادل منخفض مما يحافظ على جودة الصورة الناتجة ويعزز الأداء عندما تكون نسبة الإشارة إلى الضوضاء منخفضة.

إن من التحديات في خوارزميات الاستشعار المضغوط هو تعقيد عملية بناء الصور. باستغلال التركيبة النمطية لمصفوفة الأساس في التصوير الراديوي، يقترح هذا العمل خوارزمية مبنية على نظرية بايزن وتتميز بأنها سهلة وغير معقدة. إن الخوارزمية المقترحة تستفيد من البيانات الإحصائية الموجودة في إشارات الرادار مما يؤدي إلى بناء صورة بأقل خطأ ممكن. وتستفيد الخوارزمية المقترحة من العلاقة بين الهوائيات المستخدمة في الرادار وذلك لتعزيز أداء بناء الصورة. علاوة على ذلك، تُمَكن الخوارزمية من تبادل المعلومات الإحصائية بين الهوائيات من أجل القضاء على تأثير تعدد المسيرات والناتج عن الجدران المحيطة بالمشهد.

لتقييم الخوارزمية المقترحة، تم تطوير جهاز محاكاة، ويتضمن هذا الجهاز معظم الآثار الحقيقة في التصوير الراديوي والمبنية على الأبحاث الحديثة. بالإضافة إلى ذلك، تم بناء نظام تصوير راديوي عملي مجهز بهوائيات ذات نطاق عريض جدا. ويستخدم النظام لتوفير بيانات واقعية لتقييم الخوارزميات المقترحة في هذ العمل. تبين النتائج من البيانات المبنية على المحاكاة والبيانات المستخرجة من الجهاز العملي أن الخوارزميات المقترحة تتفوق على الخوارزميات المعروفة الأخرى في أدبيات البحث.

> “*To make any future that we dreamt up real requires creative scientists, engineers, and technologists to make it happen. If people are not within a midst dreaming about tomorrow with the capacity to bring tomorrow into the present, then the country might just recede back into a cave*”
>
> Neil deGrasse Tyson

# Chapter 1

# Introduction

The broad scope of this dissertation is a blend of two research areas: compressive sensing (CS) and through-the-wall radar imaging (TWRI). The former is a mathematical framework which allows recovering sparse signals from linear underdetermined systems of equations. The latter is a branch of radar imaging aims to image targets behind obscured barriers using electromagnetic modality. CS and TWRI have been a very active area of research and developments for the past decades. The capabilities of TWRI are highly desirable for variety of civilian and military applications such as fire-crises and rescue missions, emergency relief, and invasion operations [1–7]. Although, the indication TWRI ranges from determining building layouts, showing the interior of a building, reveal movements, etc. However, the context of imaging in this work is to determine the size, location, and the reflectivity of targets behind obscured barrier.

Several challenges are encountered in TWRI environment; including complex multipath and rich scatterings, wall wave blockage, shadowing, and target obstructions. These challenges have conventionally hindered the resolution quality and the efficiency of the imaging system. With the emerge of CS theory, the attention of TWRI researches was shifted towards projecting the challenges of TWRI on CS and sparse reconstruction (SR) scheme.

Applying CS on TWRI may raise some other concerns, like complexity, noise immunity, and the compression ratio at the sensing phase. In addition, most of CS algorithms, used in the literature [2, 8–33], rely only on the sparsity information of the signal. Our aim in this research is to design a Bayesian-based CS algorithm that overcomes the implication of applying CS on TWRRI. Moreover, it promotes sparsity and the statistical information of the acquired signal with emphasis on the correlation between the antennas in TWRI system. In essence, we utilize the structure of the sensing matrix and the prior statistical information embedded in the radar's return to aid sparse reconstructions of the radar image. Only a small percentage of data volume, that is required in conventional techniques, is used to produce high-resolution images. The algorithm provides the minimum mean square error estimate of the scene with low computational complexity.

The performance is evaluated over simulated and experimental data. The experimental data was obtained by several experiments in realistic TWRI scenarios. Results show superior performance over existed CS-based algorithms, even in the existent of noise and severe multipath.

## 1.2 Dissertation Contribution

The contributions of this dissertation can be categorized into two perspectives. The first involves in radar imaging mechanism and image reconstruction. The second is the development of the Bayesian-based algorithm. In the following, we list the main contributions with their corresponding publications:

1. From the perspective of image reconstruction mechanism:
    - This dissertation proposes a novel imaging technique for the synthetic aperture radar (SAR). This technique forms an inverse problem at each antenna element in the SAR array. The inverse problem can be solved either

independently or cooperatively using information from other antenna elements in the array [66, 68, 69].

- An efficient grouping technique for building a basis-matrix for radar imaging which demonstrates a low mutual-coherence value is proposed. The resultant basis-matrix preserves the quality of the radar-image and enhances the noise immunity of the system [68].

2. From the perspective of the algorithm development:

- By exploiting the structure of the basis-matrix, a low complexity Bayesian-based estimation algorithm is proposed. The algorithm takes advantage of the statistic of the radar-return to find the minimum mean-square error estimate of the radar-image. The low complexity is achieved by utilizing the block-matrix-inversion formula to execute the algorithm in an order-recursive manner [66].
- Further simplifications are achieved by using the exponential-sum formula to find the correlation between the columns of the basis-matrix [66].
- A cooperative technique for sharing statistical information between antenna elements in the SAR array is proposed. This technique leverages the correlation between the antenna elements. Consequently, it enhances the

performance of the image recovery, and dramatically reduces the effects of multipath [69].

- The above simplifications reduce the complexity of TWRI devices and hence reduces its overall cost. In addition, it provide instantaneous results make the which is highly desirable for TWRI applications.

As a by-product of this work, the following are some contribution to the research community:

- MATLAB$^{©}$-based TWRI simulator was developed. The simulator uses state-of-the-art TWRI models for modelling the various effects induced by TWRI environments. Including, front wall reverberation, side-walls multipath effects, target-to-target interaction, etc.

  The simulator allows the user to choose from different indoor phenomena to be included in the resultant radar's return. The simulated gives options to either generate radar images using conventional algorithms such as DSB, CS-based algorithms, or by the Bayesian-based algorithms that are developed in this work.

- Experimental SAR platform was developed to validate the algorithms and the techniques developed in this dissertation. The platform was used to generate bank of practical data for different radar imaging scenarios [70]. The data will be made available online for researchers of interest.

## 1.3 Methodology

To achieve its objectives, the work of this dissertation starts by addressing the conventional and the CS-based TWRI algorithms. The performance of the developed Bayesian-based algorithms was compared against the most popular algorithms in the literature, and for different practical scenarios.

In order to evaluate the algorithm performance, an ideal radar imaging system was designed. The system includes a synthetic aperture radar (SAR) and a scene of several targets with different reflectivity coefficients [71–73]. It is considered as an ideal scenario for the radar imaging system, and it acts as a benchmark for error performance. All developed algorithms in this dissertation are tested firstly on the ideal case. Practical aspects of radar imaging and through-the-wall radar imaging are then added gradually to the system in order to evaluate the algorithm empirical performance. These practical aspects include: additive white Gaussian noise (AWGN), multipath caused by walls and by target-to-target interactions, etc.

MATLAB©-based simulator for TWRI was built in order to generate the radar's return for different scenario. The simulator is based on the state-of-the-art modeling of TWRI [74]. This includes wall-multipath [75], wall reverberation [76], extended targets [77–79]. The simulator is capable of generating the TWRI image via conventional beamforming technique [9, 71, 80], CS-based technique [11, 14, 68, 75, 81–85], and via the developed CS Bayesian-based algorithm that is developed by this dissertation [66, 69, 86].

In addition to TWRI-simulator, a realistic ultra-wideband (UWB) SAR system was built and facilitated with UWB antenna. This system was used to image targets in different real-life scenarios. The developed algorithms were tested and validated over all realistic SAR returns. More detailed results are shown in Chapters 4-6.

Two performance criteria are used to evaluate the developed algorithms. The Normalized Mean-Squared Error (NMSE) is used to measure the reconstruction error as the amounts for the deviation between estimated and the true image vector [14, 6, 87, 88]. NMSE, measures the amount of error relative to the signal power. When NMSE exceeds one, this means that the error is greater that the signal power, hence targets will not be correctly identified, unless additional signal processing technique is invoked [14, 15].

The second criterion is the processing time to measure the complexity of the developed algorithms. In addition to the above criterion, the developed algorithms were validated over realistic data.

.

## 1.4 Notations

We denote matrices with uppercase bold-face Greek letters (e.g.,$\mathbf{\Psi}$), vectors with small-case bold-face letters (e.g., $\boldsymbol{\alpha}$), and scalars with small-case letters (e.g., $l$ ). The calligraphic letters are used for sets (e.g., $\mathcal{S}$, or $\mathcal{A}$). The bold calligraphic letters are reserved for set of sets (e.g., $\boldsymbol{\mathcal{S}}$). To refer to the $l$-th column of the matrix $\mathbf{\Psi}$, we use $\boldsymbol{\psi}_l$, while $\mathbf{\Psi}_{\mathcal{S}}$ indicates a sub-matrix formed by the columns of $\mathbf{\Psi}$ such as $\{\boldsymbol{\psi}_{s_i} : s_i \in \mathcal{S}\}$

"*Bayes' Theorem transforms the probabilities that look useful (but are often not), into probabilities that are useful. It is important to note that it is not a matter of conjecture; by definition a theorem is a mathematical statement has been proven true. Denying Bayes' Theorem is like denying the theory of relativity.*"

James V. Ston
University of Sheffield, UK.

# Chapter 2

# Technical Background

This chapter highlights the technical background materials on which this dissertation is built. The chapter presents the essentials of TWRI and related CS theories. Besides, the rationale of using CS to TWRI is elaborated. The effect of multipath due to the scattered EM waves from the surrounding walls and nearby targets on the image reconstruction and interpretation is delineated herein.

## 2.1 Basics of Compressive Sensing

Theory of CS states that a sparsely representable signal can be reconstructed using very few number of measurements compared to the signal dimension [34, 37, 46, 108–110]. In order to briefly review the main ideas of CS, consider the following finite length, discrete time signal $\mathbf{x} \in \mathbb{R}^M$. Representing a signal involves the choice of a dictionary, which is the set of elementary waveforms used to decompose the signal. Sparsity of a signal is defined as the number of non-zero elements in signal under some representation. A signal is said to have a sparse over a known dictionary $\Psi = [\boldsymbol{\psi}_1, \ \boldsymbol{\psi}_2, \dots, \boldsymbol{\psi}_N]$, with $\boldsymbol{\psi}_n \in \mathbb{C}^M$ , if there exists a sparse vector $\boldsymbol{\alpha} = [\alpha_1, \alpha_2, \dots, \alpha_N \,]^T$, such that

$$\mathbf{x} = \sum_{n=1}^{N} \boldsymbol{\psi}_n \alpha_n. \tag{2-1}$$

The above summation can be represented by a matrix form as:

$$\mathbf{x} = \boldsymbol{\Psi}\boldsymbol{\alpha} \tag{2-2}$$

where $\|\boldsymbol{\alpha}\|_{\ell_0} = G \ll M$. The $\ell_0$-norm used here simply counts the number of non-zero components in $\boldsymbol{\alpha}$. A dictionary that leads to sparse representations can either be chosen as a prespecified set of functions or designed by adapting its content to fit a given set of signal examples [89, 111]. Choosing a prespecified transform matrix is appealing because it is simpler. In this dissertation we will only consider prespecified dictionaries.

The framework of CS aims at recovering the unknown vector $\mathbf{x}$ from an underdetermined system of linear equations

$$\mathbf{y} = \mathbf{\Psi}\mathbf{x} \tag{2-3}$$

where $\mathbf{y} \in \mathbb{C}^K$is the received data vector and matrix $\mathbf{\Phi} \in \mathbb{C}^{K\times M}$ with $G < K < N$ is the sub sampling matrix or sensing matrix due to the number of rows is less than the number of columns. Since $K < N$, this system has more unknowns than equations, and thus the system is not invertible. In particular, equation (2-3) has infinitely many solutions. Among the infinitely many solutions of (2-3), we are only interested in the sparsest one. If we know a priori that our original signal $\boldsymbol{\alpha}$ is sparse, then the most natural choice will be to find a vector with least non-zero entries,

$$\min_{\boldsymbol{\alpha}} \|\boldsymbol{\alpha}\|_{\ell_0} \quad \text{such that } \mathbf{y} = \mathbf{\Phi}\mathbf{\Psi}\boldsymbol{\alpha} \tag{2-4}$$

The above equation is an NP-complete problem, which basically means that it requires an exhaustive search and, in general, it is not a feasible problem.

Special cases of interest for convexity are all the $\ell_p$-norms for $p \geq 1$. Among them, $\ell_1$- norm is very interesting and popular due to its tendency to sparsify the solution.

Chen et al. [112] stated that the sparse signal $\boldsymbol{\alpha}$ can be recovered from only $K = \mathcal{O}\left(G \log \frac{N}{G}\right)$ linear non-adaptive measurements by solving the following relaxation problem of (2-4)

$$\min_{\boldsymbol{\alpha}} \|\boldsymbol{\alpha}\|_{\ell_1} \quad \text{such that } \mathbf{y} = \boldsymbol{\Phi}\boldsymbol{\Psi}\boldsymbol{\alpha} \tag{2-5}$$

where $\|\boldsymbol{\alpha}\|_{\ell_1} = \sum_n |\alpha_n|$. Several methods are available in the literature to solve the optimization problem in (2-5). The $\ell_1$-minimization is a convex problem and can be recast as a linear program (LP)[34]. This is the foundation for the Basis Pursuit (BP) techniques [37, 112]. Alternatively, greedy methods, known as Matching Pursuit (MP), can be used to solve (2-5) iteratively. The design of reconstruction algorithms to efficiently and accurately solve (2-5) is an open problem which is currently very topical in the scientific community.

Another problem in CS consist of designing a convenient measurement matrix $\boldsymbol{\Phi}$ such that salient information in any compressible signal is not damaged by the dimensionality reduction. Work on CS thus far assumed that $\boldsymbol{\Phi}$ is drawn at random, which simplifies its theoretical analysis, and also facilitates a simple implementation [113]. The CS reconstruction performance can be substantially improved by optimizing the choice of $\boldsymbol{\Phi}$ [114]. In general, the relationship between the sensing matrix $\boldsymbol{\Phi}$ and the dictionary $\boldsymbol{\Psi}$ affects the number of measurements required to reconstruct a sparse signal. Almost all theory of CS is based on the assumption that $\mathbf{V} = \mathbf{\Phi\Psi}$ is the concatenation of two orthogonal matrices. These theories follow the uncertainty principle which says that a signal cannot be sparsely represented both in $\mathbf{\Phi}$ and $\mathbf{\Psi}$ [114]. This claim depends on the similarity between $\mathbf{\Phi}$ and $\mathbf{\Psi}$. A rough characterization of the degree of similarity between the sparsity and measurement systems is given by the mutual coherence, which is given by,

$$\mu(\mathbf{\Phi}, \mathbf{\Psi}) = \min_{\substack{i,j \\ i \neq j}} \frac{\left|\boldsymbol{\phi}_i^{\mathrm{H}} \boldsymbol{\psi}_j\right|}{\|\boldsymbol{\phi}_i\|_{\ell_2} \left\|\boldsymbol{\psi}_j\right\|_{\ell_2}} \tag{2-6}$$

In other words, $\mathbf{V}$ is desired to have columns $\mathbf{v}_n, n = 1,2,\dots,N$ with small correlations. An explicit example of matrices which have small coherence is the concatenation of the Identity and Fourier matrices.

Another suitable way to describe the mutual coherence is to compute the Gramian matrix $\mathbf{G} = \mathbf{V}^T\mathbf{V}$, using the matrix $\mathbf{V}$ after normalizing each of its columns. The mutual coherence, in this case, is given by the off-diagonal entry of $\mathbf{G}$ with largest magnitude.

On the other hand, another criterion for evaluating the quality of a CS matrices that are nearly orthonormal, is the restricted isometry property (RIP) introduced in [115] by Candes and Tao (which they initially called the uniform uncertainty principle). RIP is a sufficient condition on $\mathbf{V}$ for exact recovery of a G-sparse $\boldsymbol{\alpha}$.

The matrix $\mathbf{V}$ satisfies RIP of order $s \in \mathbb{N}$, $s < N$, if there exist an isometry constant $0 < \delta_s < 1$ such that

$$(1 - \delta_s)\|\boldsymbol{\alpha}\|_{\ell_2}^2 \leq \|\mathbf{V}\boldsymbol{\alpha}\|_{\ell_2}^2 \leq (1 + \delta_s)\|\boldsymbol{\alpha}\|_{\ell_2}^2 \tag{2-7}$$

holds for all $s$-sparse vectors. $\delta_s$ is the smallest number satisfying (2-7). However, working with the RIP condition is much more complex compared to the simple coherence concept since for a given matrix checking the validity of RIP condition is an NP-complete problem itself.

Current CS theory only applies when the dictionary is an orthonormal basis, or when the columns of $\mathbf{V}$ are extremely uncorrelated. However, there are numerous practical examples in which there exist coherence between the sparsifying basis and sensing matrix. Sparsity is sometimes expressed in terms of an overcomplete dictionary, i.e., $\boldsymbol{\Psi}$ has many more columns than rows $(M < N)$ [112], which inevitably generates coherence between dictionary's wave- forms. It was shown in [116] showed that CS and recovery via $\ell_1$-norm minimization is also viable in the context of overcomplete and coherent dictionaries.

Nevertheless, the projection matrix **V** in the context of CWSF radar image, demonstrate high mutual coherence. Its columns are highly correlated. In Chapter 3 we propose a technique that reduces the mutual coherence of the matrix **V**, and lower the complexity of the reconstruction algorithm.

"*Coherence is in some sense a natural property in the compressed sensing framework, for if two columns are closely correlated, it will be impossible in general to distinguish whether the energy in the signal comes from one or the other*"[116].

Emmanuel Jean Candès
Stanford University

# Chapter 3

# Structure Based Grouping Technique for Low Mutual-Coherence Basis-Matrix

This chapter proposes a technique and methodology that are crucial for the development of the Bayesian-based algorithm in the succeeding chapters. Successful implementation of SR is tied to two conditions: sparsity representation of the system, and low mutual-coherence (MC) of the basis-matrix [114]. The former is easy to meet in radar imaging (RI), but the latter is challenging, especially for high-resolution RI [1, 10, 22]. High MC deteriorates the noise immunity of the system, and eventually ruins the reconstruction quality. Since the high MC of the basis-matrix in RI systems is observed for pixels that are laying in the same distance from the radar location [114], in this chapter we group those pixels into one representative pixel with a time delay equals to the average. Then, a new basis-matrix based on the representative pixels is generated. The new basis-matrix has a low MC value and hence provides the system with high noise immunity. In addition, the size of the new basis-matrix is smaller than the original one which reduces the computation requirements in the SR-algorithms.

## 3.1 Signal and System Model

Consider a synthetic aperture radar with monostatic configuration. As depicted in Figure 3-1, the radar illuminates the scene from $L$ locations by step frequency continuous wave (SFCW) signals with frequency bins $f_q$ for $q = 1,2,\dots,Q$. The illuminated scene is divided into $N = N_x N_y$ pixels, where $N_x$ and $N_y$ are the number of pixels in the crossrange and in the downrange respectively. If the scene contains $G$ targets, the frequency representation of the radar output at the $l$-th location corresponding to the $q$-th frequency , $f_q$, can be expressed as

$$r_{l,q} = \sum_{g=1}^{G} \sigma_g \exp\left(-j2\pi f_q \tau_{l,g}\right) + w_{l,q} \qquad (3\text{-}1)$$

where $\sigma_g$ is the reflection coefficient of the $g$-th target, and $\tau_{l,g}$ is the round-trip delay of the signal traveling from the $l$-th radar location to the $g$-th target. At the $l$-th location and the $q$-th frequency, $w_{l,q}$ is complex additive white Gaussian noise with zero mean and variance $\sigma^2_{w_{l,q}}$.

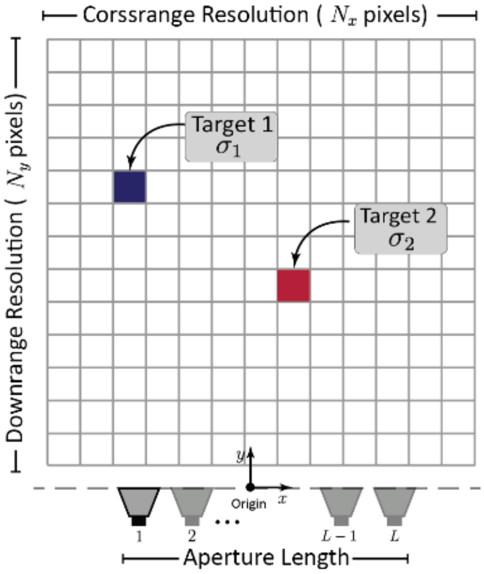

*Figure 3-1 Scene-setup and the radar system model.*

Considering all received frequencies $f_q$ for $q = 1,2,\dots,Q$, the variables of (3-1) can be put in a matrix form as

$$\mathbf{r}_l = \mathbf{\Psi}_l \boldsymbol{\alpha} + \mathbf{w}_l \qquad (3\text{-}2)$$

where the vector $\mathbf{r}_l$ represents the returns for all frequencies at the $l$-th location. $\boldsymbol{\alpha}$ is the one-dimensional representation of the radar-image at the $l$-th location with length of $N$ elements "or pixels". The vector $\mathbf{w}_l$ represents the additive white Gaussian noise, $\mathbf{w}_l \sim \mathcal{N}\left(0, \sigma_{w_l}^2 \mathbf{I}_Q\right)$.

The basis-matrix $\mathbf{\Psi}_l$ is the basis for the received vector $\mathbf{r}_l$ with dimension of $Q \times N$, i.e., the number of columns equal to the total number of pixels $N$, and the number of rows equal to the number of transmitted frequencies $Q$. Each column in the matrix represents the contribution of its corresponding pixel to the received vector $\mathbf{r}_l$. The elements of the $q$-th row and $n$-th column of $\mathbf{\Psi}_l$ is given by

$$(\mathbf{\Psi}_l)_{q,n} = \exp\left(-2\pi j f_q \tau_{l,n}\right) \tag{3-3}$$

where $\tau_{l,n}$ is the round trip time delay between the $l$-th location and the $n$-th pixel. In radar imaging, we are interested in recovering $\boldsymbol{\alpha}$ from $\mathbf{r}_l$.

For high quality RI, the number of illuminated frequencies is smaller than the number of pixels, i.e., $Q \ll N$, hence, the inverse problem in (3-2) is underdetermined with many solutions. In RI, the scene-vector $\boldsymbol{\alpha}$ is a sparse vector, thus, CS is a good candidate for solving (3-2). However, due to high MC, of the basis-matrix, CS-algorithms fail in recovering $\boldsymbol{\alpha}$, even at a negligible noise level. In fact, the value of MC, which represents the maximum value of the off-diagonal *Gramian matrix* $\mathbf{\Psi}_l^{\mathrm{H}}\mathbf{\Psi}_l$, is very close to one for the normalized high resolution radar-image. For instance, Figure 3-2, shows an example of *Gramian matrix* $\mathbf{\Psi}_l^{\mathrm{H}}\mathbf{\Psi}_l$

for a radar image of $41 \times 41$ pixels, where the intensity of the color represents the value of the columns correlation. The value of MC, denoted by $\mu(\mathbf{\Psi}_l)$, for this example is $\mu(\mathbf{\Psi}_l) = 1$, which explains why Figure 3-2 does not show any diagonality.

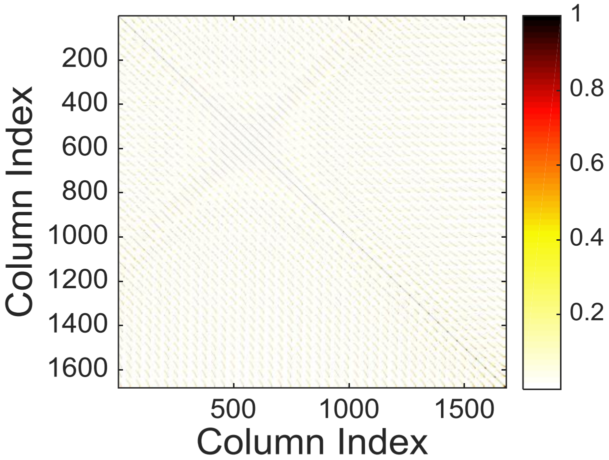

Figure 3-2 Normalized Gramian matrix $\boldsymbol{\Psi}_l^H\boldsymbol{\Psi}_l$ (columns' correlation of the full matrix $\boldsymbol{\Psi}_l$), $\mu(\boldsymbol{\Psi}_l) = 1$.

A common turn to go around this challenge, is to vertically concatenate the return vector $\mathbf{r}_l$ and the basis-matrix $\mathbf{\Psi}_l$ for all radar locations, then randomly select some rows from the concatenated version [1, 22]. The scene-vector $\boldsymbol{\alpha}$ remains intact after the concatenation process as it is not a function of the radar location. Although, CS-algorithm would successfully recover $\boldsymbol{\alpha}$ from the concatenated problem, nevertheless, the concatenated matrix still preserves a relatively high MC value, which makes the problem susceptible to noise. In addition, the large concatenated basis-matrix requires more computations in SR-algorithms.

## 3.2 Grouping Technique for Low Mutual-Coherence Matrix

We design a new basis-matrix, $\bar{\boldsymbol{\Psi}}_l$, at each radar location with low $\mu(\boldsymbol{\Psi}_l)$. We start by analysing the mutual-correlation of the columns of $\boldsymbol{\Psi}_l$ as

$$\begin{aligned}\boldsymbol{\psi}_i^{\mathrm{H}}\boldsymbol{\psi}_k &= \sum_{q=1}^{Q} \exp\left(2\pi j f_q \tau_i\right) \exp\left(-2\pi j f_q \tau_k\right)\\ &= \sum_{m=\eta}^{\zeta} \exp\left(2\pi j m \Delta f(\tau_i - \tau_k)\right) \qquad (3\text{-}4)\\ &= \frac{a^{\zeta-1} - a^{\eta}}{a-1} \text{ for } \tau_i \neq \tau_k\end{aligned}$$

where $\Delta f$ is the frequency step size in the illuminated SFCW signal, $\eta = f_1/\Delta f$, $\zeta = f_Q/\Delta f$, and $a = \exp\left(2\pi j \Delta f(\tau_i - \tau_k)\right)$.

The MC of the matrix $\boldsymbol{\Psi}_l$ depends on the delay difference between the columns $(\tau_i - \tau_k)$, i.e. the larger the difference, the less the MC is. Accordingly, the new basis matrix $\bar{\boldsymbol{\Psi}}_l$ is built by grouping the columns of small delay-difference, then we replace them with a new column of a delay equal to the average-delay of the group.

Let $\mathcal{T}_l = \{\tau_{l,i}: \tau_{l,i} \leq \tau_{l,i+1}\}, i \in \{1, \dots, N\}$ be a set of all delays in the basis-matrix $\boldsymbol{\Psi}_l$. We divide $\mathcal{T}_l$ into disjoint subsets, $\mathcal{T}_{l,t}$, that groups the delays with mutual difference less than a given threshold, $\gamma$. The value of $\gamma$ controls the number of elements in $\mathcal{T}_{l,t}$, represented by $z_{l,t}$ . The grouping process starts with the minimum delay in $\mathcal{T}_l$ to form the set of the disjoint sets $\boldsymbol{\mathcal{T}}_l = \{\mathcal{T}_{l,t}\}$, $t \in \{1, \dots, T\}$ where $\mathcal{T}_{l,t} = \{\tau_{l,1}, \tau_{l,2}, \dots, \tau_{l,z_t} : \tau_{l,i} \le \tau_{l,i+1} \text{ and } \tau_{l,z_t} - \tau_{l,1} \le \gamma\}$. Once $\boldsymbol{\mathcal{T}}_l$ is assembled, we create the average delay set as $\bar{\mathcal{T}}_l = \{\bar{\tau}_{l,t} : \bar{\tau}_{l,t} = \text{mean}(\mathcal{T}_{l,t})\}$.

Similar to (3-3), the new basis- matrix $\bar{\boldsymbol{\Psi}}_l$ is then built based on elements in the average delay set $\bar{\mathcal{T}}_l$ as

$$(\bar{\boldsymbol{\Psi}}_l)_{q,t} = \exp(-j2\pi f_q \bar{\tau}_{l,t}). \tag{3-5}$$

The size of $\bar{\boldsymbol{\Psi}}_l$ is $Q \times T$, each column of $\bar{\boldsymbol{\Psi}}_l$ represents a group of pixels corresponding to $(\bar{\tau}_{l,t} \pm \gamma)$ round-trip travel time.

Consequently, the size and the MC of new basis-matrix $\bar{\boldsymbol{\Psi}}_l$ is a function of $\gamma$. For the same example shown in Figure 3-2, Figure 3-3 , shows the normalized *Gramian matrix* $\bar{\boldsymbol{\Psi}}_l^{\mathrm{H}} \bar{\boldsymbol{\Psi}}_l$ for the new basis-matrix with $\gamma = \frac{2\Delta D}{c}$, where $\Delta D$ is the downrange resolution, and $c$ is the speed of light. The MC of this example is $\mu(\bar{\boldsymbol{\Psi}}_l) = 0.21$, and the total number of pixel-groups is $T$= 64 groups. To illustrate the physical meaning of the pixels in one group and their locations in the actual radar-image, Figure 3-4, shows one group of pixels for the aforementioned value of $\gamma$ at a given antenna location. Lastly, Figure 3-5, plots the MC values, $\mu(\bar{\boldsymbol{\Psi}}_l)$, versus delay-difference threshold $\gamma$. As a rule-of-thumb, and for pixel-sized targets, the value of $\gamma$ should not exceed $\frac{2\Delta D}{c}$.

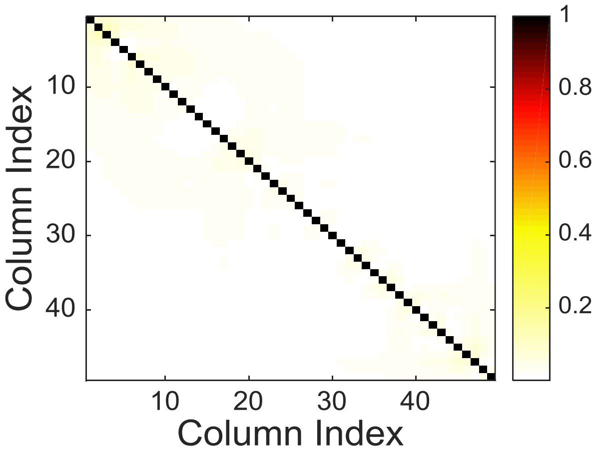

*Figure 3-3 Normalized Gramian matrix* $\bar{\boldsymbol{\Psi}}_l^H\bar{\boldsymbol{\Psi}}_l$ *of the new baissi-matrix* $\bar{\boldsymbol{\Psi}}_l$.

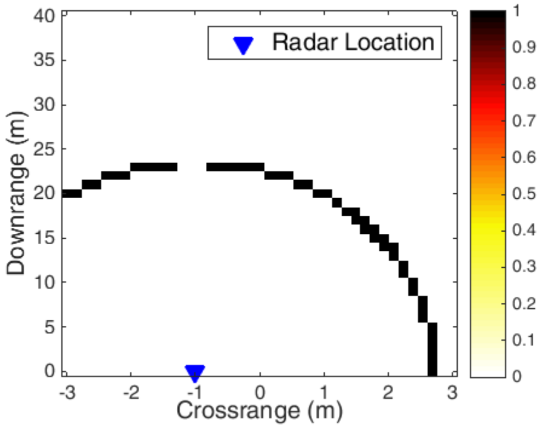

*Figure 3-4 Example of one pixel-group for* $\gamma = \frac{2\Delta D}{c}$ .

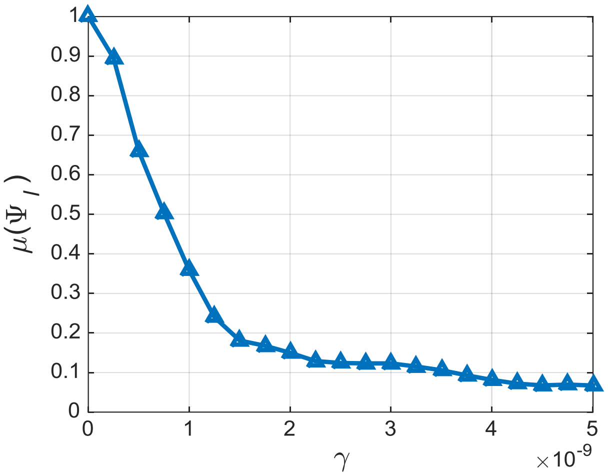

*Figure 3-5 Mutual-coherence of the proposed basis-matrix* $\bar{\boldsymbol{\Psi}}_l$ *versus* $\gamma$.

## 3.3 Using the New Basis-Matrix in CS-Algorithms

Using $\bar{\boldsymbol{\Psi}}_l$ instead of $\boldsymbol{\Psi}_l$ as a basis-matrix for radar-image recovery, will recover a vector, $\hat{\hat{\boldsymbol{\alpha}}}_l$, of length $T$. However, the desirable one-dimensional-image-vector $\hat{\boldsymbol{\alpha}}_l$ has a length of $N > T$, hence a mapping process from $\hat{\hat{\boldsymbol{\alpha}}}_l$ to $\hat{\boldsymbol{\alpha}}_l$ is required. Each nonzero element in the estimated $\hat{\hat{\boldsymbol{\alpha}}}_l$ should be mapped to its corresponding grouped pixels in $\hat{\boldsymbol{\alpha}}_l$. All pixels in that group will be given the same estimated value of their associated element in $\hat{\hat{\boldsymbol{\alpha}}}_l$. Let $\boldsymbol{\mathcal{Z}}_l = \{\mathcal{Z}_{l,1}, \mathcal{Z}_{l,2}, \dots, \mathcal{Z}_{l,t}, \dots, \mathcal{Z}_{l,T}\}$ be the grouped-supports set which contains sets of the pixel-supports corresponding to the set $\boldsymbol{\mathcal{T}}_l$, such that $\mathcal{Z}_{l,t}$ represents the set of the supports of the pixels with their delays in $\mathcal{T}_{l,t}$. Additionally, let $\bar{\mathcal{Z}}_l = \{\bar{z}_{l,1}, \bar{z}_{l,2}, \dots, \bar{z}_{l,t}, \dots, \bar{z}_{l,T}\}$ be the support set of the estimated vector $\hat{\hat{\boldsymbol{\alpha}}}_l$. After the estimation, we map $\bar{\mathcal{Z}}_l \mapsto \boldsymbol{\mathcal{Z}}_l$ such that $\hat{\boldsymbol{\alpha}}_l(\mathcal{Z}_{l,t}) =$

$\hat{\bar{\boldsymbol{\alpha}}}_l(\bar{z}_{l,t})$. This process is repeated for at all radar locations $L$. Table 3-1 shows the overall procedural flow for the imaging process.

*Table 3-1Procedural flow for the proposed radar-imaging processes with the grouping technique*

```
Start at the first radar location $l = 1$
for $l = 1: L$
    • Move the radar to location $l$, and illuminate the scene with SFCW signals and $Q$ freq bins.
    • Measure all $Q$ returns and stack them in the measurements vector $\mathbf{r}_l$.
    • Assemble the average delay set $\bar{\boldsymbol{\mathcal{T}}}_l$ and the mapping set $\bar{\boldsymbol{\mathcal{Z}}}_l$
    • Build the grouped basis matrix $\bar{\boldsymbol{\Psi}}_l$
    • Pass $\bar{\boldsymbol{\Psi}}_l$ and $\mathbf{r}_l$ to the SR-based algorithm
    • Estimate $\hat{\bar{\boldsymbol{\alpha}}}_l$.
    • Map $\hat{\bar{\boldsymbol{\alpha}}}_l$ to $\hat{\boldsymbol{\alpha}}_l$ as $\bar{\mathcal{Z}}_l \mapsto \boldsymbol{\mathcal{Z}}_l$   s.t.   $\hat{\boldsymbol{\alpha}}_l(\mathcal{Z}_{l,t}) = \hat{\bar{\boldsymbol{\alpha}}}_l(\bar{z}_{l,t})$.
end for
Compute:   $\hat{\boldsymbol{\alpha}} = \frac{1}{L}\sum_{l=1}^{L} \hat{\bar{\boldsymbol{\alpha}}}_l$
Reshape $\hat{\boldsymbol{\alpha}}$ to 2D for radar image representation as an output.
```

## 3.4 Results and Discussion

The proposed technique is applied on a simulated and a realistic RI data. Basis pursuit algorithm was used to reconstruct the radar-image at each location. A radar image system was simulated using MATLAB®. The desirable scene has a crossrange of $-3.00m$ and $3.00m$, and downrange of $6.20m$. A uniform linear monostatic array composed of 20-antenna elements spaced out by $10\text{cm}$ is used to capture the image. The center of the array is taken to be the origin of the scene.

A series of $801$ monochromatic waves to realize a UWB signal occupying a spectrum between $1$ and $3GHz$ is employed for the scene interrogation. We start by proving the concept of grouping at each radar location.

For comparison reason, we also applied the conventional CS-based as in [10]. Figure 3-6 shows a recovered image by the conventional CS-bases approach from a simulated RI data. The original scene contains three perfect-reflector targets as indicated by the red circles. The signal to noise ratio (SNR) is $SNR = 5dB$, and the relative error is $1.2$, where the relative error is defined as $\|\boldsymbol{\alpha} - \hat{\boldsymbol{\alpha}}\|/\|\boldsymbol{\alpha}\|$. For the same SNR, Figure 3-7 shows the recovered image with the proposed grouping technique, the relative error is $0.32$. All parameters were the same for both experiments. Although, thresholding the pixels of the final image would reduce the error, especiall for the case of grouping technique, but it was not used for fare comparison.

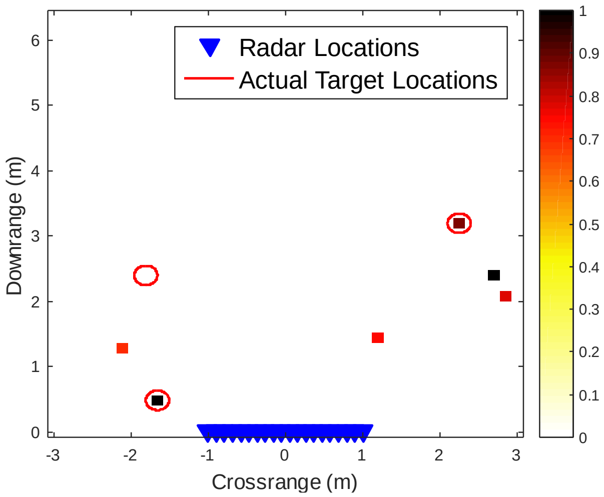

*Figure 3-6 Radar-image recovered from a simulated data using conventional CS-Based at SNR=5 dB, relative error=1.2.*

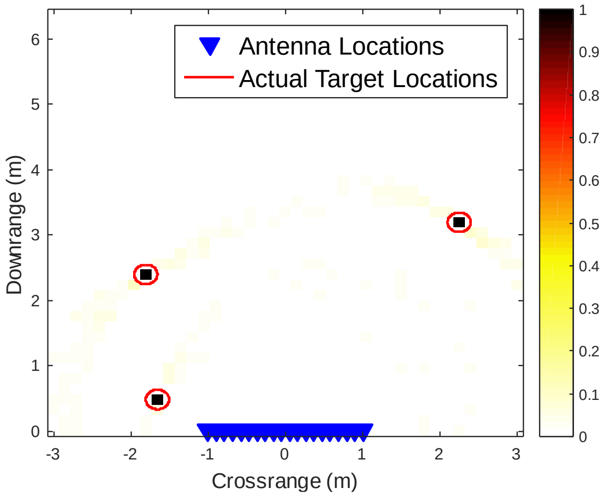

*Figure 3-7 Radar-image recovered from a simulated data the proposed grouping technique at SNR=5 dB, relative error=0.32.*

The proposes technique was also validated over a realistic RI data as shown in Figure 3-8. To generate the radar-realistic data, a SAR system was built to synthesis an antenna aperture of 2m. UWB antenna of 18GHz bandwidth was used to illuminate the scene with SFCW signal of 3GHz bandwidth and 801 frequency bins. The start frequency was 1GHz. The scene compromises of only two squareshaped metal targets of dimension 0.45m × 0.30m. The resultant image showed the true locations of the actual two targets.

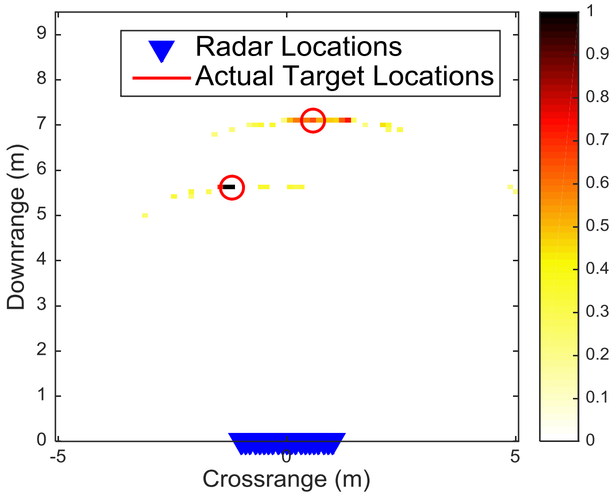

*Figure 3-8 Radar-image recovered from a realistic data using the proposed grouping technique.*

Lastly, we compare the performance of the grouping technique with the conventional CS-based approach, by evaluating their relative error for different SNR levels. The results are shown in Figure 3-9 , where the grouping technique outperforms the conventional CS-based approach, particularly at low SNR. The results were averaged over 500 trials.

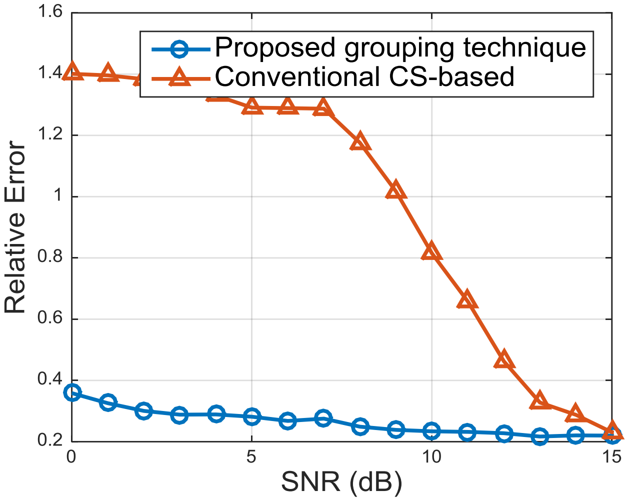

*Figure 3-9 Relative error versus SNR of the grouping technique and conventional CS-based radar imaging.*

## 3.5 Conclusion

The basis-matrix in the inverse problem of radar imaging systems demonstrates high mutual coherence, thereby hindering the sparse reconstruction of the radar image. Columns associated with similar time delays up to a given threshold are grouped together. A remapping process is required to generate the final image. The value of the threshold is set according to the size of the smallest target in the scene. The proposed technique enhances the noise immunity of the system and reduces the required computations in the sparse reconstruction algorithm.

> "*Probability theory is nothing but common sense reduced to calculation.*" [122]
>
> Pierre-Simon Laplace

# Chapter 4

# Low Complexity Sparse Bayesian Estimation for UWB Indoor Radar Imaging

In the previous chapter, we've proposed a solution of the problem of low-mutual-coherence basis-matrix in the radar image context. This chapter builds its derivations on the proposed technique in Chapter 3. Here, we design a low complexity Bayesian-base algorithm that is tailored for ultra-wideband (UWB) radar-imaging.

The advances of CS-based UWB-radar imaging is bombarded by the complexity of the reconstruction algorithms and their weak noise immunity. Exploiting the structure of the basis-matrix, a low complexity Bayesian-based estimation algorithm is proposed. The algorithm takes advantage of the radar-return statistic to find an approximate minimum mean-square error estimate (AMMSE) of the radar-image. The low complexity is achieved by utilizing the block-matrix-inversion formula to execute the algorithm in an order-recursive manner. Further simplification is achieved by using exponential-sum formula to find the correlation between the columns of the basis-matrix. The proposed algorithm is evaluated over experimental and simulated data. The results show faster processing time compared to other known algorithms, with comparable reconstruction quality.

The remaining sections of this chapter are arranged as follows. Section 4.2 presents the signal and the scene models. The development of the main Bayesian algorithm is conferred in Section 4.3. Section 4.4 addresses the execution process and the complexity reduction. Lastly, the results and the conclusions are presented in Sections 4.6 and 4.7 respectively.

## 4.1 Signal Model and Problem Formation

Consider a SAR system with monostatic configuration as illustrated in Figure 4-1. The antenna sweeps $L$ locations uniformly across the aperture length along the $x$-axis, with the mid-point at the origin of the scene. At each location, the antenna illuminates the scene with $Q$ SFCW signals of frequency bins $f_q$ for $q = 1,2,\ldots,Q$. The desire scene spans the positive $y$-axis.

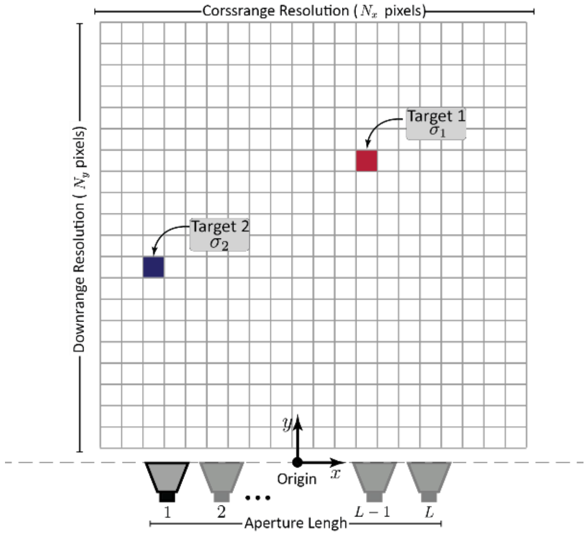

*Figure 4-1 Illustration on the scene-setup and the radar system model*

### 4.1.1 Received Signal Model

Let the scene of interest consists of $G$ targets, then the frequency representation of the received signal at the $l^{\text{th}}$ antenna location and the $q$-th frequency bin can be expressed as [14, 10]

$$r_{l,q} = \sum_{g=1}^{G} \sigma_g \exp\left(-j2\pi f_q \tau_{l,g}\right) + w_{l,q} \tag{4-1}$$

where $\sigma_g$ is the reflection coefficient of the $g$-th target which is assumed to be independent of the frequency. $f_q$ is the frequency of the transmitted signal, $\tau_{l,g}$ is the round trip delay for the signal to travel from the $l$-th antenna location to the

$g$-th target. At the $l$-th location and the $q$-th frequency, $w_{l,q}$ is complex additive white Gaussian noise with zero mean and variance $\sigma_{w_l}^2$

### 4.1.2 Received Signal in a Matrix Form

To generate the radar-image, we divide the scene in a total of $N$ pixels with $N_x$ pixels in the crossrange, and $N_y$ pixels in the downrange as shown in Figure 4-1. A pixel occupied by a target would have a value of $\sigma_g$ or zero otherwise. The frequency representation of the received signal in (4-1) for $q = 1,2,\dots,Q$ can be written in a matrix form as

$$\mathbf{r}_l = \mathbf{\Psi}_l \boldsymbol{\alpha}_l + \mathbf{w}_l \tag{4-2}$$

where the vector $\mathbf{r}_l$ represents returns for all frequencies at the $l^{\text{th}}$ location. $\boldsymbol{\alpha}_l$ is the one-dimensional representation of the radar-image at the $l^{\text{th}}$ location with length of $N$ elements. The vector $\mathbf{w}_l$ represents the additive white Gaussian noise, $\mathbf{w}_l \sim \mathcal{N}\left(0, \sigma_{w_l}^2 \mathbf{I}_Q\right)$.

The matrix $\mathbf{\Psi}_l$ represents the basis for the received vector $\mathbf{r}_l$ with dimension of $Q \times N$, i.e., the number of columns equal to the total number of pixels $N$, and the number of rows equal to the number of transmitted frequencies $Q$. Each column in the matrix represents the contribution of its corresponding pixel to the received vector $\mathbf{r}_l$. The elements of the $q$-th row and $n$-th column of $\mathbf{\Psi}_l$ is given by

$$(\mathbf{\Psi}_l)_{q,n} = \exp\left(-j2\pi f_q \tau_{l,n}\right) \tag{4-3}$$

where $\tau_{l,n}$ is the round trip time delay between the $l$-th location and the $n$-th pixel.

In this work, we estimate the vector $\boldsymbol{\alpha}_l$ by passing the received vector "the measurement vector" $\mathbf{r}_l$ to the proposed Bayesian estimation algorithm expounded in Section 4.2. The estimated one-dimensional vector $\hat{\boldsymbol{\alpha}}_l$, is then averaged over all locations to produce the final radar-image.

## 4.2 Bayesian Estimation

Let the number of targets in the scene be much less than the number of pixels in the image, i.e., $G \ll N$. In addition, let $\mathcal{S}_l$ be the set of supports of the nonzero elements of $\boldsymbol{\alpha}_l$, i.e., the locations of target-pixels in one-dimension. We can express $\mathbf{r}_l$ in terms of these nonzero elements, and their corresponding columns in $\mathbf{\Psi}_l$ as follows

$$\mathbf{r}_l = \mathbf{\Psi}_{l,\mathcal{S}_l} \boldsymbol{\alpha}_{l,\mathcal{S}_l} + \mathbf{w}_l. \tag{4-4}$$

Given the observation $\mathbf{r}_l$, the approximate minimum mean-square error (AMMSE) estimate, $\hat{\boldsymbol{\alpha}}_l$, is defined as [117]

$$\widehat{\boldsymbol{\alpha}}_l \triangleq \mathbb{E}[\boldsymbol{\alpha}_l|\mathbf{r}_l] = \sum_{i=1}^{|\boldsymbol{\mathcal{S}}_l|} \mathrm{p}\left(\mathcal{S}_l^i|\mathbf{r}_l\right)\mathbb{E}\left[\boldsymbol{\alpha}_l|\mathbf{r}_l,\mathcal{S}_l^i\right] \tag{4-5}$$

where, $\boldsymbol{\mathcal{S}}_l$ is a set of all sets for which the posteriors are significant [117], i.e., $\boldsymbol{\mathcal{S}}_l = \{\mathcal{S}_l^1, \mathcal{S}_l^2, \dots, \mathcal{S}_l^I\}$, where $I$ is the number of elements in $\boldsymbol{\mathcal{S}}_l$. The cardinality of $\boldsymbol{\mathcal{S}}_l$ is denoted by $|\boldsymbol{\mathcal{S}}_l|$.

Three essential elements are needed to compute the AMMSE of $\boldsymbol{\alpha}_l$ in (4-5). The first element is the set $\boldsymbol{\mathcal{S}}_l$; which is found using a greedy approach as detailed in Section 4.2.24.2.2. The second element is $\mathbb{E}\left[\boldsymbol{\alpha}_l|\mathbf{r}_l,\mathcal{S}_l^i\right]$ which reflects the expectation of the 1D-scene, $\boldsymbol{\alpha}_l$, given the received vector, $\mathbf{r}_l$, and the sets of nonzero supports,$\mathcal{S}_l^i$ $\forall i$. Last element, is the posteriors $\mathrm{p}\left(\mathcal{S}_l^i|\mathbf{r}_l\right)$ $\forall i$. These posteriors return the probability of the elements in the set $\mathcal{S}_l^i$ given the received vector $\mathbf{r}_l$. The latter two elements are explicated below.

### 4.2.1 Finding the Expectations and the Posteriors

Finding $\mathbb{E}\left[\boldsymbol{\alpha}_l|\mathbf{r}_l,\boldsymbol{\mathcal{S}}_l^i\right]$ and $\mathrm{p}\left(\mathcal{S}_l^i|\mathbf{r}_l\right)$ requires a complete statistical information for both $\boldsymbol{\alpha}_l$ and $\mathbf{r}_l$. In radar imaging, it is difficult to assume the distribution of the values in $\boldsymbol{\alpha}_l$; due to the wide variety of the targets [74], hence it is not feasible to find a closed form for the expectation $\mathbb{E}\left[\boldsymbol{\alpha}_l|\mathbf{r}_l,\mathcal{S}_l^i\right]$. Instead, we replace it with the best linear unbiased estimator [47] as

$$\mathbb{E}\left[\boldsymbol{\alpha}_l|\mathbf{r}_l,\mathcal{S}_l^i\right] \leftarrow \left(\boldsymbol{\Psi}_{l,\mathcal{S}_l^i}^{\mathrm{H}}\boldsymbol{\Psi}_{l,\mathcal{S}_l^i}\right)^{-1}\boldsymbol{\Psi}_{l,\mathcal{S}_l^i}\mathbf{r}_l. \tag{4-6}$$

For finding the posterior $\mathrm{p}(\mathcal{S}_l^i|\mathrm{r}_l)$, Bayes rule is used as

$$\mathrm{p}(\mathcal{S}_l^i|\mathbf{r}_l) = \frac{\mathrm{p}(\mathbf{r}_l|\mathcal{S}_l^i)\mathrm{p}(\mathcal{S}_l^i)}{p(\mathbf{r}_l)}. \tag{4-7}$$

The probability $\mathrm{p}(\mathbf{r}_l)$ in the denominator is a common scaling factor for all terms in the summation, in (4-5), and can be eliminated; because, the final answer will be normalized.

We use Bernoulli distribution to compute the prior $\mathrm{p}(\mathcal{S}_l^i)$, where each pixel in $\boldsymbol{\alpha}_l$ is assumed to have $\wp$ probability of being nonzero pixel, and $(1-\wp)$ of being zero. Accordingly, the prior $\mathrm{p}(\mathcal{S}_l^i)$ can be computed as

$$\mathrm{p}(\mathcal{S}_l^i) = \wp^{|\mathcal{S}_l^i|}(1-\wp)^{N-|\mathcal{S}_l^i|}. \tag{4-8}$$

Lastly, it remains to evaluate the likelihood $\mathrm{p}(\mathbf{r}_l|\mathcal{S}_l^i)$. We note that $\mathbf{r}_l$ is composed of two vectors, the first vector is the vector $\boldsymbol{\alpha}_{l,\mathcal{S}_l}$ in the subspace spanned by the columns of $\boldsymbol{\Psi}_{l,\mathcal{S}_l^i}$ with unknown distribution. The second vector is a white Gaussian noise vector of $\mathbf{w}_l \sim \mathcal{N}(0,\sigma_{w_l}^2\mathbf{I}_Q)$. In this step, we eliminate the non-Gaussian components of $\mathbf{r}_l$, to take advantage the Gaussian one. We project $\mathbf{r}_l$ on the orthogonal complement matrix of $\boldsymbol{\Psi}_{l,\mathcal{S}_l^i}$ [47]. The orthogonal complement matrix $\boldsymbol{\Psi}_{l,\mathcal{S}_l^i}^{\perp}$ is defined by

$$\mathbf{\Psi}^{\perp}_{l,\mathcal{S}_l^i} = \mathbf{I} - \mathbf{\Psi}_{l,\mathcal{S}_l^i}\left(\mathbf{\Psi}^{H}_{l,\mathcal{S}_l^i}\mathbf{\Psi}_{l,\mathcal{S}_l^i}\right)^{-1}\mathbf{\Psi}^{H}_{l,\mathcal{S}_l^i}. \tag{4-9}$$

This projection, leads to

$$\begin{aligned} \mathbf{\Psi}^{\perp}_{l,\mathcal{S}_l^i}\mathbf{r}_l &= \cancelto{\mathbf{0}}{\mathbf{\Psi}^{\perp}_{l,\mathcal{S}_l^i}\mathbf{\Psi}_{l,\mathcal{S}_l^i}}\boldsymbol{\alpha}_l + \mathbf{\Psi}^{\perp}_{l,\mathcal{S}_l^i}\mathbf{w}_l \\ &= \mathbf{\Psi}^{\perp}_{l,\mathcal{S}_l^i}\mathbf{w}_l \end{aligned} \tag{4-10}$$

which is a vector of Gaussian distribution with zero mean and covariance matrix given by

$$\begin{aligned} \mathbf{\Sigma} &= \mathbb{E}\left[\left(\mathbf{\Psi}^{\perp}_{l,\mathcal{S}_l^i}\mathbf{w}_l\right)\left(\mathbf{\Psi}^{\perp}_{l,\mathcal{S}_l^i}\mathbf{w}_l\right)^{\mathrm{H}}\right] \\ &= \mathbf{\Psi}^{\perp}_{l,\mathcal{S}_l^i}\mathbb{E}\left[\mathbf{w}_l\mathbf{w}_l^{\mathrm{H}}\right]{\mathbf{\Psi}^{\perp}_{l,\mathcal{S}_l^i}}^{\mathrm{H}} \\ &= \sigma^2_{\mathbf{w}_l}\,\mathbf{\Psi}^{\perp}_{l,\mathcal{S}_l^i}. \end{aligned} \tag{4-11}$$

Therefore, the likelihood $\mathrm{p}\left(\mathbf{r}_l|\mathcal{S}_l^i\right)$ can be written as

$$\mathrm{p}\left(\mathbf{r}_l|\mathcal{S}_l^i\right) \cong \frac{1}{\sqrt{\left(2\pi\sigma^2_{\mathbf{w}_l}\right)^M}}\exp\left(-\frac{1}{2}\left(\mathbf{\Psi}^{\perp}_{l,\mathcal{S}_l^i}\mathbf{r}_l\right)^{\mathrm{H}}\mathbf{\Sigma}^{-1}\left(\mathbf{\Psi}^{\perp}_{l,\mathcal{S}_l^i}\mathbf{r}_l\right)\right). \tag{4-12}$$

The above approximation is justified in [47].

Now we can find the posterior $\mathrm{p}\left(\mathcal{S}_l^i|\mathbf{r}_l\right)$ by substituting (4-8) and (4-12) in (4-7).

Now, we have the essential terms for finding $\hat{\boldsymbol{\alpha}}_l$ as in (4-5).

Next, we show how we find the elements "the sets $\mathcal{S}_l^i$" of the set $\boldsymbol{\mathcal{S}}_l$, for which the posteriors, $\mathrm{p}\left(\mathcal{S}_l^i|\mathbf{r}_l\right)$ $\forall i$, are significant.

### 4.2.2 Finding the Support Sets of Significant Posteriors

Ideally, the summation in (4-5) should be evaluated over all possible sets of the support-combinations of $\boldsymbol{\alpha}_l$, which is $2^N$possible sets. This gives the exact minimum mean square error estimate; however, it is computationally expensive and might be impractical. Alternatively, we evaluate this estimate over the sets for which the posteriors are significant, i.e. $\hat{\mathcal{S}}_l^i \triangleq \arg\max_{\mathcal{S}_l^i} \mathrm{p}\left(\mathcal{S}_l^i \middle| \mathbf{r}_l\right)$, where $\mathcal{S}_l^i$ is a set of $i$ elements "$i$ supports". In this section, we aim to find these sets and hence compose $\boldsymbol{\mathcal{S}}_l = \left\{\hat{\mathcal{S}}_l^1, \hat{\mathcal{S}}_l^2, \dots, \hat{\mathcal{S}}_l^I\right\}$. Eventually the set $\boldsymbol{\mathcal{S}}_l$ is used to evaluate the summation in (4-5) over $\boldsymbol{\mathcal{S}}_l$. The selection of $\hat{\mathcal{S}}_l^i$ is accomplished by means of a selection metric, $\nu\left(\mathcal{S}_l^i\right)$, which is defined as the logarithmic posterior.

$$
\begin{aligned}
\nu\left(\mathcal{S}_l^i\right) &\triangleq \ln\left(p\left(\mathcal{S}_l^i \middle| \mathbf{r}_l\right)\right) \\
&= -\frac{1}{2\sigma_{\mathbf{w}_l}^2}\left\|\boldsymbol{\Psi}_{l,\mathcal{S}_l^i}^{\perp}\mathbf{r}_l\right\|^2 + \left|\mathcal{S}_l^i\right| \ln \wp + \left(N - \left|\mathcal{S}_l^i\right|\right)\ln(1-\wp) \\
&= -\frac{1}{2\sigma_{\mathbf{w}_l}^2}\left\|\boldsymbol{\Psi}_{l,\mathcal{S}_l^i}\left(\boldsymbol{\Psi}_{l,\mathcal{S}_l^i}^{H}\boldsymbol{\Psi}_{l,\mathcal{S}_{l_i}}\right)^{-1}\boldsymbol{\Psi}_{l,\mathcal{S}_l^i}^{H}\mathbf{r}_l\right\|^2 \\
&\quad + \left|\mathcal{S}_l^i\right| \ln \wp + \left(N - \left|\mathcal{S}_l^i\right|\right)\ln(1-\wp) \\
&= -\frac{1}{2\sigma_{\mathbf{w}_l}^2}\left\|\boldsymbol{\Psi}_{l,\mathcal{S}_l^i}\mathbb{E}\left[\boldsymbol{\alpha}_{l_i}\middle|\mathbf{r}_l, \mathcal{S}_l^i\right]\right\|^2 \\
&\quad + \left|\mathcal{S}_l^i\right| \ln \wp + \left(N - \left|\mathcal{S}_l^i\right|\right)\ln(1-\wp).
\end{aligned}
\tag{4-13}
$$

The above metric is evaluated sequentially in a greedy manner. At the outset, $\nu\left(\mathcal{S}_l^i\right)$, is computed for a single element, i.e., $\mathcal{S}_l^1 = \{1\},\{2\},\dots,\{N\}$. Then we select the element of the largest value of $\nu(\mathcal{S}_l^1)$ as shown in "step 1" of Figure 4-2. Afterward, we evaluate $\nu(\mathcal{S}_l^i)$ for $\mathcal{S}_l^2$, given that the first element of $\mathcal{S}_l^2$ is the one that was selected in the previous step. Then $\nu(\mathcal{S}_l^i)$ is evaluated for $\mathcal{S}_l^3$ and so on. This procedure continues in the same manner until $|\boldsymbol{\mathcal{S}}_l| = G$, where $G$ is the number of targets. If the number of targets is unknown, the termination criteria is $\mathrm{p}(|\boldsymbol{\mathcal{S}}_l| > I) \leq \beta$, where $\beta$ is a small number. Figure 4-2 shows an example of finding $\boldsymbol{\mathcal{S}}_l$ for $N = 7$ and $I = 4$. Each row in the figure represents a step for evaluating $\nu(\mathcal{S}_l^i)$ where $i$ is the number of items in the set $\mathcal{S}_l^i$. The red-highlighted cells indicate the selected set which reflect the largest value of $\nu(\mathcal{S}_l^i)$ for the corresponding step. At the bottom of the Figure 4-2, the desirable set $\boldsymbol{\mathcal{S}}_l$ is shown. The algorithm steps are detailed in Table 4-1.

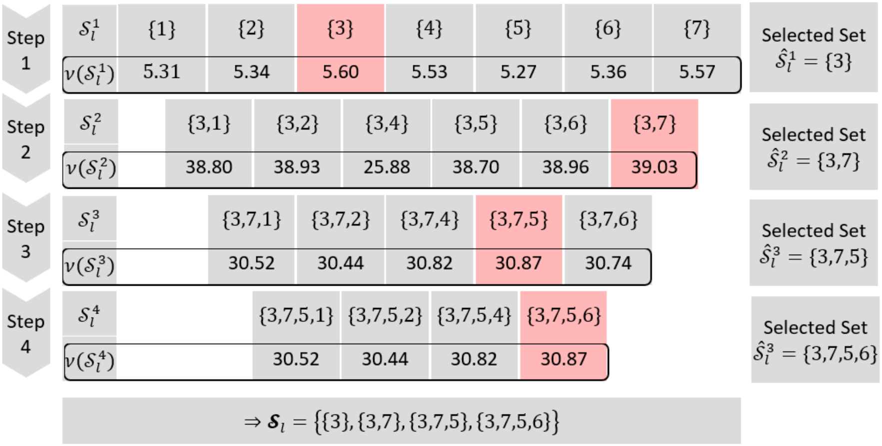

| | | | | | | | | | |
|---|---|---|---|---|---|---|---|---|---|
| Step 1 | $\mathcal{S}_l^1$ | {1} | {2} | {3} | {4} | {5} | {6} | {7} | Selected Set $\hat{\mathcal{S}}_l^1 = \{3\}$ |
| | $\nu(\mathcal{S}_l^1)$ | 5.31 | 5.34 | 5.60 | 5.53 | 5.27 | 5.36 | 5.57 | |
| Step 2 | $\mathcal{S}_l^2$ | {3,1} | {3,2} | {3,4} | {3,5} | {3,6} | {3,7} | | Selected Set $\hat{\mathcal{S}}_l^2 = \{3,7\}$ |
| | $\nu(\mathcal{S}_l^2)$ | 38.80 | 38.93 | 25.88 | 38.70 | 38.96 | 39.03 | | |
| Step 3 | $\mathcal{S}_l^3$ | {3,7,1} | {3,7,2} | {3,7,4} | {3,7,5} | {3,7,6} | | | Selected Set $\hat{\mathcal{S}}_l^3 = \{3,7,5\}$ |
| | $\nu(\mathcal{S}_l^3)$ | 30.52 | 30.44 | 30.82 | 30.87 | 30.74 | | | |
| Step 4 | $\mathcal{S}_l^4$ | {3,7,5,1} | {3,7,5,2} | {3,7,5,4} | {3,7,5,6} | | | | Selected Set $\hat{\mathcal{S}}_l^3 = \{3,7,5,6\}$ |
| | $\nu(\mathcal{S}_l^4)$ | 30.52 | 30.44 | 30.82 | 30.87 | | | | |

$\Rightarrow \boldsymbol{\mathcal{S}}_l = \{\{3\},\{3,7\},\{3,7,5\},\{3,7,5,6\}\}$

*Figure 4-2 Illustrative example on evaluating the selection metric* $\nu\left(\mathcal{S}_l^i\right)$ *for building the set* $\boldsymbol{\mathcal{S}}_l$

Once the set $\boldsymbol{\mathcal{S}}_l$ is built, we can find $\hat{\boldsymbol{\alpha}}_l$, by evaluating (4-5), for all locations $l$. The final radar-image is then averaged as

$$\hat{\boldsymbol{\alpha}} = \frac{1}{L}\sum \hat{\boldsymbol{\alpha}}_l. \tag{4-14}$$

*Table 4-1 Bayesian Estimation algorithm*

```
Inputs arguments: measurement vector $\mathbf{r}_l$, measurement Matrix $\boldsymbol{\Psi}_l$,
Initialization: $\mathcal{A} \leftarrow \{1,2,\dots,N\}$, $\mathcal{B} \leftarrow \mathcal{A}$, $i = 1, \boldsymbol{\mathcal{S}}_l = \phi$,
        $\hat{\mathcal{S}}_l^0 = \phi, Posteriors = \phi$, $Expectations = \phi$
while $i \le G$ do
    $\boldsymbol{\mathcal{C}} \leftarrow \{\hat{\mathcal{S}}_l^{i-1} \cup \{s_1\}, \hat{\mathcal{S}}_l^{i-1} \cup \{s_2\}, \dots, \hat{\mathcal{S}}_l^{i-1} \cup \{s_{|\mathcal{B}|}\} | s_j \in \mathcal{B}\}$
    compute $\{\nu(\mathcal{S}_l^i)\ \forall j, |\mathcal{S}_l^i \in \boldsymbol{\mathcal{C}}\}$                eq. (4-13)
    find $\hat{\mathcal{S}}_l^i \in \boldsymbol{\mathcal{C}}$ s.t. $\nu(\hat{\mathcal{S}}_l^i) \ge \max \nu(\mathcal{S}_j)\ \forall j$
    compute                    $\mathbb{E}[\boldsymbol{\alpha}|\mathbf{r}_l, \hat{\mathcal{S}}_l^i]$ eq. (4-6)
            $p(\hat{\mathcal{S}}_l^i|\mathbf{r}_l)$                eq.(4-7)
    $Posteriors \leftarrow \{Posteriors, p(\hat{\mathcal{S}}_l^i|\mathbf{r}_l)\}$
    $Expectations \leftarrow \{Expectations, \mathbb{E}[\boldsymbol{\alpha}_l|\mathbf{r}_l, \hat{\mathcal{S}}_l^i]\}$
    $\boldsymbol{\mathcal{S}}_l \leftarrow \{\boldsymbol{\mathcal{S}}_l, \hat{\mathcal{S}}_l^i\}$
    $\mathcal{B} \leftarrow \{\mathcal{A} \backslash \hat{\mathcal{S}}_l^i\}$
    $i = i + 1$
end while
compute and return $\hat{\boldsymbol{\alpha}}_l$ using $\boldsymbol{\mathcal{S}}_l$, $Posteriors$, and $Expectations$eq.
    (4-5)
```

## 4.3 Complexity Reduction

With a close look at the selection metric in (4-13), we notice that all three essential terms for finding $\hat{\boldsymbol{\alpha}}$ are embedded in evaluating $\nu(\mathcal{S}_l^i)$. In other words, by the time we evaluate $\nu(\mathcal{S}_l^i)$, for a given set $\mathcal{S}_l^i$, we would have already computed the posterior $p(\mathcal{S}_l^i|\mathbf{r}_l)$ and the expectation $\mathbb{E}[\boldsymbol{\alpha}_l|\mathbf{r}_l,\mathcal{S}_l^i]$. The computational complexity of evaluating $\nu(\mathcal{S}_l^i)$, in (4-13), lies in the matrix inversion of the expectation $\mathbb{E}[\boldsymbol{\alpha}_{l_i}|\mathbf{r}_l,\mathcal{S}_l^i]$. In this section, we make use of block-matrix-inversion formula to breakdown $\mathbb{E}[\boldsymbol{\alpha}_{l_i}|\mathbf{r}_l,\mathcal{S}_l^i]$ into vector-multiplication terms that can be executed in order-recursive manner. Then we use exponential-sum formula to apply further simplification on the vector multiplications.

### 4.3.1 **Computing the Expectation in Order-Recursive Fashion**

For compact notations, in the following derivations, we drop the subscript $l$ and the superscript $i$ from all symbols. For example, $\boldsymbol{\alpha}_l$, $\mathbf{r}_l$, and $\mathcal{S}_l^i$ become $\boldsymbol{\alpha}$, $\mathbf{r}$, and $\mathcal{S}$ respectively. Also, we will refer to $\mathbb{E}[\boldsymbol{\alpha}|\mathbf{r},\mathcal{S}_l^i]$ by $\boldsymbol{\varepsilon}_{\mathcal{S}}(\mathbf{r})$. However, it should be noted that all steps are executed for each $l$ radar observation and for all elements of $\boldsymbol{\mathcal{S}}_l$.

Consider a support set $\mathcal{S}$ for which $\nu(\mathcal{S})$ is to be evaluated. The elements of $\mathcal{S}$ are sorted as $\mathcal{S}=\{s_1,s_2,s_3,\dots,s_i\}$ where $s_1<s_2<\cdots<s_i$. Accordingly, we can rewrite $\boldsymbol{\varepsilon}_{\mathcal{S}}(\mathbf{r})$ in block matrix form as

$$\boldsymbol{\varepsilon}_{\mathcal{S}}(\mathbf{r})=\left(\begin{bmatrix}\boldsymbol{\Psi}_{\underline{\mathcal{S}}}^{\mathrm{H}}\\ \boldsymbol{\psi}_{s_i}^{\mathrm{H}}\end{bmatrix}\begin{bmatrix}\boldsymbol{\Psi}_{\underline{\mathcal{S}}} & \boldsymbol{\psi}_{s_i}\end{bmatrix}\right)^{-1}\begin{bmatrix}\boldsymbol{\Psi}_{\underline{\mathcal{S}}}^{\mathrm{H}}\mathbf{r}\\ \boldsymbol{\psi}_{s_i}^{\mathrm{H}}\mathbf{r}\end{bmatrix} \tag{4-15}$$

where $\underline{\mathcal{S}} = \mathcal{S}\backslash\mathscr{s}_i = \{\mathscr{s}_1, \mathscr{s}_2, \dots, \mathscr{s}_{i-1}\}$, and $\mathbf{\Psi}_{\underline{\mathcal{S}}}$ represents the selected columns of $\mathbf{\Psi}$ corresponding to the elements of $\underline{\mathcal{S}}$. $\boldsymbol{\psi}_{\mathscr{s}_i}$ is the $\mathscr{s}_i$-th column of $\mathbf{\Psi}$. It should be noticed that evaluating $\boldsymbol{\varepsilon}_{\mathcal{S}}(\mathbf{r})$ depends on all columns in the set $\underline{\mathcal{S}}$, in addtion to the last colum on the set $\mathcal{S}$. Hence it can be evaluated in order-recursive manner. Next we explain how to update $\boldsymbol{\varepsilon}_{\underline{\mathcal{S}}}(\mathbf{r})$ to compute $\boldsymbol{\varepsilon}_{\mathcal{S}}(\mathbf{r})$.

As derived in Appendix I, we use the block-matrix-inversion formula to breakdown the right-hand-side of (4-15) to another recursion form as

$$\boldsymbol{\varepsilon}_{\mathcal{S}}(\mathbf{r}) = \begin{bmatrix} \boldsymbol{\varepsilon}_{\underline{\mathcal{S}}}(\mathbf{r}) + \dfrac{1}{d_{\mathcal{S}}}\boldsymbol{\varepsilon}_{\underline{\mathcal{S}}}(\boldsymbol{\psi}_{\mathscr{s}_i})\left[\boldsymbol{\rho}_{\mathscr{s}_i}(\mathbf{\Psi}_{\underline{\mathcal{S}}})\boldsymbol{\varepsilon}_{\underline{\mathcal{S}}}(\mathbf{r}) - \rho_{\mathscr{s}_i}(\mathbf{r})\right] \\ -\dfrac{1}{d_{\mathcal{S}}}\left[\boldsymbol{\rho}_{\mathscr{s}_i}(\mathbf{\Psi}_{\underline{\mathcal{S}}})\boldsymbol{\varepsilon}_{\underline{\mathcal{S}}}(\mathbf{r}) - \rho_{\mathscr{s}_i}(\mathbf{r})\right] \end{bmatrix} \tag{4-16}$$

where

$$\boldsymbol{\varepsilon}_{\underline{\mathcal{S}}}(\boldsymbol{\psi}_{\mathscr{s}_i}) = \left(\mathbf{\Psi}_{\underline{\mathcal{S}}}^{\mathrm{H}}\mathbf{\Psi}_{\underline{\mathcal{S}}}\right)^{-1}\mathbf{\Psi}_{\underline{\mathcal{S}}}^{\mathrm{H}}\boldsymbol{\psi}_{\mathscr{s}_i} \tag{4-17}$$

$$\boldsymbol{\rho}_{\mathscr{s}_i}(\mathbf{\Psi}_{\underline{\mathcal{S}}}) = \boldsymbol{\psi}_{\mathscr{s}_i}^{\mathrm{H}}\mathbf{\Psi}_{\underline{\mathcal{S}}} \tag{4-18}$$

$$\rho_{\mathscr{s}_i}(\mathbf{r}) = \boldsymbol{\psi}_{\mathscr{s}_i}^{\mathrm{H}}\mathbf{r} \tag{4-19}$$

$$d_{\mathcal{S}} = 1 - \boldsymbol{\rho}_{\mathscr{s}_i}(\mathbf{\Psi}_{\underline{\mathcal{S}}})\boldsymbol{\varepsilon}_{\underline{\mathcal{S}}}\left(\boldsymbol{\psi}_{\mathscr{s}_i}\right) \tag{4-20}$$

The recursion in (4-16) is initiated with $\boldsymbol{\varepsilon}_{\mathscr{s}_1}(\mathbf{r}) = \left(\boldsymbol{\psi}_{\mathscr{s}_1}^{\mathrm{H}}\boldsymbol{\psi}_{\mathscr{s}_1}\right)^{-1}\boldsymbol{\psi}_{\mathscr{s}_1}^{\mathrm{H}}\mathbf{r}$ for $\mathscr{s}_1 \in \{1,2,\dots N\}$. Equation (4-17) is another recursion in the same form as (4-15), therefore we use the same approach to update $\boldsymbol{\varepsilon}_{\underline{\mathcal{S}}}(\boldsymbol{\psi}_{\mathscr{s}_i})$ to obtain $\boldsymbol{\varepsilon}_{\mathcal{S}}(\boldsymbol{\psi}_{\mathscr{s}_{i+1}})$ as

$$\boldsymbol{\varepsilon}_{\mathcal{S}}\left(\boldsymbol{\psi}_{s_{i+1}}\right) = \begin{bmatrix} \boldsymbol{\varepsilon}_{\underline{\mathcal{S}}}\left(\boldsymbol{\psi}_{s_{i+1}}\right) + \frac{1}{d_{\underline{\mathcal{S}}}}\boldsymbol{\varepsilon}_{\underline{\mathcal{S}}}\left(\boldsymbol{\psi}_{s_i}\right)\left[\boldsymbol{\rho}_{s_i}\left(\boldsymbol{\Psi}_{\underline{\mathcal{S}}}\right)\boldsymbol{\varepsilon}_{\underline{\mathcal{S}}}\left(\boldsymbol{\psi}_{s_{i+1}}\right) - \rho_{s_i}\left(\boldsymbol{\psi}_{s_{i+1}}\right)\right] \\ -\frac{1}{d_{\underline{\mathcal{S}}}}\left[\boldsymbol{\rho}_{s_i}\left(\boldsymbol{\Psi}_{\underline{\mathcal{S}}}\right)\boldsymbol{\varepsilon}_{\underline{\mathcal{S}}}\left(\boldsymbol{\psi}_{s_{i+1}}\right) - \rho_{s_i}\left(\boldsymbol{\psi}_{s_{i+1}}\right)\right] \end{bmatrix} \qquad (4\text{-}21)$$

The derivation of (4-21) is detailed in Appendix II. The index $i$ in $\boldsymbol{\varepsilon}_{\mathcal{S}}\left(\boldsymbol{\psi}_{s_{i+1}}\right)$ and $\boldsymbol{\rho}_{s_i}\left(\boldsymbol{\Psi}_{\underline{\mathcal{S}}}\right)$ starts with $i = 2$. Hence, they are initialized with $\boldsymbol{\varepsilon}_{\mathcal{S}}\left(\boldsymbol{\psi}_{s_3}\right)$, $\boldsymbol{\rho}_{s_2}^{\mathrm{H}}\left(\boldsymbol{\psi}_{s_1}\right)$. Table 4-2 shows the algorithm steps for evaluating $\boldsymbol{\varepsilon}_{\mathcal{S}}(\mathbf{r})$ in (4-15). It should be noted that the algorithm in Table 4-2 is executed implicitly in line 5 of the Bayesian algorithm in Table 4-1

### 4.3.2 **Simplifications of Column Crosscorrelations**

Up to this far, we evaluate $\mathbb{E}\left[\boldsymbol{\alpha}_l \middle| \mathbf{r}_l, \mathcal{S}_l^i\right]$ in order-recursive manner with complexity $\mathcal{O}(GMN)$. Additional simplification can be achievded by considering the stucture of the basis-matrix $\boldsymbol{\Psi}$. We notice that equations (4-17), (4-18), and (4-20) rely on the correlation between the columns of the basis-matrix $\boldsymbol{\Psi}$, i.e. $\boldsymbol{\psi}_j^{\mathrm{H}}\boldsymbol{\psi}_k$ where $j, k = 1, \ldots, N$. Based on the definition of the elements of the columns of $\boldsymbol{\Psi}$, see (4-3), we can simplify their mutual correlation as

$$\begin{aligned}\boldsymbol{\psi}_j^{\mathrm{H}}\boldsymbol{\psi}_k &= \sum_{q=1}^{Q} \exp\left(j2\pi f_q \tau_j\right)\exp\left(-j2\pi f_q \tau_k\right) \\ &= \sum_{m=\eta}^{\zeta} \exp\left(j2\pi m\Delta f\left(\tau_j-\tau_k\right)\right) \\ &= \frac{z^{\zeta-1}-z^{\eta}}{z-1} \quad \text{for } \tau_j \neq \tau_k\end{aligned} \tag{4-22}$$

where $\eta = f_1/\Delta f$, $\zeta = f_Q/\Delta f$, and $z = \exp\left(j2\pi\Delta f\left(\tau_j-\tau_k\right)\right)$. Therefore, the correlation between two columns of $\boldsymbol{\Psi}$ can be obtained in one operation using only their associated delays i.e., $\tau_j, \tau_k$. In his way, the complexity of finding $\boldsymbol{\psi}_j^{\mathrm{H}}\boldsymbol{\psi}_k$ drops from $Q$ sum operations to only one operation. Consequently, using (3-4) for evaluating (4-17)-(4-18) reduces the algorithm's complexity to $\mathcal{O}(GN)$.

*Table 4-2 Recursion algorithm for evaluating $\boldsymbol{\varepsilon}_{\mathcal{S}}(\boldsymbol{r})$ in (4-15)*

```
Input $\boldsymbol{\Psi}$, $\mathcal{C} = \{s_1, s_2, \dots, s_I\}$, $\mathbf{r}$
$\mathbf{a} \leftarrow \boldsymbol{\varepsilon}_{s_1}(\mathbf{r}) = \left(\boldsymbol{\psi}_{s_1}^{\mathbf{H}}\boldsymbol{\psi}_{s_1}\right)^{-1}\boldsymbol{\psi}_{s_1}^{\mathbf{H}}\mathbf{r}$          }
$\mathbf{b} \leftarrow \boldsymbol{\varepsilon}_{s_1}(\boldsymbol{\psi}_{s_2}) = \left(\boldsymbol{\psi}_{s_1}^{\mathbf{H}}\boldsymbol{\psi}_{s_1}\right)^{-1}\boldsymbol{\psi}_{s_1}^{\mathbf{H}}\boldsymbol{\psi}_{s_2}$   }
$\mathbf{c} \leftarrow \boldsymbol{\psi}_{s_1}^{\mathrm{H}}\boldsymbol{\psi}_{s_2}$                                        } initialization
$d \leftarrow d_{s_1} = 1 - \mathbf{c}^{\mathrm{H}}\mathbf{b}$                                  }
for $i = 2 : I - 1$
    $\mathcal{S} \leftarrow \{s_1, s_2, \dots, s_i\}$
    form $\boldsymbol{\Psi}_{\mathcal{S}}$
    $\mathbf{b} \leftarrow \boldsymbol{\varepsilon}_{\mathcal{S}}(\boldsymbol{\psi}_{s_{i+1}})$ using $\mathbf{b}, \mathbf{c}, d$   eq.(4-21)
    $\mathbf{c} \leftarrow \boldsymbol{\rho}_{s_i}(\boldsymbol{\Psi}_{\underline{\mathcal{S}}})$                 eq.(4-18)
    $e \leftarrow \rho_{s_i}(\mathbf{r})$                   eq.(4-19)
    $d \leftarrow d_{\mathcal{S}}$ using $\mathbf{b}, \mathbf{c}$              eq.(4-20)
    $\mathbf{a} \leftarrow \boldsymbol{\varepsilon}_{\mathcal{S}}(\mathbf{r})$ using $\mathbf{a}, \mathbf{b}, \mathbf{c}, d$      eq.(4-16)
end for
Return a
```

## 4.4 Results and Discussions

In this section, the performance of the proposed algorithm is evaluated for different SNR ratios against three well-known algorithms in the literature. The proposed algorithm is Bayesian and greedy based at the same time and it promotes sparsity, thus we choose algorithms who share some of those features for fair comparison. Namely: Orthogonal Matching Pursuit (OMP), which is a greed-based and known for its fast execution [27]; Fast Bayesian matching pursuit (FBMP) which is a greedy and Bayesian based algorithm, but unlike the proposed algorithm, it constrains Gaussian distribution on the pixel values [117]. Last algorithm we chose is basis pursuit (BS), which is $\ell_1$-minimization-based and it does not consider on any statistical information of the pixels [34].

The running time is evaluated as a measure of complexity. In addition to simulation, measured data was also used to validate the applicability of the proposed algorithm.

Using MATLAB, a simulated SAR imaging system was designed with 2m length. The scene contains three pixel-sized targets of uniformly-distributed reflectivity. The SAR illuminated the scene form 21 locations with SFCW signal of 3 GHz bandwidth and 801 frequency bins. The start frequency was 1GHz. Using the proposed low-complexity Bayesian estimation(4-3) Figure 4-3 shows an example of a reconstructed scene from noisy measurements of $\mathrm{SNR} = 10\mathrm{dB}$. The low-intensity pixels around the actual targets, are the pixels who share the same distance from the antenna with the actual targets. Their intensity can be reduced by increasing the number of antenna locations.

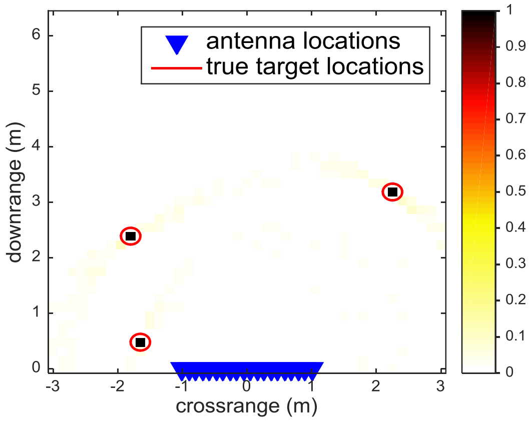

*Figure 4-3 Example of a reconstructed scene using the proposed low-complexity Bayesian algorithm*

The performance of the algorithm is measured by finding the relative error for the reconstructed image for different SNR. The relative error is defined as

$$\text{Relative Error} = \frac{\|\boldsymbol{\alpha} - \hat{\boldsymbol{\alpha}}\|^2}{\|\boldsymbol{\alpha}\|^2} \tag{4-23}$$

where $\boldsymbol{\alpha}$ is the original scene, and $\hat{\boldsymbol{\alpha}}$ is the reconstructed scene. Figure 4-4 compares the performance of the proposed algorithm with the orthogonal matching pursuit, fast Bayesian matching pursuit, and the basis pursuit. All measurements were taken into consideration without any compression. The results were averaged over

1000 trials. For each trial, different target locations, reflectivity and noise realizations were used. As shown in Figure 4-4, the proposed low complexity Bayesian estimator outperforms other algorithms especially at the high SNR values.

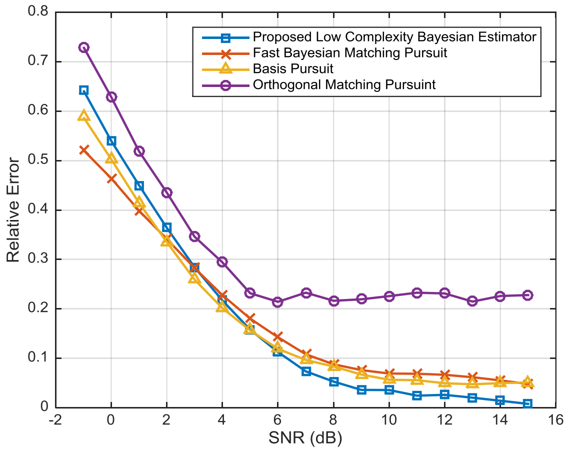

*Figure 4-4 Relative Error vs. SNR*

The run time was used with used to assess and compare the complexity. The scene and the system parameters were kept the same as in the previous setup. Figure 4-5 shows the runtime vs. the number of frequencies used, $Q$, to illuminate the scene. The runtime was averaged over 1000 trials with $\mathrm{SNR} = 10\ \mathrm{dB}$ for all trials, but with different noise realization. Since the complexity of the proposed algorithm does not vary with the number of frequencies, its runtime is a constant as shown in Figure 4-5.

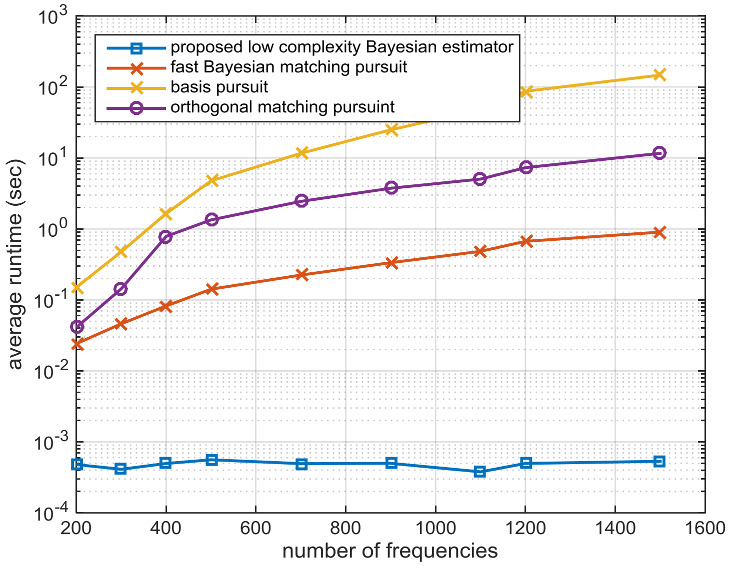

*Figure 4-5 Average runtime vs. number of used frequencies*

Lastly, the algorithm is validated on realistic measurements. To generate the radar-experimental data, a SAR system was built to synthesize an antenna aperture of 2m.UWB antenna was used to illuminate the scene with SFCW signal of 3 GHz bandwidth and 801 frequency bins. The start frequency was 1GHz, and the stop frequency was 4GHz. The scene compromises of only two cuboid metal object of dimension $0.18\text{m} \times 0.45\text{m} \times 0.45\text{m}$. For comparison, Figure 4-6 shows the radar-image that was generated by the conventional delay-and-sum algorithm while Figure 4-7 shows the radar-image generated by the proposed low-complexity Bayesian estimation algorithm. In both figures the scene was illuminated from 20 antenna locations starting from $-1\text{m}$ to $1\text{m}$ as depicted in the figure.

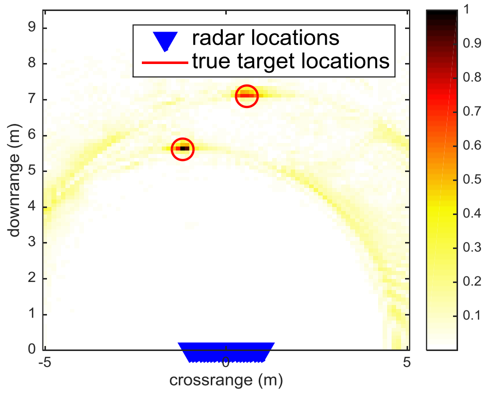

*Figure 4-6 Radar image of the delay-and-sum algorithm*

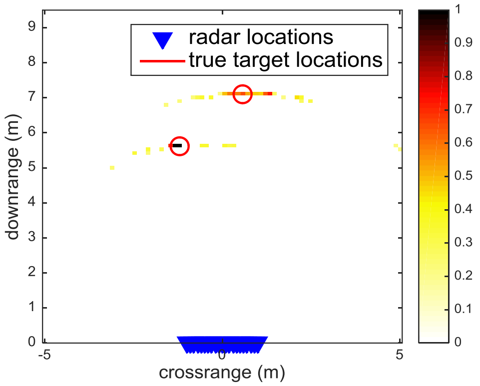

*Figure 4-7 Radar image of the proposed Bayesian algorithm*

## 4.5 Conclusion

In this chapter, we introduced a low-complexity Bayesian estimation for UWB radar imaging. Unlike other Bayesian-based algorithms, the proposed algorithm does not impose any statistical condition on the intensity of the pixels. It is implemented in fast order-recursive manner with linear complexity of order $O(GN)$, where $G$ is the number of targets in the scene, and $N$ is the total number of pixels. The execution time does not vary with number of used frequency to illuminate the scene. By grouping the pixels who share the same distance from the antenna, we were able to reduce the mutual coherence of the basis-matrix at each radar location, and hence enhance the accuracy of calculating the posteriors at each radar location. The algorithm is robust and outperforms other well-known algorithms for different SNR levels.

> “*…antenna correlation based channel estimators can bring about significant gains compared to scalar estimators, specially in the low to medium SNR range.*” [126]
>
> Jose Flordelis
> Lund University, Sweden

# Chapter 5

# Cooperative Bayesian Estimation for Compressed Indoor Radar Imaging

In the previous chapter, the proposed Bayesian-based algorithm was implemented independently at each antenna location, the resultant sub-images at all locations are then averaged together to generate the final image. In this chapter, we modify the algorithm and take it to a further step by capitalising on the correlation between the antenna elements. We propose a novel collaborative algorithm that allows antenna elements of the SAR array to share information about the scene. Each antenna calculates statistical information, such as the marginal probability of every pixel in the scene, and then share it with a selected antenna in the array. Sharing statistical information does not only enhance the recovery performance, but it helps in suppressing the multipath effects caused by the surrounding walls in indoor environment.

Results based on synthesized data and real experiments show that the proposed method can greatly enhance the performance in low NSR. It also aids in multipath suppression and hence increase signal-to-clutter ratio.

## 5.1 System and Scene Model

Consider a synthetic aperture radar emitting the desired scene with a stepped-frequency signal of $Q$ frequency bins from $L$ locations. As illustrated in Figure 5-1, the scene is comprised of $G$ targets and surrounded with three walls. When the signal travels form an antenna element, it gets reflected to back though direct path and multipath owing to the wall reflections and others. Assuming a monostatic configuration of the SAR system, and considering only multipath caused by the surrounding walls, the scene return at the $l$ location from the $q$th emitted frequency can be expressed as

$$r_{l,q} = \sum_{w=1}^{W} \sum_{g=0}^{G} \sigma_g^w \exp\left(-j2\pi f_q \tau_{g,l}^w\right) + v_{l,q} \tag{5-1}$$

where $G$ represents the number of targets in the scene, and $\sigma_g^w$ is the reflection coefficient of the $g$-th target corresponding the $w$-th path [3]. The time $\tau_{g,l}^w$ is the round-trip delay time between the $g$th targets and the $l$th location corresponding to the $w$th path. We consider the direct path, as depicted by soled lines in Figure 5-1, and the first order multipath, as depicted by the dashed lines in Figure 5-1. All reflection coefficients are assumed to be frequency-independent [68].

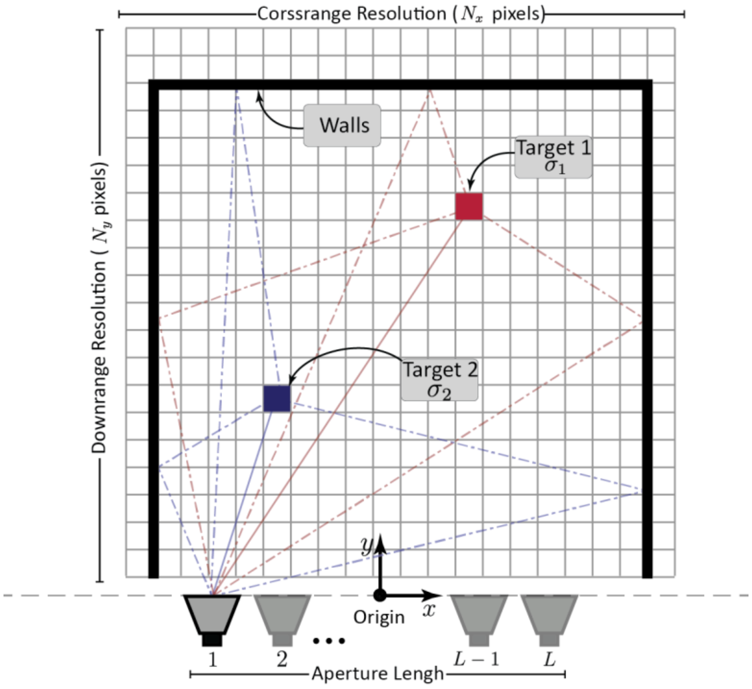

*Figure 5-1 Radar system and scene model*

Conventionally, after collecting $r_{l,q}$ for all $Q$ frequencies at all $L$ locations, delay-and-sum algorithm is applied to generate the radar image by DSB as follows. Let the radar image comprised of $N$ pixels distributed over the cross-rage and the downrange of the image, hence the value of the $n^{\text{th}}$ pixel is obtained by:

$$I(\mathbf{x}_n) = \frac{1}{LQ}\sum_{l=1}^{L}\sum_{q=1}^{Q} r_{l,q} \exp\left(j2\pi f_q \tau_{nl}\right) \tag{5-2}$$

where $\mathbf{x}_n$is the coordinate two-dimensional vector of the pixel $n$.

Given the above signal model, in the following section we express the radar return for the indoor environment in a matrix for convenience manipulation in algorithm development.

## 5.2 Radar Image as an Inverse Problem

Let the vector $\mathbf{r}_l$ represents all $r_{l,q}$returns at the $l^{\text{th}}$ location. It can be expressed as

$$\mathbf{r}_l = \sum_{w=1}^{W} \mathbf{\Psi}_l^{\text{w}} \boldsymbol{\alpha}_l + \mathbf{v}_l \tag{5-3}$$

$\boldsymbol{\alpha}_l$ is the one-dimensional representation of the radar-image at the $l^{\text{th}}$ location with length of $N$ elements. The nonzero element of $\boldsymbol{\alpha}_l$ represents a target's pixel. The vector $\mathbf{v}_l$ is the additive white Gaussian noise, $\mathbf{v}_l \sim \mathcal{N}\left(0, \sigma_{\mathbf{v}_l}^2 \mathbf{I}_Q\right)$.

The matrix $\mathbf{\Psi}_l^w$ represents the basis for the received vector $\mathbf{r}_l$ corresponding to the $w$-th path, with dimension of $Q \times N$, i.e., the number of columns equal to the total number of pixels $N$, and the number of rows equal to the number of transmitted frequencies $Q$. Each column in the matrix represents the contribution of its corresponding pixel to the received vector $\mathbf{r}_l$. The elements of the $q$-th row and the $n$-th column of $\boldsymbol{\Psi}_l^w$ is given by

$$(\boldsymbol{\Psi}_l^{\mathrm{w}})_{q,n} = \exp\left(-j2\pi f_q \tau_{l,n}^{w}\right) \tag{5-4}$$

where $\tau_{l,n}^{w}$ is the roundtrip time delay between the $l$-th location and the $n$-th pixel corresponding to the $w$th path. Assuming the full knowledge of the scene diminution, and according to the multipath model in [75], all delays $\tau_{l,n}^{w}$ can be calculated.

At the sensing stage, the received vector $\mathbf{r}_l$ is projected on a random selection matrix $\boldsymbol{\Phi}_l$, of dimension $M \times N$ where $M < N$, creating a compressed version of the received vector $\mathbf{r}_l$ at the location $l$ as following:

$$\begin{aligned} \mathbf{y}_l &= \boldsymbol{\Phi}_l \boldsymbol{\Psi}_l \boldsymbol{\alpha}_l + \mathbf{w}_l \\ &= \boldsymbol{V}_l \boldsymbol{\alpha}_l + \mathbf{w}_l \end{aligned} \tag{5-5}$$

$\boldsymbol{V}_l$ is $M \times N$ random matrix, $\boldsymbol{\Psi}_l = \sum_{w=1}^{W} \boldsymbol{\Psi}_l^{\mathrm{w}}$, and $\mathbf{w}_l$ is the additive white Gaussian noise vector that is $\mathbf{w}_l \sim \mathcal{N}\left(0, \sigma_{w_l}^2 \mathbf{I}_M\right)$. The aim of TWRI is to estimate $\boldsymbol{\alpha}_l \; \forall \; l$, and generate the final radar image $\boldsymbol{\alpha}$ as

$$\widehat{\boldsymbol{\alpha}} = \frac{1}{L}\sum_{l=1}^{L} \widehat{\widehat{\boldsymbol{\alpha}}}_l. \tag{5-6}$$

The system in (5-5) is underdetermined system with many solutions. By exploiting the sparsity nature of the image vector $\boldsymbol{\alpha}_l$, compressive sensing technique would be a good candidate for estimating $\boldsymbol{\alpha}_l$. For successful estimation of $\boldsymbol{\alpha}_l$, the theory of compressive sensing requires that the sensing matrix $\boldsymbol{V}_l$ should demonstrate low mutual coherence value, $\mu(\boldsymbol{V}_l)$. This requirement is not satisfied in this context of radar imaging. The reason for high mutual coherence value of $\boldsymbol{V}_l$ is owing to the fact that the bases matrix, $\boldsymbol{\Psi}_l$, is highly structured. To go around this issue, we use a grouping technique, proposed in Chapter 3 and in [86], for building a new basis matrix, $\overline{\boldsymbol{\Psi}}_l$, that results in a sensing matrix, $\overline{\mathbf{V}}_l$, of low mutual coherence value.

## 5.3 Bayesian Estimation at each Antenna Location

The image vector $\boldsymbol{\alpha}_l$ in (5-5) can be modelled as

$$\boldsymbol{\alpha}_l = \boldsymbol{\alpha}_l^{\mathrm{A}} \odot \boldsymbol{\alpha}_l^{\mathrm{B}} \tag{5-7}$$

where $\odot$ is an element by element multiplication or “Hadamard Multiplication”. The elements of the vector $\boldsymbol{\alpha}_l^{\mathrm{A}}$ are drown from unknown distribution, while the elements of $\boldsymbol{\alpha}_l^{\mathrm{B}}$ are independent non-identical Bernoulli random variables distributed as

$$\mathrm{p}\left(\boldsymbol{\alpha}_l^{\mathrm{B}}(n)=j\right)=\begin{cases}\mathcal{p}_{l,n} & j=1\\ 1-\mathcal{p}_{l,n} & j=0\end{cases}. \tag{5-8}$$

We call $\mathcal{p}_{l,n}\ \forall\ n$ the sparsity rates, since they control how sparse or dens the vector $\boldsymbol{\alpha}_l$ is.

In the available Bayesian estimation approaches, the distribution of the vector $\boldsymbol{\alpha}_l^{\mathrm{A}}$ is assumed to be Gaussian [21, 31, 33], which is not a realistic assumption for radar imaging, because the pixels' values vary with the material and shape of the occupied targets, i.e., with the reflectivity coefficient of the targets. It should be highlighted that the algorithm described in this section is agnostic to the distribution of the vector $\boldsymbol{\alpha}_l^{\mathrm{A}}$, i.e., it works with any types of targets, as we detail in the coming discussion.

Given the observation $\mathbf{y}_l$, the MMSE of $\boldsymbol{\alpha}_l$ at the $l^{\mathrm{th}}$location is defined as

$$\widehat{\boldsymbol{\alpha}}_l \triangleq \mathbb{E}[\boldsymbol{\alpha}_l|\mathbf{y}_l]=\sum_{\mathcal{S}_l\in\boldsymbol{\mathcal{S}}_l}\mathrm{p}(\mathcal{S}_l|\mathbf{y}_l)\mathbb{E}[\boldsymbol{\alpha}_{\mathrm{l}}|\mathbf{y}_l,\mathcal{S}_l] \tag{5-9}$$

where $\mathcal{S}_l$ is a set of supports "indices" of possible nonzero elements of $\boldsymbol{\alpha}_l$, i.e., $\mathcal{S}_l=\{\mathcal{s}_{l1},\mathcal{s}_{l2},\dots,\mathcal{s}_{la}\},\mathcal{s}_{li}\in\{1,\dots,N\}$. $\mathbb{E}[\boldsymbol{\alpha}_l|\mathbf{y}_l,\mathcal{S}_l]$ and $p(\mathcal{S}_l|\mathbf{y}_l)$ are respectively, the conditional expectation and the posterior of $\mathcal{S}_l$ given $\mathbf{y}_l$. The bold set notation $\boldsymbol{\mathcal{S}}_l$ is a set of all possible combination sets, of the supports in the vector $\boldsymbol{\alpha}_l$. Typically, the above summation, in

(5-9), should be evaluated over all element of $\boldsymbol{\mathcal{S}}_l$, which are $2^N$ sets. This evaluation is not feasible for large $N$. However, by promoting the sparsity of $\boldsymbol{\alpha}_l$, we can predict the locations of the nonzero elements, hence the evaluation complexity will be dramatically reduced as we explained in section 4.2.2. Next, we breakdown the terms of the above estimator and show how we evaluate them.

For a given set $\mathcal{S}_l$ of supports of the nonzero elements of $\boldsymbol{\alpha}_l$, we can express $\mathbf{y}_l$ in terms of those nonzero elements and the corresponding columns of $\mathbf{V}_l$ as follows

$$\mathbf{y}_l = \mathbf{V}_{l,\mathcal{S}_l}\boldsymbol{\alpha}_{l,\mathcal{S}_l} + \mathbf{w}_l \tag{5-10}$$

where $\boldsymbol{\alpha}_{l,\mathcal{S}_l}$ is the nonzero elements of $\boldsymbol{\alpha}_l$, and $\mathbf{V}_{l,\mathcal{S}_l}$, is the selected columns of the matrix $\mathbf{V}_l$ corresponding to the set $\mathcal{S}_l$. Computing $\mathbb{E}[\boldsymbol{\alpha}_l|\mathbf{y}_l,\mathcal{S}_l]$ require the knowledge the distribution of the nonzero components of the vector $\boldsymbol{\alpha}_l$, which is difficult in TWRI due to the reflectivity variation of targets [47]. Instead, we replace it with the best unbiased estimator (BLUE) as:

$$\mathbb{E}[\boldsymbol{\alpha}_l|\mathbf{y}_l,\mathcal{S}_l] \leftarrow \left(\mathbf{V}_{l,\mathcal{S}_l}^{\mathrm{H}}\mathbf{V}_{l,\mathcal{S}_l}\right)^{-1}\mathbf{V}_{l,\mathcal{S}_l}\mathbf{y}_l. \tag{5-11}$$

Afterword, Bayes rule is used to express the posterior in (5-9) as

$$\mathrm{p}(\mathcal{S}_l|\mathbf{y}_l) = \frac{\mathrm{p}(\mathbf{y}_l|\mathcal{S}_l)\mathrm{p}(\mathcal{S}_l)}{\mathrm{p}(\mathbf{y}_l)}. \tag{5-12}$$

The probability $\mathrm{p}(\mathbf{y}_l)$ in the denominator is a common scaling factor for all terms in the summation and can be eliminated.

We assume that some elements of $\boldsymbol{\alpha}_l$ are more probable to be nonzero than others, thus those elements will be assigned with higher probability. Accordingly, the prior $\mathrm{p}(\mathcal{S})$ can be computed using non-identically distributed Bernoulli distribution as

$$\mathrm{p}(\mathcal{S}_l) = \prod_{i \in \mathcal{S}_l} \wp_{l,i} \prod_{j \in \{1,\ldots,N\} \setminus \mathcal{S}_l} (1 - \wp_{l,j}), \qquad (5\text{-}13)$$

where, $\wp_{l,i}$, is the probability of the $i^{\mathrm{th}}$ element of $\boldsymbol{\alpha}_l$ to be nonzero.

Since the distribution of $\boldsymbol{\alpha}_l$ is unknown, finding $\mathrm{p}(\mathbf{y}_l|\mathcal{S}_l)$ is impossible. However, we noticed that $\mathbf{y}_l$ is composed of two components, the first is a vector in the subspace spanned by columns of $\mathbf{V}_{l,\mathcal{S}_l}$. The second is in the additive white Gaussian noise. Hence, we can project $\mathbf{y}_l$ on the orthogonal complement matrix of $\mathbf{V}_{l,\mathcal{S}_l}$ in order to eliminate the non-Gaussian components of $\mathbf{y}_l$ [47]. The orthogonal complement matrix is defined by

$$\mathbf{V}_{l,\mathcal{S}_l}^{\perp} = \mathbf{I} - \overline{\mathbf{V}}_{l,\mathcal{S}_l} = \mathbf{I} - \mathbf{V}_{l,\mathcal{S}_l}\left(\mathbf{V}_{l,\mathcal{S}_l}^{\mathrm{H}}\mathbf{V}_{l,\mathcal{S}_l}\right)^{-1}\mathbf{V}_{l,\mathcal{S}_l}^{\mathrm{H}}. \qquad (5\text{-}14)$$

This projection leads to $\mathbf{V}_{l,\mathcal{S}}^{\perp}\mathbf{y} = \mathbf{V}_{l,\mathcal{S}}^{\perp}\mathbf{w}_l$, which is a vector of Gaussian distribution with zero mean and covariance matrix given by

$$\begin{aligned}\mathbf{C} &= \mathbb{E}\left[\left(\mathbf{V}_{l,\mathcal{S}_l}^{\perp}\mathbf{w}_l\right)\left(\mathbf{V}_{l,\mathcal{S}_l}^{\perp}\mathbf{w}_l\right)^{\mathrm{H}}\right] \\ &= \mathbf{V}_{l,\mathcal{S}_l}^{\perp}\mathbb{E}\left[\mathbf{w}_l\mathbf{w}_l^{\mathrm{H}}\right]\mathbf{V}_{l,\mathcal{S}_l}^{\perp}{}^{\mathrm{H}} \\ &= \mathbf{V}_{l,\mathcal{S}_l}^{\perp}\sigma_{\mathbf{w}_l}^2\mathbf{V}_{l,\mathcal{S}_l}^{\perp}{}^{\mathrm{H}} \\ &= \sigma_{\mathbf{w}_l}^2\mathbf{V}_{l,\mathcal{S}_l}^{\perp}.\end{aligned} \tag{5-15}$$

Therefore, the likelihood $\mathrm{p}(\mathbf{y}_l|\mathcal{S}_l)$ can be expressed as

$$\mathrm{p}(\mathbf{y}_l|\mathcal{S}) = \frac{1}{\sqrt{\left(2\pi\sigma_{\mathbf{w}_l}^2\right)^M}}\exp\left(-\frac{1}{2\sigma_{\mathbf{w}_l}^2}\left(\mathbf{V}_{l,\mathcal{S}}^{\perp}\mathbf{y}_l\right)^{\mathrm{H}}\mathbf{C}^{-1}\left(\mathbf{V}_{l,\mathcal{S}}^{\perp}\mathbf{y}_l\right)\right) \tag{5-16}$$

Now we can find the posterior $\mathrm{p}(\mathcal{S}_l|\mathbf{y}_l)$ by substituting (5-13) and (5-16) in (5-12), subsequently, we have all ingredients for evaluating the MMSE in (5-9). Nevertheless, evaluating the sum over all sets of $\boldsymbol{\mathcal{S}}_l$ is computationally expensive. Instead, and by promoting sparsity of $\boldsymbol{\alpha}_l$, we define a new set, $\mathfrak{S}_l$, which contains the sets, $\mathcal{S}_l$, with significant posteriors $p(\mathcal{S}_l|\mathbf{y}_l)$. That is, $\mathfrak{S}_l$, contains sets of the supports with significantly high value of $p(\mathcal{S}_l|\mathbf{y}_l)$. Hence, the MMSE in (5-9) will be approximated as

$$\widehat{\boldsymbol{\alpha}}_{\mathrm{AMMSE}} \cong \sum_{\mathcal{S}_l\in\mathfrak{S}_l} p(\mathcal{S}_l|\mathbf{y}_l)\mathbb{E}[\boldsymbol{\alpha}_l|\mathbf{y}_l,\mathcal{S}_l]. \tag{5-17}$$

Next, we show how we find the elements of the set $\mathfrak{S}_l$.

### 5.3.1 Finding the Dominant Supports Set

In order to build the set $\mathfrak{S}_l$, we define "*support selection metric*" as the logarithmic posterior

$$\begin{aligned} \nu(\mathcal{S}_l, \mathbf{y}_l) &\triangleq \ln\big(p(\mathcal{S}_l|\mathbf{y}_l)\big) \\ &= -\frac{1}{2\sigma_{\mathbf{w}_l}^2}\left\|\mathbf{V}_{l,\mathcal{S}_l}^{\perp}\mathbf{y}_l\right\| + \sum_{i\in\mathcal{S}_l}\ln\big(\wp_{l,i}\big) + \sum_{j\in\{1,\dots,N\}\setminus\mathcal{S}_l}\ln\big(1-\wp_{l,j}\big). \end{aligned} \tag{5-18}$$

The set $\mathfrak{S}_l$ is built sequentially in a greedy manner. At the outset, $\nu(\mathcal{S}_l, \mathbf{y}_l)$, is computed for a single nonzero element, i.e., $\mathcal{S}_l = \{1\}, \{2\}, \dots, \{N\}$. Then we choose the support corresponding to the largest value of $\nu(\mathcal{S}_l, \mathbf{y}_l)$ as the first element of $\mathfrak{S}_l$. Afterward, we evaluate $\nu(\mathcal{S}_l, \mathbf{y}_l)$ for $\mathcal{S}_l$ of two elements, given that the first element is the one that was chosen in the previous step. The element corresponding to the largest value of $\nu(\mathcal{S}_l, \mathbf{y}_l)$ will be chosen as the second element in $\mathfrak{S}_l$. Then $\nu(\mathcal{S}_l, \mathbf{y}_l)$ is evaluated with three elements in $\mathcal{S}_l$, again, the first two are the ones were selected in the previous step. This procedure continues until a termination criterion is satisfied. Figure 5-2 shows an example of the greedy approach for a vector of length $N = 7$, and number of nonzero elements $K = 4$. Each row in the Figure 5-2 shows a single step for selecting one element of $\mathfrak{S}_l$, the selected elements are highlighted with red.

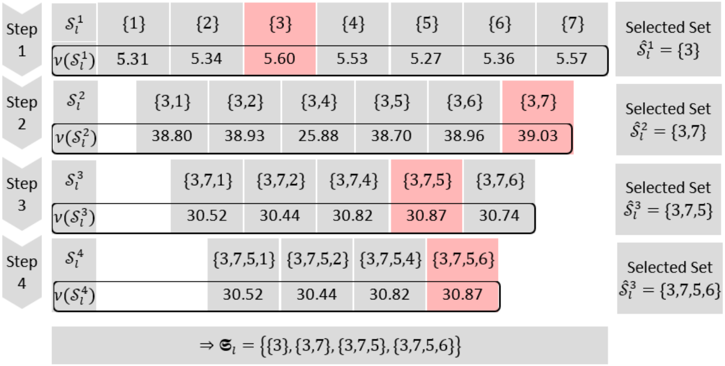

*Figure 5-2 Illustration on how selection matric* $\nu(\mathcal{S}_k)$ *is evaluated.*

The number of iteration for building $\mathfrak{S}_l$ can be set slightly more than the number of targets, if the number of targets is known. Otherwise, the iteration can be terminated when the following condition is met $\mathrm{p}(|\mathfrak{S}_l| > K), = \frac{1}{2}\mathrm{erfc}\left(\frac{K - N\wp_l}{\sqrt{2Np(1-\wp_l)}}\right) \leq \gamma$ , where $\gamma$ is a small number [47], and $\boldsymbol{\wp}_l = \max(\wp_{l,n})\ \forall n$.

Note that the value of the selection metric $\nu(\mathcal{S}_l, \mathbf{y}_l)$, in (5-18), depends on the probabilities, $\wp_{l,i}$ and $\wp_{l,j}$, of the elements of $\boldsymbol{\alpha}_l$ being non-zeros. If provided accurately, these probabilities will lead for better selection of the true locations of the nonzero elements of $\boldsymbol{\alpha}_l$, We exploit this dependency to enable cooperation between antenna elements. Where each element estimates a probability vector, $\boldsymbol{\mathcal{P}}_l = \{\wp_{l,1}, \wp_{l,2}, \dots, \wp_{l,N}\}$, and shares it with a selected antenna element in the array.

In the following section, we show how each antenna element marginalize over the posterior $p(\mathcal{S}_l|\mathbf{y}_l)$ to produce the probability vector $\boldsymbol{\mathcal{P}}_l$ to be passed to the next selected antenna.

### 5.3.2 Finding the Marginal Probability Vector

Evaluating the selection metric $\nu(\mathcal{S}_l, \mathbf{y}_l)$ in (5-18) returns the posteriori $p(\mathcal{S}_l|\mathbf{y}_l)$ for a given set of supports $\mathcal{S}_l$. Since $\nu(\mathcal{S}_l, \mathbf{y}_l)$ is evaluated for different sets, we marginalize over all $p(\mathcal{S}_l|\mathbf{y}_l)$ to obtain the probability of each element for the vector $\boldsymbol{\alpha}_l$ for being nonzero element as

$$p(\alpha_i|\mathbf{y}_l) = \wp_{l,i} = \sum_{\alpha_i \cap \mathcal{S}_j \neq \phi} p(\mathcal{S}_j|\mathbf{y}_l) \quad \forall i, j. \tag{5-19}$$

Once $p(\alpha_i|\mathbf{y}_i)$ is calculated for all values pixels, the antenna at the $l$-th location shares its probability vector $\boldsymbol{\mathcal{P}}_l$ with a selected antenna in the SAR array as demonstrated in the Section 5.4.

### 5.3.3 Updating the Noise Variance

It can, also, be observed that the selection metric in (5-18), is a function of the noise variance $\sigma^2$. We assume that the noise variance is the same at all elements, hence it can be refined at each location. At the first location, the algorithm is initiated with noise variance $\sigma_1^2 = \frac{1}{4}\sigma_{\mathbf{y}_1}^2$, then at the next locations the variance is updated as

$$\sigma_l^2 = \text{var}(\mathbf{y}_{l-1} - \boldsymbol{\Phi}_l \hat{\boldsymbol{\alpha}}_{l-1}). \tag{5-20}$$

The execution flow of the above algorithm is detailed Table 5-1.

*Table 5-1 Structure Based Bayesian Matching Pursuit*

```
Mandatory Inputs: Measurements vector $\mathbf{y}_l$, Measurement Matrix $\mathbf{V}_l$,
Optional Inputs: Probability vector $\boldsymbol{\mathcal{P}}_l$, Noise Variance $\sigma^2$
Initialization: $\mathcal{A} \leftarrow \{1,2,\dots,N\}$, $\mathcal{B} \leftarrow \mathcal{A}$, $i = 1$,
                $\mathcal{S}_\star = \phi$, $\boldsymbol{\mathcal{S}}_\mathrm{d} = \phi$,
                $Posteriors = \phi$, $Expectations = \phi$
while termination criterion is not met do
    $\boldsymbol{\mathcal{C}} \leftarrow \left\{\mathcal{S}_\star \cup \{s_1\}, \mathcal{S}_\star \cup \{s_2\}, \dots, \mathcal{S}_\star \cup \left\{s_{|\mathcal{B}|}\right\} \middle| s_j \in \mathcal{B}\right\}$
    compute $\left\{\nu\left(\mathcal{S}_j\right) \forall j, |\mathcal{S}_j \in \boldsymbol{\mathcal{C}}\right\}$                 eq. (5-18)
    find $\mathcal{S}_\star \in \boldsymbol{\mathcal{C}}$ s.t. $\nu(\mathcal{S}_\star) \geq \max \nu\left(\mathcal{S}_j\right)\ \forall j$
    compute $p(\mathcal{S}_\star|\mathbf{y})$                                   eq.(5-18)
            $\mathbb{E}[\boldsymbol{\alpha}|\mathbf{y}, \mathcal{S}_\star]$                                   eq. (5-11)
    $Posteriors \leftarrow \{Posteriors, p(\mathcal{S}_\star|\mathbf{y})\}$
    $Expectations \leftarrow \{Expectations, \mathbb{E}[\boldsymbol{\alpha}|\mathbf{y}, \mathcal{S}_\star]\}$
    $\mathfrak{S}_{l\cdot} \leftarrow \{\mathfrak{S}_{l\cdot}, \mathcal{S}_\star\}$
    $\mathcal{B} \leftarrow \{\mathcal{A} \backslash \mathcal{S}_\star\}$
    $i = i + 1$
end while
compute $\widehat{\boldsymbol{\alpha}}_\mathrm{AMMSE}$                                      eq. (5-17)
        $\hat{\sigma}_l^2$                                              eq. (5-20)
        $\boldsymbol{p}(\widehat{\boldsymbol{\alpha}}_i|\mathbf{y}_l)\ \ \forall i$                                  eq. (5-19)
Return $\widehat{\boldsymbol{\alpha}}_\mathrm{AMMSE}$, $\hat{\sigma}^2$, $\boldsymbol{p}(\widehat{\boldsymbol{\alpha}}_i|\mathbf{y})\ \ \forall i$
```

## 5.4 Sharing Information between Antennas

In this section, we demonstrate three type of statistical information that are shared between the antenna elements of the system. The first is the probability of each pixel for being nonzero pixel (i.e., non-target pixel). The second is the normalized amplitude of the estimated pixels at each location. Lastly, we share the searching sets for the nonzero pixels with their corresponding probability of being nonzero pixels.

### 5.4.1 Sharing Mechanism

The aim of sharing statistical information between the antenna elements is to place more emphasis on the nonzero pixels "target-pixels" of the desirable scene. At the same time, sharing information should de-emphasize the pixel of ghosts (effects of multipath). This can be achieved by sharing information with the antenna of the least multipath correlation. In other words, since the pixels of the actual targets are the same for all antennas, while the ghost-pixels are highly uncorrelated at the extreme-ends of the antenna array [118], therefore, each antenna shares information with its analogous antenna at the extreme ends of the array. The algorithm starts calculating the information at the first antenna, this information is then shared with an antenna in its opposite end in the array as depicted in Figure 5-3. This procedure is continued until all elements in the array contribute to the statistical information.

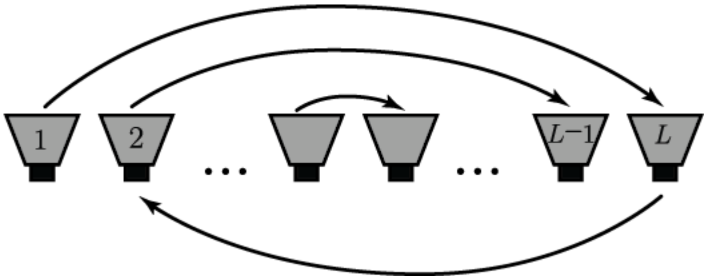

*Figure 5-3 Scheme of information sharing between antenna elements in the SAR array*

The image reconstruction consists of the following steps, these steps are depicted in Figure 5-4:

1. The measurement vector $\mathbf{y}_l$ and the measurement matrix $\mathbf{V}_l$ are passed to the proposed Bayesian estimation algorithm, expounded in Table 5-1, to extract statistical information of the image pixels at the $l^{\text{th}}$ location.
2. This statistical information is shared with a selected antenna in the SAR array as per Figure 5-3.
3. The new antenna uses the received information along with its own measurement vector $\mathbf{y}_l$ and measurement matrix $\mathbf{V}_l$ to update the statistical information of the image.
4. The updated statistical information is then share with another selected antenna in the array until these statistical information is updated by all antennas in the array.
5. Th final statistical information is given to all elements in the array.
6. Each antenna uses these statistical Information and its own measurement vector and measurement matrix to reconstruct a sub-image at its location.

All sub-images are the averaged to produce the final radar image as in (5-6).

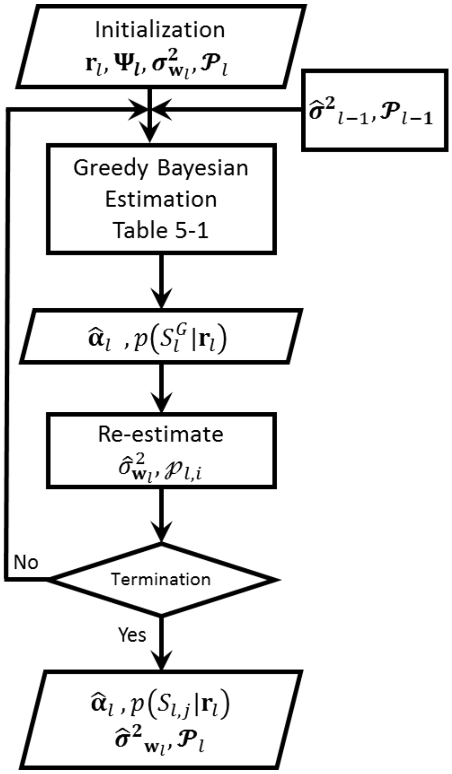

*Figure 5-4 Flowchart for the reconstruction algorithm with information sharing*

### 5.4.2 Sharing Probability Vector

The key factor for a superior performance of the developed algorithm, is the right selection of the possible set for the nonzero elements of the vector $\boldsymbol{\alpha}_l$. It can be observed form equation (5-18) the probability $\wp_{l,i}$ contributes for the value of the selection metric. Hence, providing the right estimate of $\wp_{l,i}$ would enhance the accuracy of selecting the right set of nonzero elements.

Using the marginal probability vector, given by equation (5-19), in this scenario, each antenna calculates the probability vector $\boldsymbol{\mathcal{P}}_l$ and then share it with the next selected antenna as per the sharing scheme in 5.4.1.

### 5.4.3 Sharing Normalized Amplitude Vector

As a role of thumb, it has been observed that pixels with high amplitude in the estimated image vector $\widehat{\boldsymbol{\alpha}}_l$ are associated with high probability, $\mathcal{p}_{l,i}$ in the probability vector $\mathcal{P}_l$. Therefore, in this type of sharing scenario, instead of providing the algorithm with the probability vector $\boldsymbol{\mathcal{P}}_l$, each antenna normalize its estimated vector $\widehat{\boldsymbol{\alpha}}_l$ and then provided with the next selected antenna as per the sharing scheme in 5.4.1.

### 5.4.4 Sharing Searching Sets of Nonzero Pixels

In this sharing scenario, the shared statistical information is the expected set of the nonzero pixels of the image. As detailed in Section 5.3.1, the selection metric (5-18) should be evaluated in a greedy manner over all pixels in the image vector $\boldsymbol{\alpha}_l$ to find the set of the significant posteriors $\mathfrak{S}_l$. In this scenario, the evaluation is done over selected sets that is provided by another antenna in the array. Once the first antenna estimates its image vector $\boldsymbol{\alpha}_l$, it shares the support of the nonzero pixels in the vector, and their corresponding probabilities $\mathcal{p}_{l,i}$ with a selected antenna in the array as per the sharing scheme in 5.4.1. The selection metric is then evaluated over those sets and the process is repeated.

## 5.5 Results and Discussion

This section presents results based on synthesized data, generated by MATLAB-based simulator, and practical data measured in real-life environment. Two scenarios are considered, the first is the multipath-free scenario, where multipath component are not included in the radar return. In the second scenario, multipath is included. Individual experiments are firstly presented for visual inspection.

Two criteria are used to evaluate the algorithm, the first is the error performance over different levels of SNR. The second is the error performance over the different compression rate. The error is defined as following

$$\text{Relative Error} = \frac{\|\boldsymbol{\alpha} - \hat{\boldsymbol{\alpha}}\|^2}{\|\boldsymbol{\alpha}\|^2}. \tag{5-21}$$

### 5.5.1 Results Based on MATLAB-Synthesized Data

For visual inspection, in this section we start by validating the cooperative algorithm over individual experiments using a scene of four targets. Then we present the error performance over different SNR levels and different compression ratios. All sharing schemes, as elaborated in Section 5.4, are employed in both scenarios.

In the following experiments, the scene consists of four targets, with crossrange and downrange of $6m$. A uniform linear monostatic array composed of 40-elements spaced out by 5.00cm is used to capture the image. The center of the array is considered to be the origin of the system. A series of 1000 monochromatic waves to shape an UWB signal occupying a spectrum between 1 and 10GHz is employed for the scene interrogation.

The next experiments demonstrate two scenarios, the first uses a radar return with no multipath effects; it aims to validate the performance over noisy environments as shown in Figure 5-7. The second uses the same experimental setup but with consideration of the multipath effects caused by the surrounding walls. Figure 5-8 shows the effectiveness of information sharing for suppressing the effects of multipath. In bother scenarios, the front wall contribution was suppressed by spatial filtering.

The original scene is shown in Figure 5-5 (a), the received radar returns are contaminated with AWGN with $SNR = -5\text{dB}$. Figure 5-5 (b) shows the reconstructed image without antenna cooperation, i.e., no information is shared between antennas. The error in this case is 5.1. With visual inspection, “Target 3” is undetected; “Target 2” and “Target 4” are weakly detected. Figure 5-5 (c) shows the reconstructed image when the antennas share the probability vector $\boldsymbol{\mathcal{P}}_l$, as explained in Section 5.4.2. This sharing scheme results in the best error performance, where the relative error is dropped to 0.52. Figure 5-5 (d) shows the reconstructed image when the second sharing schemed is implemented, as expound in Sections 5.4.3, with error of 0.54. The reconstructed image of the last sharing schemes, as elaborated in Section 5.4.4, is shown in Figure 5-5 (e) with error of 0.61.

The results in Figure 5-6 visualize the performance of the cooperative algorithm in a multipath environment. Figure 5-6 (a) shows the ground-truth scene. In order to illustrate the effects of multipath on conventional radar imaging, DSB is implemented and shown in Figure 5-6 (b), where three ghosts appear in the image. In rich-multipath environments, and when antenna cooperation is not employed, the our algorithm fails to reconstruct the scene as shown in Figure 5-6 (c). However, when statistical information is shared, the algorithm succeeds in reconstructing the image, with error of 0.52, as well as in suppressing the ghosts as shown in Figure 5-6 (d). The above results can be summarized in Table 5-2.

*Table 5-2 Error comparison for different sharing scenario at* $SNR = -5dB$

| **Sharing Scenario** | **Error in when multipath is not considered** | **Error when Multipath is considered** |
|---|---|---|
| No Shared Information | 5.1 | 6.8 |
| Sharing probability vector | 0.52 | 0.71 |
| Sharing normalized estimated image | 0.54 | 0.9 |
| Sharing probability vector and searching set | 0.61 | 0.8 |

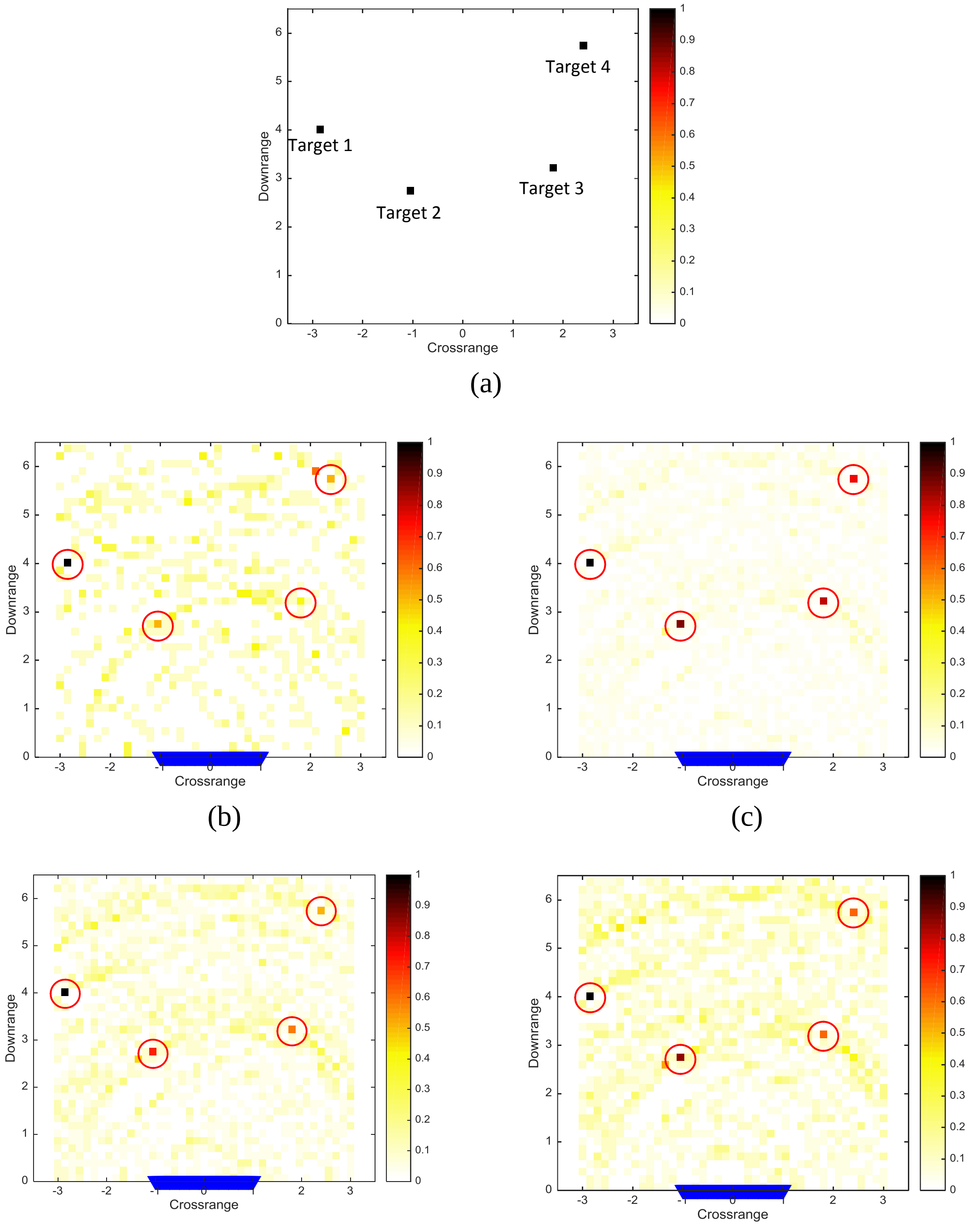

(a)

(b) (c)

(d) (e)

*Figure 5-5 Using the cooperative algorithm to recover a scene of four targets under* $SNR = -5dB$*, Multipath effects are not included. (a) Original Scene. (b) Reconstructed image with no information sharing Error=5.1. (c) Reconstructed image with sharing probability vector* $\mathcal{P}_l$*. Error=0.54. (d) Reconstructed image with sharing Points (normalized estimated vector). Error=0.64. (e) Reconstructed image with sharing possible sets of the nonzero pixels. Error=0.61.*

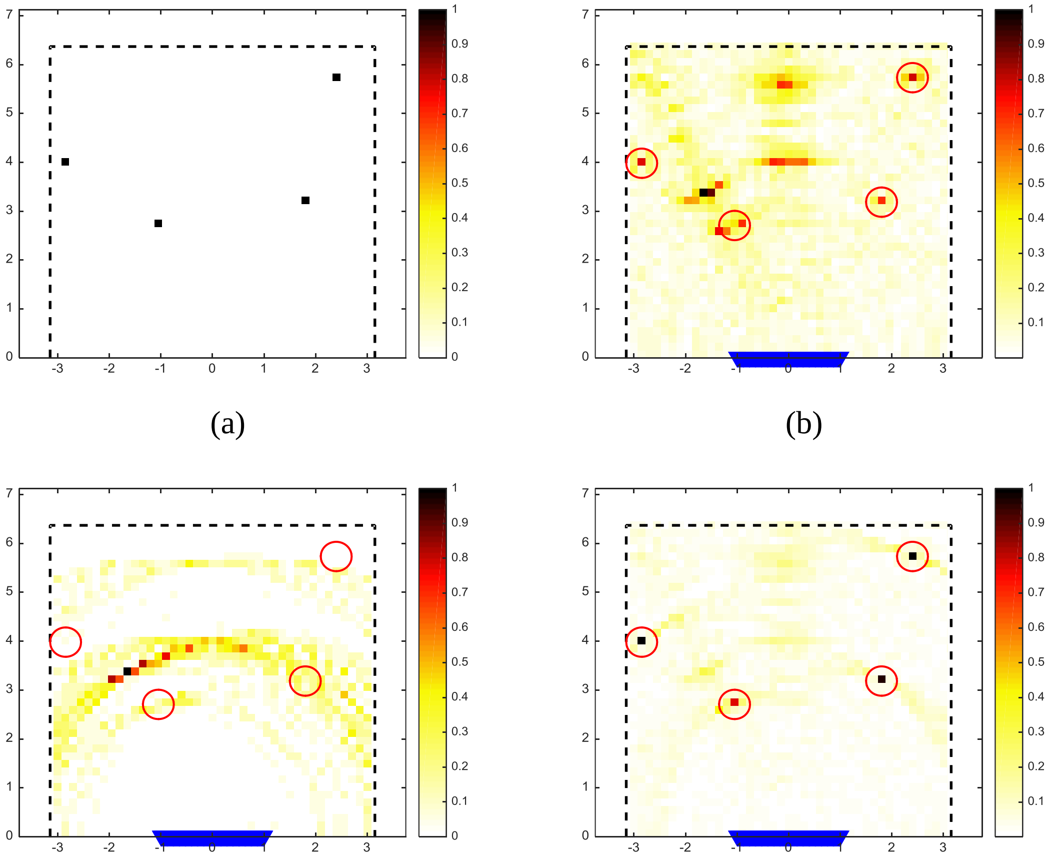

(a) (b)

(c) (d)

*Figure 5-6 Using the cooperative algorithm to recover a scene of four targets under* $SNR = -5dB$, *Multipath effects are included. (a) Original Scene. (b) Recovered image using conventional DSB. Error=6.8. (c) Reconstructed image with no information sharing. Error=5.3. (d) Reconstructed image with sharing probability vector* $\mathcal{P}_l$. *Error=0.71.*

#### 5.5.1.1 Error Performance in Noisy Environment

In this section, we used the same setup of the above experiments to evaluate the performance over different SNR levels. The error is averaged over 500 trials at each SNR level. Target's locations and reflectivity are selected randomly for each trial. Figure 5-7 shows the error performance for the multipath-free and the multipath environments. All sharing schemes, as detailed in 5.4 , were employed for both environments. At high SNR levels, the performances of the sharing schemes are comparable. At low SNR levels, sharing the probability vectors overcomes other sharing schemes.

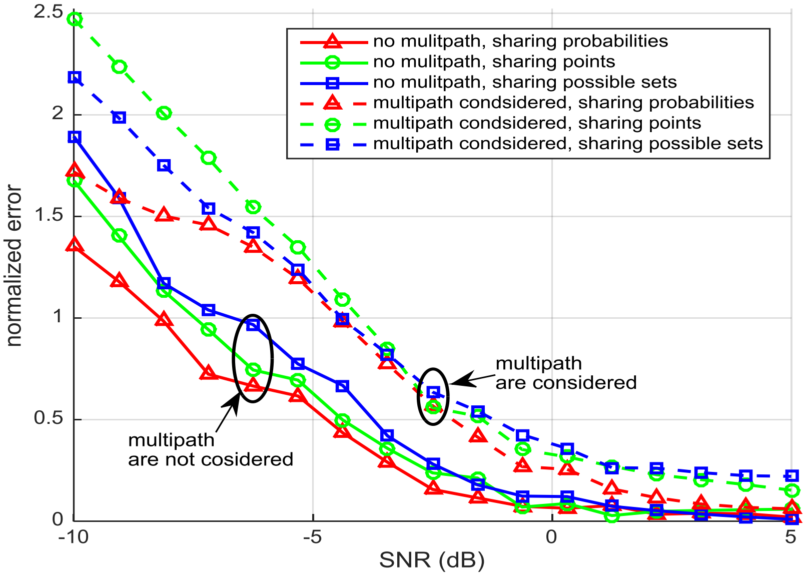

*Figure 5-7 Error performance versus different SNR levels*

### 5.5.1.2 Compression Performance

This section evaluates the error performance against the compression ratio. Data compression in this context is interpret as the ratio of the used frequencies $M$ to the number of frequencies $Q$ that are required by the conventional TWRI approaches. Figure 5-8 shows the error performance for different compression ratios. We used 500 noise-free trials and average their resultant error to produce the error value at each ratio. The locations of targets and their reflectivity are selected randomly at each trial. The cooperative algorithm behaves better in multipath-free environment especially when the compression ratio is between 40-50 percent of the data as shown in Figure 5-8.

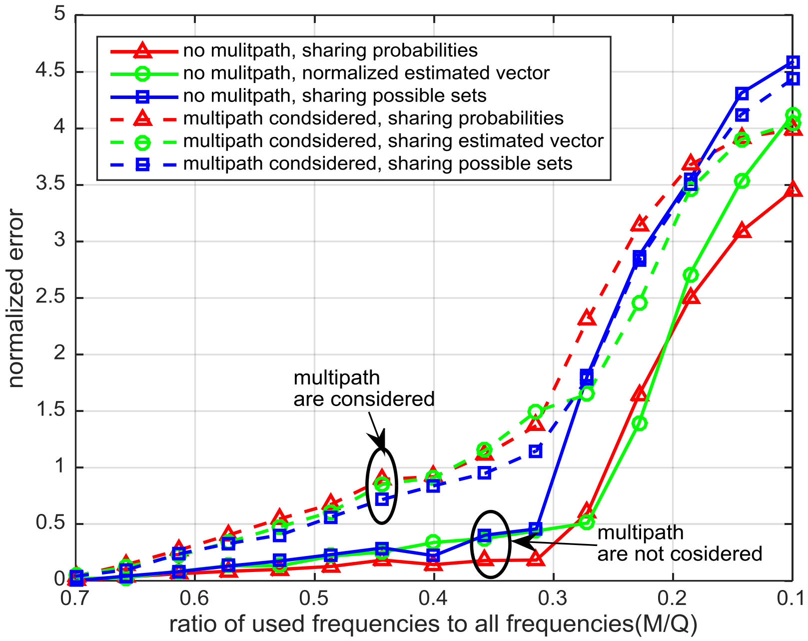

*Figure 5-8 Error performance over different compression rate*

### 5.5.2 Performance over Practical Data

A wideband SAR system was setup in a real-life classroom to validate the proposed algorithm in a multipath environment. The system is used to image a scene of four target inside a classroom. A schematic sketch of the room and a photo of the scene are shown in Figure 5-9 (a)-(b) respectively. The system specifications and more details about the scene are shown in Chapter 6 and in Table 6-2. Figure 5-9 (c) shows the reconstructed image using DSB algorithm; three ghosts appear in the recovered image due to the effects of multipath (the ghost are highlighted by blue stars). We used the cooperative algorithm to recover the scene as shown in Figure 5-9 (d), the cooperative algorithm helped in enhancing the recovery of the targets and in suppressing the effects of the multipath.

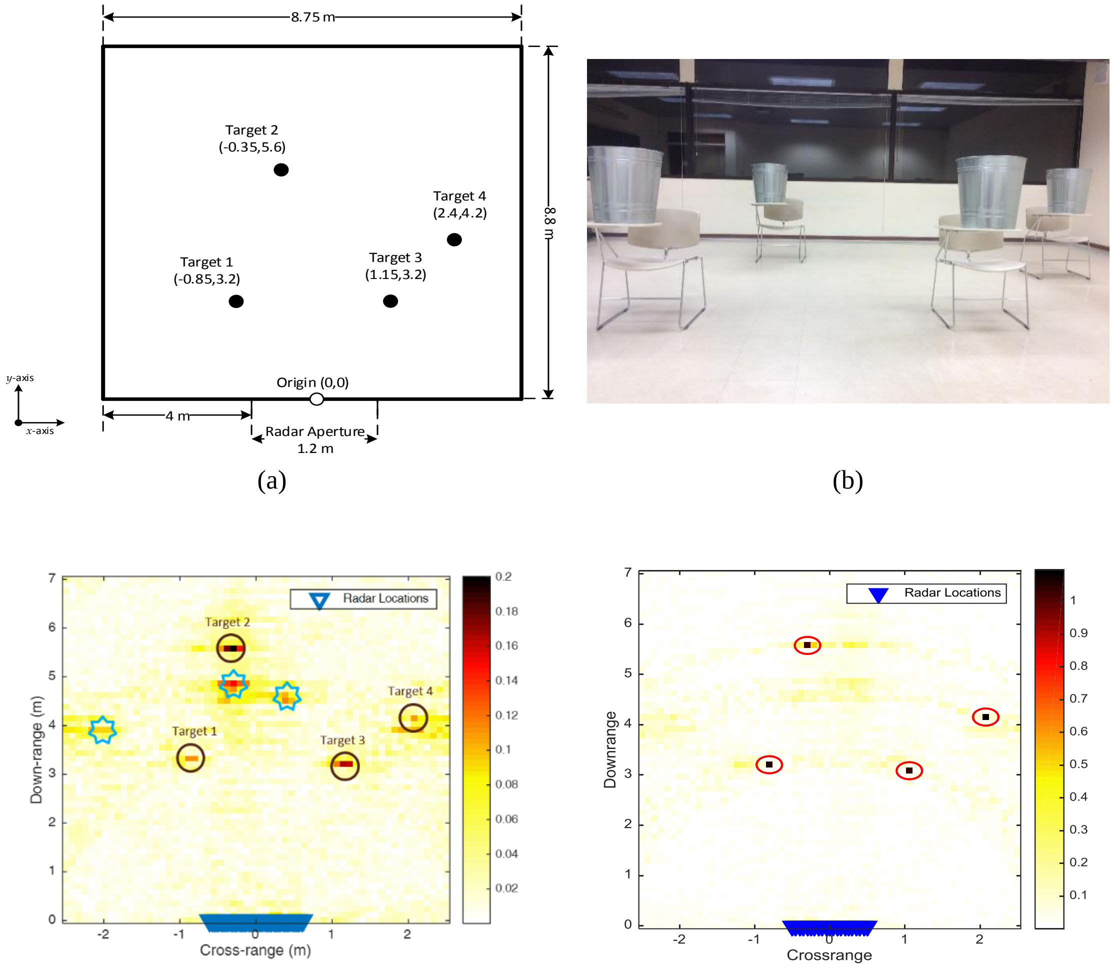

(a) (b)

(c) (d)

*Figure 5-9 Validating the cooperative algorithm in practical multipath environment (a) Sketch of the scene setup. (b) Scene setup in a classroom. (c) Recovered Scene using DSB. (d) Reconstructed Scene using the cooperative algorithm*

## 5.6 Conclusion

This chapter modified the proposed Bayesian algorithm to take advantage of the antenna correlation to enhance the performance of the image reconstruction. Each antenna shares statistical information about the scene with a selected antenna in the array. Three scenario were used for sharing the statistical information. The first is sharing probability of the pixels for being target-pixels, this scenario enhances the reconstruction quality by 56% at SNR$=0\text{dB}$. The second, is sharing "points" which is the normalized estimated of the pixels. Lastly, is sharing the expected locations of the target pixels and their corresponding probability for being target pixels. The latter two scenarios have relatively equivalent error performance, their enhancement for the reconstruction quality is 40% at $\text{SNR}=0\text{dB}$.

Based on synthetic and practical data, capitalizing on the antenna correlation has enhanced the reconstruction quality and suppressed the effects of multipath.

Chapter 6

# TWRI-Simulator and Practical Implementation

## 6.1 Introduction to TWRI-Simulation and Implementation

This chapter presents a MATLAB-based simulator and a set of practical TWRI data that were developed throughout the work of this dissertation. The objective of this chapter is to offer tools and a data-bank of practical data for the research community in the subject matter.

Recent researches were paying a lot of efforts for addressing and resolving the challenges of indoor radar imaging (IRI), such as multipath exploitation [2], suppressing wall clutters [119], front wall mitigations [120], and others. In most of the reviewed literature, the available IRI solutions and algorithms were evaluated over simulated data or over an idealized “controlled” environment. Based on the state of the art modelling, our developed simulator takes into account most of the TWRI phenomena, such as multipath, front wall reverberation, etc. The simulator is user friendly and allows the user to select and generate the radar return in different environments.

In addition to the simulator, a SAR was built and equipped with UWB antenna. Several IRI experiments are performed in fully uncontrolled realistic environments. No an echoic chamber or radio frequency (RF) absorbers were used. The conducted experiments were designed to account for numerous scenarios. The produced row-data and the experimental setups, sketches, and photos will be made available for interested researchers. The shared high-resolution data can be used to evaluate IRI-related algorithms/methodologies under realistic circumstances.

Producing high resolution IRI images requires transmitting ultra-wideband (UWB) signal and using antenna with long aperture. The former controls downrange resolution while the latter controls the crossrange resolution [80]. UWB signals can be achieved by transmitting an ultrashort-pulse or by transmitting a sequence of monochromic signals that sweep certain frequency band. The former is called impulse-radar and it is rarely used in in IRI applications due to its complexity [74]. The latter is very common in IRI applications and it is adopted in in all experiments [80]. The available IRI experiments, in the literature, compromise between the high frequency for better down range resolution and the low frequency for wall-penetration as in [121–123].

As a practice, IRI technology uses UWB directional antennas, in particular antennas like horn [76, 121, 123] or Vivaldi [122] are used. Long antenna aperture is obtained by using the concept of synthetic aperture radar (SAR) [76, 121, 123]. The work in [121] transmits signal stepped frequency continuous wave (SFCW) of 2-3GHz bandwidth at different locations to form the long aperture which led to a prolong acquisition time. The work in [124] used an antenna array, which is made of 16 Vivaldi antennas in order to form the long aperture.

Bistatic and monostatic configurations are two possible configurations for the IRI systems. In bistatic radar, the transmitter and the receiver have different locations [121, 122]. Monostatic radar transmits and receives the signal at the same location[74]. Monostatic radar has some advantages over the bistatic radar such as simplicity and the ability to use spatial filters for eliminating the clutters of front wall without the need to know the characteristics of the wall [76].

Existence of the walls in indoor environment has added some challenge to the applications of IRI. EM waves passing through walls are subject to amplitude and phase distortion. Wall characterization was the objective of several indoor radar experiments. Walls can be classified into homogeneous and nonhomogeneous [11]. The wall in reference [121] consists of wood studs that are covered by plywood from one side and gypsum from the other side.

The work in [122] and [124] has conducted IRI experiments for target motion detection. Detecting moving targets is usually easier than detecting stationary targets. The coherent changes in the frames are detected and each frame is subtracted continuously from the previous frame in order to detect the motion.

The rest of the chapter is organized as following. Section 6.2 shows the MATLAB-based TWRI simulator. Section 6.3 illustrates the constructed radar system specifications and the methodology used to do the experiments. Section 6.36.3 presents the hardware design of the SAR system. Section 6.5 shows the practical experiments and the results obtained in each case. Finally, conclusions are drown in Section 6.6.

## 6.2 Indoor TWRI Simulator

In this section, we show the TWRI simulator that was developed during the work of this dissertation. The simulator consists of three user-friendly interfaces. The first inter face allows the user to draw the scene and choose its parameters as depicted in Figure 6-1. In the scene parameter, the user can also select the number of targets in and the phenomena to be included in the generated data.

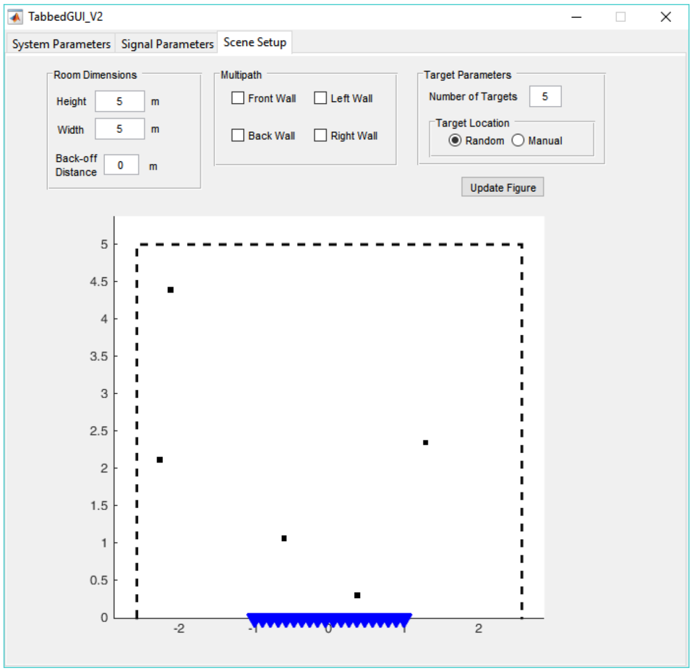

Height 5 m
Width 5 m
Back-off Distance 0 m
☐ Front Wall ☐ Left Wall
☐ Back Wall ☐ Right Wall
Number of Targets 5
● Random ○ Manual

*Figure 6-1 MATLAB interface for the TWRI simulator*

The second interface of the simulator is the Signal Parameters as shown in Figure 6-2 (a). The user can choose the type of the radar system and the characteristic of signal such as the bandwidth and the power. The third interface is the System Parameters, as shown in Figure 6-2 (b), which allows for choosing physical parameters of the system such as type of configuration and the aperture length.

TabbedGUI_V2

System Parameters | Signal Parameters | Scene Setup

Button Group

● SFCW ○ Chirp

○ Impulse

Panel

Bandwidth 2 GHz

Start Frequency 1 GHz

Number of Frequency Bins 1000

Frequency Selection

● Uniformly ○ Entered by user

○ Randomly

TabbedGUI_V2

System Parameters | Signal Parameters | Scene Setup

SAR Configuration

● Monostatic ○ Biostatic

Aperture Length: 2 m

Start Location -1 m

Number of Antenna Locations 20

Antenna Seperation Distance

● Uniformly ○ Entered by user

○ Randomly

(a) (b)

*Figure 6-2 MATLAB interface for entering (a) System parameter (b) Signal prameter*

## 6.3 Practical SAR Platform

A wideband SAR system was built and setup in different rooms at KFUPM-EE department, to produce a bank of realistic radar imaging data. The moving platform is controlled by a microcontroller system which receives commands from the PC via Bluetooth as demonstrated using block diagrams in Figure 6-3. The system is equipped with UWB horn antenna of 18GHz bandwidth as shown in Figure 6-4 (a). We used “Agilent Fielfox N9918A” network analyser, shown in Figure 6-8 (b), of 10GHz bandwidth to illuminate the scene with an UWB signal and received the reflections.

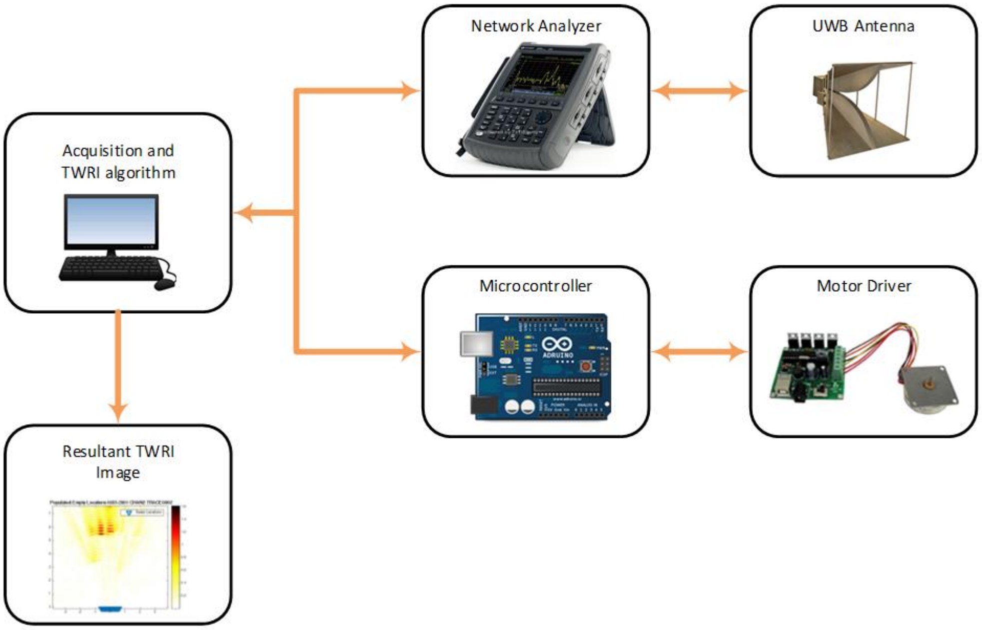

*Figure 6-3 Block diagram of the radar imaging system*


(a) (b)

*Figure 6-4 (a) Moving platform and UWB antenna during imaging process. (b) Full imaging system*

## 6.4 System Setup and Beamforming

In this work, SAR system is used to synthesize a long aperture. A horn UWB antenna of 1-18GHz bandwidth is mounted on a slider, that is controlled by a microcontroller; in order to form the desired aperture. As depicted in Figure 6-5, SAR system is located parallel to the scene of interest. A vector network analyser (VNA) is configured to interrogate the scene with SFCW signal. The monostatic configuration is adopted, where the VNA transmits and receives a series of $N$ monochromic frequencies at each $M$ antenna locations. The system parameters are summaries in Table 6-1.

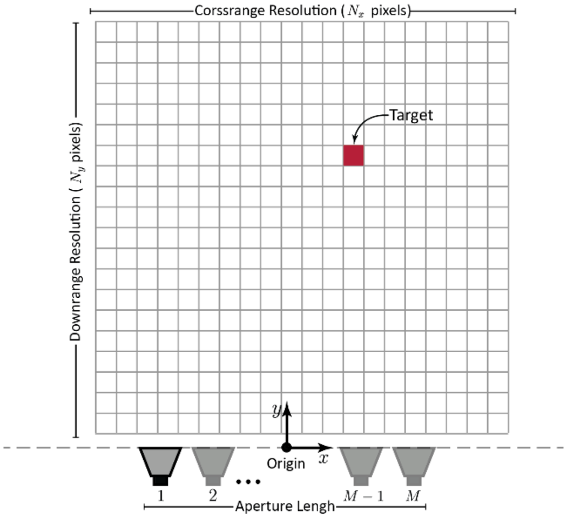

*Figure 6-5Illustration of used radar imaging system*

*Table 6-1 System Parameters*

| | |
|---|---|
| **Type of signal** | Stepped frequency continuous wave |
| **Start frequency** | 1 GHz |
| **Stop frequency** | 4 GHz |
| **Number of frequencies** | 801 |
| **Transmitted power** | 3 dBm |
| **Radar location** | - 0.45 m to 0.45 m |
| **Number of locations** | 31 |
| **Antenna type and Model** | Horn, A-INFOMW JXTXLB-10180 |
| **VNA model** | Agilent Fielfox N9918A |

For a scene of $G$ stationary point targets, we can express the received signal of the $n^{\text{th}}$ frequency and the $m^{\text{th}}$ location as

$$r_{m,n} = \sum_{r=0}^{R-1} \sum_{g=0}^{G-1} \sigma_g^{(r)} \exp\left(-j2\pi f_n \tau_{g,m}^{(r)}\right) + v_{m,n} \tag{6-1}$$

where $R$ is the maximum possible target-radar propagation paths including the direct and excluding target-to-target interactions. $\sigma_g^{(r)}$ is the complex reflectivity of the $g^{\mathrm{th}}$ target when observed through the $r^{\mathrm{th}}$path, $\tau_{g,m}^{(r)}$ is the round trip propagation delay between the location of the $g^{\mathrm{th}}$ target and the $m^{th}$ antenna location along the $r^{th}$ path. $f_n$ is $n^{\mathrm{th}}$ transmitted frequency, $v_{m,n}$ is the additive complex white noise. Note that the direct path is the desired path associated with the actual targets because its corresponding delay will coincide with the focus delay in (6-2) and that predicts the actual location of the target. The other indirect paths "higher-order multipath" are the interaction of the target with the surrounding walls and other object of the scene as detailed in [12]. Unless exploited, multipath would lead to the appearance of false targets in the image known as ghosts, they can be suppressed using different techniques [12].

Generating the IRI is done by dividing the desired scene into $N_x$ pixels in the crossrange and $N_y$ pixels in the downrange, as depicted in Figure 6-5, then delay and sum (DS) algorithm is applied at each pixel to generate the image as [13], [14]

$$I(q) = \frac{1}{MN} \sum_{m=1}^{M} \sum_{n=1}^{N} r_{m,n} \exp\left(j2\pi f_n \tau_{m,q}\right) \tag{6-2}$$

where $q$ is the pixel index, $\tau_{m,q}$ is called the focus delay, which is the delay associated with the round trip time between the $q^{\text{th}}$ pixel and the $m^{\text{th}}$ radar location. The origin of the scene is chosen to be in the middle of the SAR system.

The resolution of the radar image is a measure of the ability of the radar to distinguish between two adjacent targets. More specifically, the downrange resolution, expressed in meter, measures the ability of the radar to resolve distinct targets positioned along the same angular location, but with different downrange. It can be expressed as [1]

$$\Delta R_D = \frac{c}{2B} \tag{6-3}$$

where $c$ is the speed of light, and $B$ is the bandwidths of the system. Crossrange resolution, expressed in meter, measures the ability of the radar to distinguish between two targets placing in the same downrange, but with different angular displacements Cross range resolution can be expressed as:

$$\Delta R_c = \frac{\lambda D}{2L} \tag{6-4}$$

where $\lambda$ is the wavelength of the minimum frequency of the SFCW signal, $D$ is the maximum distance in which the scene is bounded, $L$ is the aperture size.

Next, we show the experimental evaluation of the above-detailed system for four different IRI experiments. Each experiment is chosen to serve certain objectives as detailed below.

## 6.5 Experiments

The first two experiments were conducted in the Telecommunications Research Laboratory (TRL) at King Fahd University of Petroleum & Minerals (KFUPM). In the first experiment, we show the effect of the variation of target's size on the recovered image. The crossrange resolution for the used radar system is examined in experiment 2

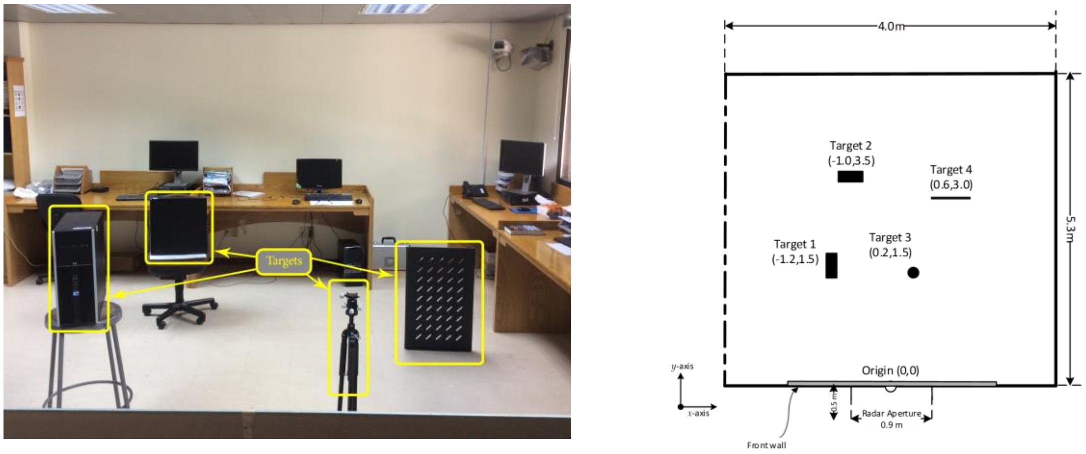

*Figure 6-6 (a) Populated scene of experiment 1 (b) Sketch of the top view of scene of experiment 1*

Experiments 3-4 were conducted inside an empty classroom at KFUPM. Unlike the first two experiments, no front wall was used. The bandwidth, number of antenna locations, and the length of aperture were increased. These two experiments highlight the effects of multipath caused by the surrounding walls and by target-to-target interaction.

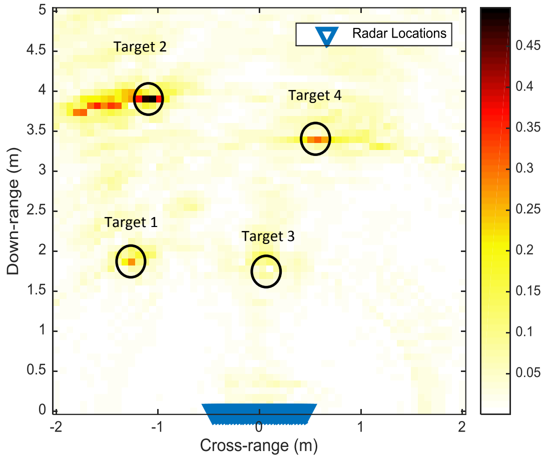

*Figure 6-7 Radar image of experiment 1*

In all experiment, background subtraction was applied to eliminate the scatters of the stationary objects in the vicinity. The empty scene was firstly imaged before adding the targets, this produced the (background scene data). The targets were then added to the scene, and the scene was imaged again from exact antenna locations of the empty scene, this produced (the populated scene data). Background data were subtracted from the populated data, then DS algorithm was applied to produce the image.

### 6.5.1 Experiment 1: The effect of the size and shape-variation of the targets

In this experiment, four targets are used. The first is a metallic computer case of dimension $0.18\text{m} \times 0.45\text{ m} \times 0.45\text{ m}$. It is placed at distance of $0.5\text{ m}$ from the wall as depicted in Figure 6-6. Its front-side faces the SAR, and it's located on a stool of height $0.76\text{ m}$. The second target is a computer identical to the target one, however its side sided was faced to the SAR. It is placed at a distance of $3.5\text{ m}$ way from the front wall. The third target is a metallic tripod of $0.93\text{ m}$ height thickness of $0.1\text{ m}$. It is placed at a distance of $1.5\text{ m}$. The fourth target is a metallic sheet of dimension of $0.47\text{m} \times 0.75\text{ m}$ that is placed on the floor at a distance of $3\text{ m}$ from the wall. Figure 6-6 (a) shows a photograph of the populated scene, the shoot was taken from above the SAR system. Figure 6-6 (b) shows the top0view sketch of the scene with the dimensions specified.

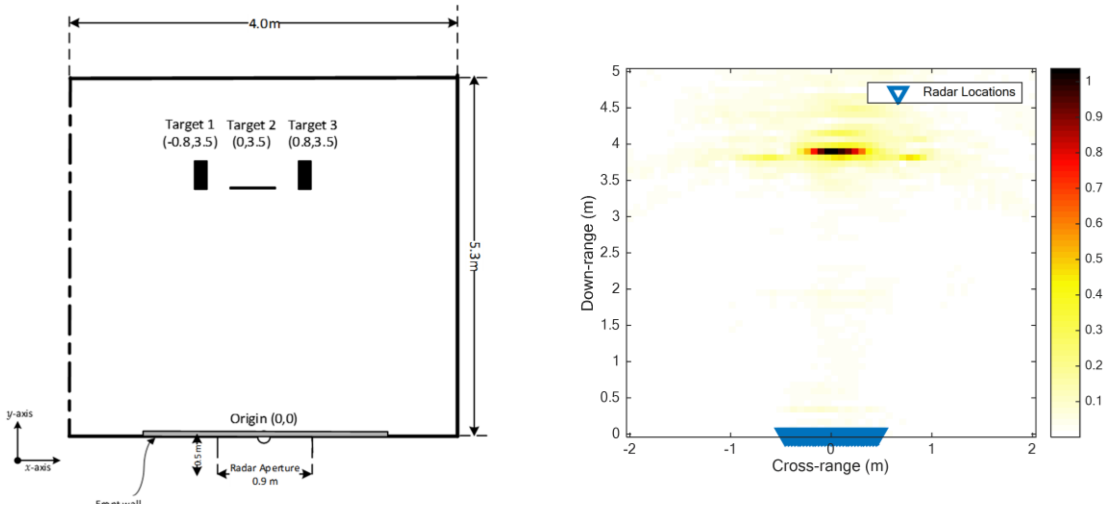

*Figure 6-8 (a) Sketch of the scene for experiment 2 (b) Radar image of Experiment 2*

*(a)* *(b)*

Figure 6-7 shows the radar image after applying delay and sum algorithm to the background-subtracted data. Using the system specifications in Table 6-1, and equations (6-3)-(6-4) , we can find the downrange and crossrange resolution of the radar. In Figure 6-7, we notice that Target 1 has a medium intensity, because its width is less than, but comparable to, the crossrange resolution. On the other hand, Target 3 has very low density due to the fact that its width and depth is much smaller than the crossrange and the downrange resolutions. The width and depth of Target 2, is larger than the downrange and the crossrange of the system, and hence its intensity it the highest. The width of Target 4, is larger than the crossrange resolution, but its depth is much less the downrange resolution, which caused its intensity to be medium.

Owing to the presence of the right and the back walls in the scene, the multipath reflections causes high-intensity pixels beside Target 2, they are call “ghost” as they confuse with the actual target.

### 6.5.2 Experiment 2: Cross range resolution

Three targets are used in this experiment where all targets are place at the same distance of 3.5 m from the front wall, as depicted in Figure 6-8 (a). The separation between the targets is 0.42 m. Target 1 and Target 3, are two computer cases faced toward the SAR system. The dimension of the front face is $0.18\text{m} \times 0.45\text{ m}$. Target 2, in between the two cases, is a metallic sheet of dimension of $0.47\text{m} \times 0.75\text{ m}$. The metallic sheet is above the ground by 0.3 m in front of a metallic chair

The objective of this experiment is to demonstrate the ability of the radar to distinguish between adjacent targets in the same down range. Since the targets are separated by distance that is less than the crossrange resolution, the radar has detected them as one target as shown in the radar image in Figure 6-8 (b).

Before moving to the next experiments, we would like to mention that, the SAR system was placed 0.5 m behind a gypsum wall of 1 cm thickness. The scene of the first two experiments, consists of multiple wooden desks and computers which are located beside the walls of the room as shown in Figure 6-6.

### 6.5.3 Experiments 3-4: The effects of Multipath and target-to-target interactions

In these experiments, we changed the environment to a class room with no furniture around the targets. The bandwidth of the system has increased to 9 GHz (1-10 GHz) and the number of frequency points has also increased to 1001. The radar systerem parameters for these two experiments 3-4 are changed as shown Table 6-2.

*Table 6-2 System Parameters for Experiments 3-4*

| | |
|---|---|
| **Type of signal** | Stepped frequency continuous wave |
| **Start frequency** | 1 GHz |
| **Stop frequency** | 10 GHz |
| **Number of frequencies** | 1001 |
| **Transmitted power** | 3 dBm |
| **Radar location** | $-\ \mathbf{0.6\ m}\ \boldsymbol{to}\ \mathbf{0.6\ m}$ |
| **Number of locations** | 41 |
| **Antenna type and Model** | Horn, A-INFOMW JXTXLB-10180 |
| **VNA model** | Agilent Fielfox N9918A |

We start with experiment 3, where we placed four metallic trash cans in the classroom as shown in Figure 6-9 (a). The sketch of the scene and the location of each target is depicted in Figure 6-9 (b). The resultant radar image is shown in Figure 6-10. The multipath effects are very clear in the middle of the image where three ghosts appear and marked by the start-shapes. The main sources for these ghosts are the multipath caucused by surrounding wall and the target-to-target interactions.

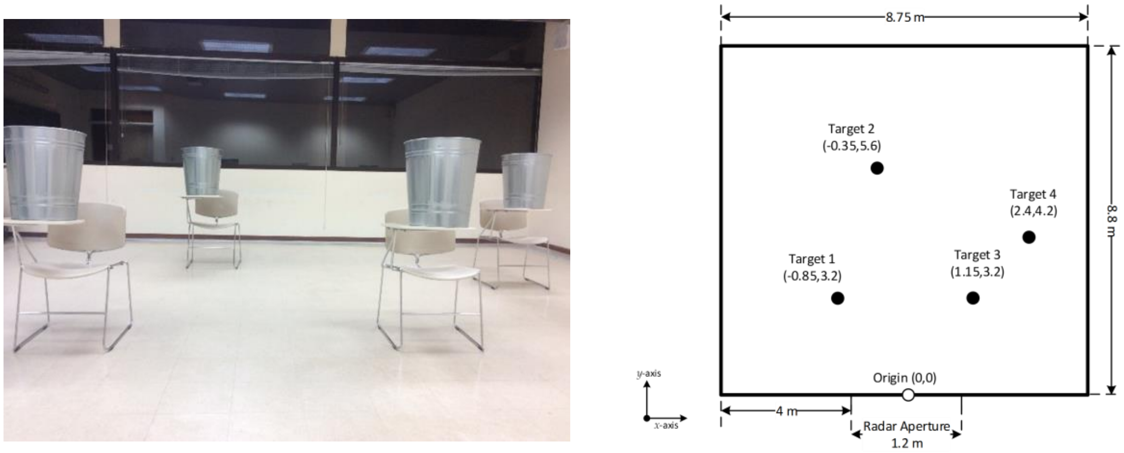

*Figure 6-9 (a) Populated scene of experiment 3 (b) Sketch of the scene for experiment 3*

(a) (b)

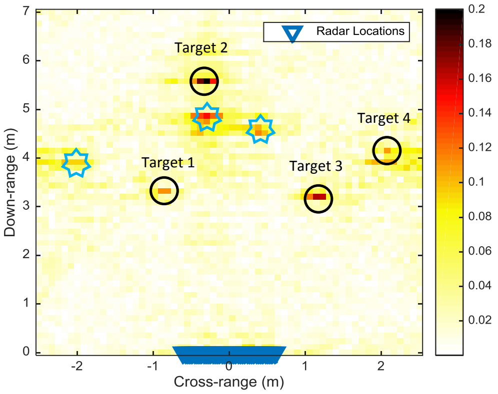

*Figure 6-10 Radar image of experiment 3*

In order to elaborate more on the multipath effects on the radar image, we repeat experiment 3 but with only three target as shown in Figure 6-11 (a). We removed Target 2 from the scene to remove its multipath effects. Figure 6-11 (b) shows the radar image as with three targets and one ghost.

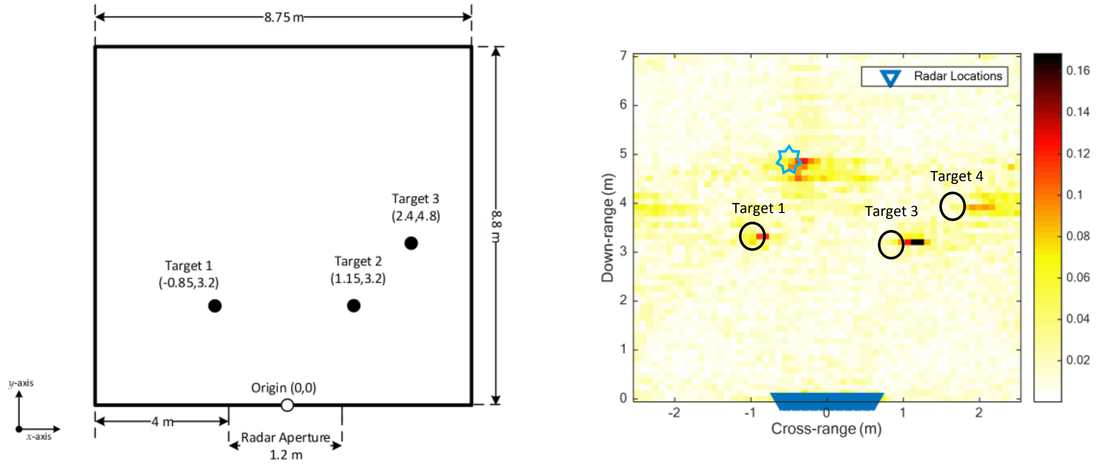

*Figure 6-11 (a) Sketch of the scene for experiment 4 (b) Radar image of Experiment 4*

## 6.6 Conclusion

This chapter has shown some of the by-products of this dissertation. A MTLAB-based simulator for TWRI was presented. Four experiments were conducted in real-life scenarios and based on high resolution UWB antenna and SAR. Several realistic-scenarios were implemented with different variation in the size and location of targets. The experiments were conducted in a populated lab and an empty classroom in order to show the effects of dense scatters environment and less scatters environment on the IRI. To provide more data-diversity, different radar parameters were used, such as bandwidth, number of frequencies, length of the aperture, and number of antennas locations. The crossrange resolution was examined, the minimum distance between two targets should be at least twice the crossrange to be distinguishable. Unless exploited, multipath, caused by the surrounding walls and by the target-to-target interaction, result in appearance of ghosts in the radar image. Further research is needed to enhance the ability of IRI in detect targets with low reflectivity in the presence of high-reflectivity targets. The acquired data is helpful for evaluating future advances in the field of indoor and through wall imaging. As extension of this work, several experiments for different wall materials and targets characteristics can be conducted. All data, figure, sketches will be made available for the research community of the subject matter.

Chapter 7

# Conclusions and Suggestions for Future Work

This chapter summarizes the main conclusions of this dissertation and suggests directions for future work.

## 7.1 Summary of Conclusions

This dissertation has contributed to the field of TWRI by proposing a new imaging mechanism; and a Bayesian-CS algorithm that overcomes some of encountered challenges in TWRI. In the following sections, we summarize and highlight the main findings.

### 7.1.1 Reducing the Mutual Coherence of the Sensing Matrix

This dissertation has proposed a technique for building a low mutual-coherence sensing matrix to be used in radar imaging applications. The proposed matrix improves the noise immunity of the system and enhances the reconstruction quality by 4-folds compared to the conventional CS-based techniques at $\mathrm{SNR} = 0\mathrm{dB}$. In addition, using the proposed matrix reduces the computational complexity of the CS-based estimation algorithms by factor of $U$, where $U$ is the number of grouped pixels in.

### 7.1.2 Proposing a Low Complexity Bayesian-Based Algorithm

A low complexity Bayesian-based algorithm has been proposed for the applications of TWRI. Unlike conventional CS-based algorithms, the complexity of the proposed algorithm does not vary with the bandwidth of the transmitted signal. This has granted the algorithm advantages such as producing high resolution images in short time compared to conventional algorithms.

The complexity reduction of the proposed algorithm was achieved by exploiting the structure of the bases-matrix in the TWRI problem. The complexity was reduced by a factor of $Q$, where $Q$ is the number of transmitted frequency.

The algorithm takes advantage of the sparsity of the scene and the Gaussianity of the additive noise. In contrast to other Bayesian-based algorithms, its performance does deteriorate by different probability distributions of the targets' reflectivity.

### 7.1.3 Leveraging the Antenna Correlation

This dissertation capitalizes on the correlation between the antenna elements in the SAR system. This has added further enhancement on the reconstruction quality. Leveraging antenna correlation is manifested by sharing three type of statistical information between the antenna elements. The first is the probability of the nonzero pixels; the second is the estimated nonzero pixels at each location; and the last is the expected location of the nonzero pixels. More than fifty percent enhancement in the image quality has been achieved at $\mathsf{SNR} = \mathsf{0dB}$, by sharing the probability of nonzero pixels.

Sharing information between antennas has also benefited the suppression of multipath effects caused by the surrounded walls in indoor TWRI.

### 7.1.4 TWRI Simulator and Practical Databank

- Over the course of developing the material of this dissertation, a TWRI MATLAB-based simulator was built. The simulator will be made available for the research community to generate TWRI data in different environment and in different room layouts. The simulator uses state of the art signal-models as in the literature of TWRI.

- Several experiments were conducted in real-life environments using UWB antenna. The generated raw data are organized and will be made available for the research community of TWRI.

## 7.2 Future Work

Although the results presented in this dissertation have demonstrated the effectiveness of the proposed Bayesian-based algorithm, many venues remain for extending the scope of this dissertation. This section discusses some of the topics that we consider for future extension.

- The analysis developed in the dissertation were built on the assumption that each target occupies a single pixel in the image; an extension can be made for extended targets. In this context, the algorithm can be modified for block sparsity reconstruction. Preliminary work was started as in [125].
- Our experiments were built and designed for 2D images. Further development is needed to extend the developed algorithm to reconstruct 3D images.
- Since the developed approach is a Bayesian-based, learning and adaptation mechanisms can be added. For example, by means of the distribution of the radar's return, the algorithm can sense the scene and adapt for the best bandwidth and aperture-length to be used.

- With the emerge of Machine Learning techniques, and using the Baeysian-framework, a statistical machine learning approach can be developed for object identification in TWRI.

# Appendix I: Derivation of Equation (4-16)

In this appendix, we provide the mathematical direvations of the regression in quation (4-16).

Using Woodbury matrix identity "Matrix inversion lemma" and LDU decomposition, we can derive the block matrix inversion as

$$\begin{bmatrix} A & U \\ V & C \end{bmatrix}^{-1} = \begin{bmatrix} A^{-1} + A^{-1}U(C - VA^{-1}U)^{-1}VA^{-1} & -A^{-1}U(C - VA^{-1}U)^{-1} \\ -(C - VA^{-1}U)^{-1}VA^{-1} & (C - VA^{-1}U)^{-1} \end{bmatrix} \qquad \text{(A-0-1)}$$

$A \rightarrow n \times n$ : $A$ Non-singular (Invertable)
$U \rightarrow n \times 1$
$C \rightarrow 1 \times 1$
$V \rightarrow 1 \times n$
let: $d = (1 - VA^{-1}U)^{-1}$

$$\begin{bmatrix} A & U \\ V & C \end{bmatrix}^{-1} = \begin{bmatrix} A^{-1} + \frac{1}{d}A^{-1}UVA^{-1} & -\frac{1}{d}A^{-1}U \\ -\frac{1}{d}VA^{-1} & \frac{1}{d} \end{bmatrix} \qquad \text{(A-0-2)}$$

From Equation (A-14) we have

$$\boldsymbol{\varepsilon}_{\mathcal{S}}(\mathbf{r}) = \left( \begin{bmatrix} \boldsymbol{\Psi}_{\underline{\mathcal{S}}}^{\mathrm{H}} \\ \boldsymbol{\psi}_{\mathscr{s}_i}^{\mathrm{H}} \end{bmatrix} \begin{bmatrix} \boldsymbol{\Psi}_{\underline{\mathcal{S}}} & \boldsymbol{\psi}_{\mathscr{s}_i} \end{bmatrix} \right)^{-1} \begin{bmatrix} \boldsymbol{\Psi}_{\underline{\mathcal{S}}}^{\mathrm{H}}\mathbf{r} \\ \boldsymbol{\psi}_{\mathscr{s}_i}^{\mathrm{H}}\,\mathbf{r} \end{bmatrix} \qquad \text{(A-0-3)}$$

Let:

$$\Lambda^{-1} = \left( \begin{bmatrix} \boldsymbol{\Psi}_{\underline{\mathcal{S}}}^{\mathrm{H}} \\ \boldsymbol{\psi}_{\mathscr{s}_i}^{\mathrm{H}} \end{bmatrix} \begin{bmatrix} \boldsymbol{\Psi}_{\underline{\mathcal{S}}}\ \boldsymbol{\psi}_{i} \end{bmatrix} \right)^{-1} = \begin{pmatrix} \left(\boldsymbol{\Psi}_{\underline{\mathcal{S}}}^{\mathrm{H}}\boldsymbol{\Psi}_{\underline{\mathcal{S}}}\right)_{|\underline{\mathcal{S}}|\times|\underline{\mathcal{S}}|} & \left(\boldsymbol{\Psi}_{\underline{\mathcal{S}}}^{\mathrm{H}}\boldsymbol{\psi}_{\mathscr{s}_i}\right)_{|\underline{\mathcal{S}}|\times 1} \\ \left(\boldsymbol{\psi}_{\mathscr{s}_i}^{\mathrm{H}}\,\boldsymbol{\Psi}_{\underline{\mathcal{S}}}\right)_{1\times|\underline{\mathcal{S}}|} & \left(\boldsymbol{\psi}_{\mathscr{s}_i}^{\mathrm{H}}\,\boldsymbol{\psi}_{\mathscr{s}_i}\right)_{1\times 1} \end{pmatrix}^{-1} \qquad \text{(A-0-4)}$$

$A = \boldsymbol{\Psi}_{\underline{\mathcal{S}}}^{\mathrm{H}}\boldsymbol{\Psi}_{\underline{\mathcal{S}}}$
$U = \boldsymbol{\Psi}_{\underline{\mathcal{S}}}^{\mathrm{H}}\boldsymbol{\psi}_{\mathscr{s}_i}$
$V = \boldsymbol{\psi}_{\mathscr{s}_i}^{\mathrm{H}}\,\boldsymbol{\Psi}_{\underline{\mathcal{S}}}$
$C = \boldsymbol{\psi}_{\mathscr{s}_i}^{\mathrm{H}}\,\boldsymbol{\psi}_{\mathscr{s}_i}$
$d_{\underline{\mathcal{S}}} = 1 - \boldsymbol{\psi}_{\mathscr{s}_i}^{\mathrm{H}}\,\boldsymbol{\Psi}_{\underline{\mathcal{S}}}\left(\boldsymbol{\Psi}_{\underline{\mathcal{S}}}^{\mathrm{H}}\boldsymbol{\Psi}_{\underline{\mathcal{S}}}\right)^{-1}\boldsymbol{\Psi}_{\underline{\mathcal{S}}}^{\mathrm{H}}\boldsymbol{\psi}_{\mathscr{s}_i}$

$\Rightarrow \boldsymbol{\Lambda}^{-1} =$

$$\begin{bmatrix} \left(\boldsymbol{\Psi}_{\underline{\mathcal{S}}}^{\mathrm{H}}\boldsymbol{\Psi}_{\underline{\mathcal{S}}}\right)^{-1} + \frac{1}{d_{\underline{\mathcal{S}}}}\left(\boldsymbol{\Psi}_{\underline{\mathcal{S}}}^{\mathrm{H}}\boldsymbol{\Psi}_{\underline{\mathcal{S}}}\right)^{-1}\boldsymbol{\Psi}_{\underline{\mathcal{S}}}^{\mathrm{H}}\boldsymbol{\psi}_{s_i}\,\boldsymbol{\psi}_{s_i}^{\mathrm{H}}\,\boldsymbol{\Psi}_{\underline{\mathcal{S}}}\left(\boldsymbol{\Psi}_{\underline{\mathcal{S}}}^{\mathrm{H}}\boldsymbol{\Psi}_{\underline{\mathcal{S}}}\right)^{-1} & -\frac{1}{d_{\underline{\mathcal{S}}}}\left(\boldsymbol{\Psi}_{\underline{\mathcal{S}}}^{\mathrm{H}}\boldsymbol{\Psi}_{\underline{\mathcal{S}}}\right)^{-1}\boldsymbol{\Psi}_{\underline{\mathcal{S}}}^{\mathrm{H}}\boldsymbol{\psi}_{s_i} \\ -\frac{1}{d_{\underline{\mathcal{S}}}}\boldsymbol{\psi}_{s_i}^{\mathrm{H}}\,\boldsymbol{\Psi}_{\underline{\mathcal{S}}}\left(\boldsymbol{\Psi}_{\underline{\mathcal{S}}}^{\mathrm{H}}\boldsymbol{\Psi}_{\underline{\mathcal{S}}}\right)^{-1} & \frac{1}{d_{\underline{\mathcal{S}}}} \end{bmatrix}$$

Then we multiply with the vector $\begin{bmatrix} \boldsymbol{\Psi}_{\underline{\mathcal{S}}}^{\mathrm{H}}\mathbf{r} \\ \boldsymbol{\psi}_{s_i}^{\mathrm{H}}\,\mathbf{r} \end{bmatrix}$

$$\boldsymbol{\chi}_{\mathcal{S}}(\mathbf{r}) = \boldsymbol{\Lambda}^{-1}\begin{bmatrix} \boldsymbol{\Psi}_{\underline{\mathcal{S}}}^{\mathrm{H}}\mathbf{r} \\ \boldsymbol{\psi}_{s_i}^{\mathrm{H}}\,\mathbf{r} \end{bmatrix}$$

$$= \begin{bmatrix} \left(\boldsymbol{\Psi}_{\underline{\mathcal{S}}}^{\mathrm{H}}\boldsymbol{\Psi}_{\underline{\mathcal{S}}}\right)^{-1} + \frac{1}{d_{\underline{\mathcal{S}}}}\left(\boldsymbol{\Psi}_{\underline{\mathcal{S}}}^{\mathrm{H}}\boldsymbol{\Psi}_{\underline{\mathcal{S}}}\right)^{-1}\boldsymbol{\Psi}_{\underline{\mathcal{S}}}^{\mathrm{H}}\boldsymbol{\psi}_{s_i}\,\boldsymbol{\psi}_{s_i}^{\mathrm{H}}\,\boldsymbol{\Psi}_{\underline{\mathcal{S}}}\left(\boldsymbol{\Psi}_{\underline{\mathcal{S}}}^{\mathrm{H}}\boldsymbol{\Psi}_{\underline{\mathcal{S}}}\right)^{-1} & -\frac{1}{d_{\underline{\mathcal{S}}}}\left(\boldsymbol{\Psi}_{\underline{\mathcal{S}}}^{\mathrm{H}}\boldsymbol{\Psi}_{\underline{\mathcal{S}}}\right)^{-1}\boldsymbol{\Psi}_{\underline{\mathcal{S}}}^{\mathrm{H}}\boldsymbol{\psi}_{s_i} \\ -\frac{1}{d_{\underline{\mathcal{S}}}}\boldsymbol{\psi}_{s_i}^{\mathrm{H}}\,\boldsymbol{\Psi}_{\underline{\mathcal{S}}}\left(\boldsymbol{\Psi}_{\underline{\mathcal{S}}}^{\mathrm{H}}\boldsymbol{\Psi}_{\underline{\mathcal{S}}}\right)^{-1} & \frac{1}{d_{\underline{\mathcal{S}}}} \end{bmatrix}\begin{bmatrix} \boldsymbol{\Psi}_{\underline{\mathcal{S}}}^{\mathrm{H}}\mathbf{r} \\ \boldsymbol{\psi}_{s_i}^{\mathrm{H}}\,\mathbf{r} \end{bmatrix}$$

$$= \begin{bmatrix} \left[\left(\boldsymbol{\Psi}_{\underline{\mathcal{S}}}^{\mathrm{H}}\boldsymbol{\Psi}_{\underline{\mathcal{S}}}\right)^{-1} + \frac{1}{d_{\underline{\mathcal{S}}}}\left(\boldsymbol{\Psi}_{\underline{\mathcal{S}}}^{\mathrm{H}}\boldsymbol{\Psi}_{\underline{\mathcal{S}}}\right)^{-1}\boldsymbol{\Psi}_{\underline{\mathcal{S}}}^{\mathrm{H}}\boldsymbol{\psi}_{s_i}\,\boldsymbol{\psi}_{s_i}^{\mathrm{H}}\,\boldsymbol{\Psi}_{\underline{\mathcal{S}}}\left(\boldsymbol{\Psi}_{\underline{\mathcal{S}}}^{\mathrm{H}}\boldsymbol{\Psi}_{\underline{\mathcal{S}}}\right)^{-1}\right]\boldsymbol{\Psi}_{\underline{\mathcal{S}}}^{\mathrm{H}}\mathbf{r} - \frac{1}{d_{\underline{\mathcal{S}}}}\left(\boldsymbol{\Psi}_{\underline{\mathcal{S}}}^{\mathrm{H}}\boldsymbol{\Psi}_{\underline{\mathcal{S}}}\right)^{-1}\boldsymbol{\Psi}_{\underline{\mathcal{S}}}^{\mathrm{H}}\boldsymbol{\psi}_{s_i}\,\boldsymbol{\psi}_{s_i}^{\mathrm{H}}\,\mathbf{r} \\ -\frac{1}{d_{\underline{\mathcal{S}}}}\boldsymbol{\psi}_{s_i}^{\mathrm{H}}\,\boldsymbol{\Psi}_{\underline{\mathcal{S}}}\left(\boldsymbol{\Psi}_{\underline{\mathcal{S}}}^{\mathrm{H}}\boldsymbol{\Psi}_{\underline{\mathcal{S}}}\right)^{-1}\boldsymbol{\Psi}_{\underline{\mathcal{S}}}^{\mathrm{H}}\mathbf{r} + \frac{1}{d_{\underline{\mathcal{S}}}}\boldsymbol{\psi}_{s_i}^{\mathrm{H}}\,\mathbf{r} \end{bmatrix} \tag{A-0-5}$$

$$= \begin{bmatrix} \left(\boldsymbol{\Psi}_{\underline{\mathcal{S}}}^{\mathrm{H}}\boldsymbol{\Psi}_{\underline{\mathcal{S}}}\right)^{-1}\boldsymbol{\Psi}_{\underline{\mathcal{S}}}^{\mathrm{H}}\mathbf{r} + \frac{1}{d_{\underline{\mathcal{S}}}}\left(\boldsymbol{\Psi}_{\underline{\mathcal{S}}}^{\mathrm{H}}\boldsymbol{\Psi}_{\underline{\mathcal{S}}}\right)^{-1}\boldsymbol{\Psi}_{\underline{\mathcal{S}}}^{\mathrm{H}}\boldsymbol{\psi}_{s_i}\,\boldsymbol{\psi}_{s_i}^{\mathrm{H}}\,\boldsymbol{\Psi}_{\underline{\mathcal{S}}}\left(\boldsymbol{\Psi}_{\underline{\mathcal{S}}}^{\mathrm{H}}\boldsymbol{\Psi}_{\underline{\mathcal{S}}}\right)^{-1}\boldsymbol{\Psi}_{\underline{\mathcal{S}}}^{\mathrm{H}}\mathbf{r} - \frac{1}{d_{\underline{\mathcal{S}}}}\left(\boldsymbol{\Psi}_{\underline{\mathcal{S}}}^{\mathrm{H}}\boldsymbol{\Psi}_{\underline{\mathcal{S}}}\right)^{-1}\boldsymbol{\Psi}_{\underline{\mathcal{S}}}^{\mathrm{H}}\boldsymbol{\psi}_{s_i}\,\boldsymbol{\psi}_{s_i}^{\mathrm{H}}\,\mathbf{r} \\ -\frac{1}{d_{\underline{\mathcal{S}}}}\boldsymbol{\psi}_{s_i}^{\mathrm{H}}\,\boldsymbol{\Psi}_{\underline{\mathcal{S}}}\left(\boldsymbol{\Psi}_{\underline{\mathcal{S}}}^{\mathrm{H}}\boldsymbol{\Psi}_{\underline{\mathcal{S}}}\right)^{-1}\boldsymbol{\Psi}_{\underline{\mathcal{S}}}^{\mathrm{H}}\mathbf{r} + \frac{1}{d_{\underline{\mathcal{S}}}}\boldsymbol{\psi}_{s_i}^{\mathrm{H}}\,\mathbf{r} \end{bmatrix} \tag{A-0-6}$$

$$= \begin{bmatrix} \left(\boldsymbol{\Psi}_{\underline{\mathcal{S}}}^{\mathrm{H}}\boldsymbol{\Psi}_{\underline{\mathcal{S}}}\right)^{-1}\boldsymbol{\Psi}_{\underline{\mathcal{S}}}^{\mathrm{H}}\mathbf{r} + \frac{1}{d_{\underline{\mathcal{S}}}}\left(\boldsymbol{\Psi}_{\underline{\mathcal{S}}}^{\mathrm{H}}\boldsymbol{\Psi}_{\underline{\mathcal{S}}}\right)^{-1}\boldsymbol{\Psi}_{\underline{\mathcal{S}}}^{\mathrm{H}}\boldsymbol{\psi}_{s_i}\,\boldsymbol{\psi}_{s_i}^{\mathrm{H}}\,\boldsymbol{\Psi}_{\underline{\mathcal{S}}}\left(\boldsymbol{\Psi}_{\underline{\mathcal{S}}}^{\mathrm{H}}\boldsymbol{\Psi}_{\underline{\mathcal{S}}}\right)^{-1}\boldsymbol{\Psi}_{\underline{\mathcal{S}}}^{\mathrm{H}}\mathbf{r} - \frac{1}{d_{\underline{\mathcal{S}}}}\left(\boldsymbol{\Psi}_{\underline{\mathcal{S}}}^{\mathrm{H}}\boldsymbol{\Psi}_{\underline{\mathcal{S}}}\right)^{-1}\boldsymbol{\Psi}_{\underline{\mathcal{S}}}^{\mathrm{H}}\boldsymbol{\psi}_{s_i}\,\boldsymbol{\psi}_{s_i}^{\mathrm{H}}\,\mathbf{r} \\ -\frac{1}{d_{\underline{\mathcal{S}}}}\left[\boldsymbol{\psi}_{s_i}^{\mathrm{H}}\,\boldsymbol{\Psi}_{\underline{\mathcal{S}}}\left(\boldsymbol{\Psi}_{\underline{\mathcal{S}}}^{\mathrm{H}}\boldsymbol{\Psi}_{\underline{\mathcal{S}}}\right)^{-1}\boldsymbol{\Psi}_{\underline{\mathcal{S}}}^{\mathrm{H}}\mathbf{r} - \boldsymbol{\psi}_{s_i}^{\mathrm{H}}\,\mathbf{r}\right] \end{bmatrix} \tag{A-0-7}$$

$$= \begin{bmatrix} \boldsymbol{\varepsilon}_{\underline{\mathcal{S}}}(\mathbf{r}) + \frac{1}{d_{\underline{\mathcal{S}}}}\boldsymbol{\varepsilon}_{\underline{\mathcal{S}}}\left(\boldsymbol{\psi}_{s_i}\right)\boldsymbol{\rho}_{s_i}\left(\boldsymbol{\Psi}_{\underline{\mathcal{S}}}\right)\boldsymbol{\varepsilon}_{\underline{\mathcal{S}}}(\mathbf{r}) - \frac{1}{d_{\underline{\mathcal{S}}}}\boldsymbol{\varepsilon}_{\underline{\mathcal{S}}}\left(\boldsymbol{\psi}_{s_i}\right)\rho_{s_i}(\mathbf{r}) \\ -\frac{1}{d_{\underline{\mathcal{S}}}}\left[\boldsymbol{\rho}_{s_i}\left(\boldsymbol{\Psi}_{\underline{\mathcal{S}}}\right)\boldsymbol{\varepsilon}_{\underline{\mathcal{S}}}(\mathbf{r}) - \rho_{s_i}(\mathbf{r})\right] \end{bmatrix}$$

$$\therefore\ \boldsymbol{\varepsilon}_{\mathcal{S}}(\mathbf{r}) = \begin{bmatrix} \boldsymbol{\varepsilon}_{\underline{\mathcal{S}}}(\mathbf{r}) + \frac{1}{d_{\underline{\mathcal{S}}}}\boldsymbol{\varepsilon}_{\underline{\mathcal{S}}}\left(\boldsymbol{\psi}_{s_i}\right)\left[\boldsymbol{\rho}_{s_i}\left(\boldsymbol{\Psi}_{\underline{\mathcal{S}}}\right)\boldsymbol{\varepsilon}_{\underline{\mathcal{S}}}(\mathbf{r}) - \rho_{s_i}(\mathbf{r})\right] \\ -\frac{1}{d_{\underline{\mathcal{S}}}}\left[\boldsymbol{\rho}_{s_i}\left(\boldsymbol{\Psi}_{\underline{\mathcal{S}}}\right)\boldsymbol{\varepsilon}_{\underline{\mathcal{S}}}(\mathbf{r}) - \rho_{s_i}(\mathbf{r})\right] \end{bmatrix} \tag{A-0-8}$$

$$\boldsymbol{\varepsilon}_{\underline{\mathcal{S}}}(\mathbf{r}) = \left(\boldsymbol{\Psi}_{\underline{\mathcal{S}}}^{\mathrm{H}}\boldsymbol{\Psi}_{\underline{\mathcal{S}}}\right)^{-1}\boldsymbol{\Psi}_{\underline{\mathcal{S}}}^{\mathrm{H}}\mathbf{r} \tag{A-0-9}$$

$$\boldsymbol{\varepsilon}_{\underline{\mathcal{S}}}\left(\boldsymbol{\psi}_{s_i}\right) = \left(\boldsymbol{\Psi}_{\underline{\mathcal{S}}}^{\mathrm{H}}\boldsymbol{\Psi}_{\underline{\mathcal{S}}}\right)^{-1}\boldsymbol{\Psi}_{\underline{\mathcal{S}}}^{\mathrm{H}}\boldsymbol{\psi}_{s_i} \tag{A-0-10}$$

$$\boldsymbol{\rho}_{s_i}\left(\boldsymbol{\Psi}_{\underline{\mathcal{S}}}\right) = \boldsymbol{\psi}_{s_i}^{\mathrm{H}}\,\boldsymbol{\Psi}_{\underline{\mathcal{S}}} \tag{A-0-11}$$

$$\rho_{s_i}(\mathbf{r}) = \boldsymbol{\psi}_{s_i}^{\mathrm{H}}\,\mathbf{r} \tag{A-0-12}$$

# Appendix II: Derivation of Equation (4-21)

In this appendix, we provide the mathematical direvations of the regression in quation (4-21)

$$\boldsymbol{\varepsilon}_{\mathcal{S}}\left(\boldsymbol{\psi}_{s_{i+1}}\right) = \left(\boldsymbol{\Psi}_{\mathcal{S}}^{\mathrm{H}}\boldsymbol{\Psi}_{\mathcal{S}}\right)^{-1}\boldsymbol{\Psi}_{\mathcal{S}}^{\mathrm{H}}\boldsymbol{\psi}_{s_{i+1}}$$

$$= \left(\begin{bmatrix} \boldsymbol{\Psi}_{\underline{\mathcal{S}}}^{\mathrm{H}} \\ \boldsymbol{\psi}_{s_i}^{\mathrm{H}} \end{bmatrix} \begin{bmatrix} \boldsymbol{\Psi}_{\underline{\mathcal{S}}} & \boldsymbol{\psi}_{s_i} \end{bmatrix}\right)^{-1} \begin{bmatrix} \boldsymbol{\Psi}_{\underline{\mathcal{S}}}^{\mathrm{H}}\boldsymbol{\psi}_{s_{i+1}} \\ \boldsymbol{\psi}_{s_i}^{\mathrm{H}}\,\boldsymbol{\psi}_{s_{i+1}} \end{bmatrix} \tag{A-0-1}$$

Let: block matrix inversion in (A-0-2)

$$\mathbf{K}^{-1} = \begin{pmatrix} \left(\boldsymbol{\Psi}_{\underline{\mathcal{S}}}^{\mathrm{H}}\boldsymbol{\Psi}_{\underline{\mathcal{S}}}\right)_{|\underline{\mathcal{S}}|\times|\underline{\mathcal{S}}|} & \left(\boldsymbol{\Psi}_{\underline{\mathcal{S}}}^{\mathrm{H}}\boldsymbol{\psi}_{s_i}\right)_{|\underline{\mathcal{S}}|\times 1} \\ \left(\boldsymbol{\psi}_{s_i}^{\mathrm{H}}\,\boldsymbol{\Psi}_{\underline{\mathcal{S}}}\right)_{1\times|\underline{\mathcal{S}}|} & \left(\boldsymbol{\psi}_{s_i}^{\mathrm{H}}\,\boldsymbol{\psi}_{s_i}\right)_{1\times 1} \end{pmatrix}^{-1} \tag{A-0-2}$$

$\Rightarrow \mathbf{K}^{-1}$

$$= \begin{bmatrix} \left(\boldsymbol{\Psi}_{\underline{\mathcal{S}}}^{\mathrm{H}}\boldsymbol{\Psi}_{\underline{\mathcal{S}}}\right)^{-1} + \frac{1}{d_{\underline{\mathcal{S}}}}\left(\boldsymbol{\Psi}_{\underline{\mathcal{S}}}^{\mathrm{H}}\boldsymbol{\Psi}_{\underline{\mathcal{S}}}\right)^{-1}\boldsymbol{\Psi}_{\underline{\mathcal{S}}}^{\mathrm{H}}\boldsymbol{\psi}_{s_i}\,\boldsymbol{\psi}_{s_i}^{\mathrm{H}}\,\boldsymbol{\Psi}_{\underline{\mathcal{S}}}\left(\boldsymbol{\Psi}_{\underline{\mathcal{S}}}^{\mathrm{H}}\boldsymbol{\Psi}_{\underline{\mathcal{S}}}\right)^{-1} & -\frac{1}{d_{\underline{\mathcal{S}}}}\left(\boldsymbol{\Psi}_{\underline{\mathcal{S}}}^{\mathrm{H}}\boldsymbol{\Psi}_{\underline{\mathcal{S}}}\right)^{-1}\boldsymbol{\Psi}_{\underline{\mathcal{S}}}^{\mathrm{H}}\boldsymbol{\psi}_{s_i} \\ -\frac{1}{d_{\underline{\mathcal{S}}}}\boldsymbol{\psi}_{s_i}^{\mathrm{H}}\,\boldsymbol{\Psi}_{\underline{\mathcal{S}}}\left(\boldsymbol{\Psi}_{\underline{\mathcal{S}}}^{\mathrm{H}}\boldsymbol{\Psi}_{\underline{\mathcal{S}}}\right)^{-1} & \frac{1}{d_{\underline{\mathcal{S}}}} \end{bmatrix} \tag{A-0-3}$$

where $d_{\underline{\underline{\mathcal{S}}}} = 1 - \boldsymbol{\psi}_{s_i}^{\mathrm{H}}\,\boldsymbol{\Psi}_{\underline{\mathcal{S}}}\left(\boldsymbol{\Psi}_{\underline{\mathcal{S}}}^{\mathrm{H}}\boldsymbol{\Psi}_{\underline{\mathcal{S}}}\right)^{-1}\boldsymbol{\Psi}_{\underline{\mathcal{S}}}^{\mathrm{H}}\boldsymbol{\psi}_{s_i}$

Now we substiture $\mathbf{K}^{-1}$ in (A-0-1)

$$\boldsymbol{\varepsilon}_{\mathcal{S}}\left(\boldsymbol{\psi}_{s_{i+1}}\right) = \mathrm{K}^{-1}\begin{bmatrix} \boldsymbol{\Psi}_{\underline{\mathcal{S}}}^{\mathrm{H}}\boldsymbol{\psi}_{s_{i+1}} \\ \boldsymbol{\psi}_{s_i}^{\mathrm{H}}\,\boldsymbol{\psi}_{s_{i+1}} \end{bmatrix}$$

$$= \begin{bmatrix} \left[\left(\boldsymbol{\Psi}_{\underline{\mathcal{S}}}^{\mathrm{H}}\boldsymbol{\Psi}_{\underline{\mathcal{S}}}\right)^{-1} + \frac{1}{d_{\underline{\mathcal{S}}}}\left(\boldsymbol{\Psi}_{\underline{\mathcal{S}}}^{\mathrm{H}}\boldsymbol{\Psi}_{\underline{\mathcal{S}}}\right)^{-1}\boldsymbol{\Psi}_{\underline{\mathcal{S}}}^{\mathrm{H}}\boldsymbol{\psi}_{s_i}\,\boldsymbol{\psi}_{s_i}^{\mathrm{H}}\,\boldsymbol{\Psi}_{\underline{\mathcal{S}}}\left(\boldsymbol{\Psi}_{\underline{\mathcal{S}}}^{\mathrm{H}}\boldsymbol{\Psi}_{\underline{\mathcal{S}}}\right)^{-1}\right]\boldsymbol{\Psi}_{\underline{\mathcal{S}}}^{\mathrm{H}}\boldsymbol{\psi}_{s_{i+1}} - \frac{1}{d_{\underline{\mathcal{S}}}}\left(\boldsymbol{\Psi}_{\underline{\mathcal{S}}}^{\mathrm{H}}\boldsymbol{\Psi}_{\underline{\mathcal{S}}}\right)^{-1}\boldsymbol{\Psi}_{\underline{\mathcal{S}}}^{\mathrm{H}}\boldsymbol{\psi}_{s_i}\,\boldsymbol{\psi}_{s_i}^{\mathrm{H}}\,\boldsymbol{\psi}_{s_{i+1}} \\ -\frac{1}{d_{\underline{\mathcal{S}}}}\boldsymbol{\psi}_{s_i}^{\mathrm{H}}\,\boldsymbol{\Psi}_{\underline{\mathcal{S}}}\left(\boldsymbol{\Psi}_{\underline{\mathcal{S}}}^{\mathrm{H}}\boldsymbol{\Psi}_{\underline{\mathcal{S}}}\right)^{-1}\boldsymbol{\Psi}_{\underline{\mathcal{S}}}^{\mathrm{H}}\boldsymbol{\psi}_{s_{i+1}} + \frac{1}{d_{\underline{\mathcal{S}}}}\boldsymbol{\psi}_{s_i}^{\mathrm{H}}\,\boldsymbol{\psi}_{s_{i+1}} \end{bmatrix} \tag{A-0-4}$$

$$= \begin{bmatrix} \left(\boldsymbol{\Psi}_{\underline{\mathcal{S}}}^{\mathrm{H}}\boldsymbol{\Psi}_{\underline{\mathcal{S}}}\right)^{-1}\boldsymbol{\Psi}_{\underline{\mathcal{S}}}^{\mathrm{H}}\boldsymbol{\psi}_{s_{i+1}} + \frac{1}{d_{\underline{\mathcal{S}}}}\left(\boldsymbol{\Psi}_{\underline{\mathcal{S}}}^{\mathrm{H}}\boldsymbol{\Psi}_{\underline{\mathcal{S}}}\right)^{-1}\boldsymbol{\Psi}_{\underline{\mathcal{S}}}^{\mathrm{H}}\boldsymbol{\psi}_{s_i}\,\boldsymbol{\psi}_{s_i}^{\mathrm{H}}\,\boldsymbol{\Psi}_{\underline{\mathcal{S}}}\left(\boldsymbol{\Psi}_{\underline{\mathcal{S}}}^{\mathrm{H}}\boldsymbol{\Psi}_{\underline{\mathcal{S}}}\right)^{-1}\boldsymbol{\Psi}_{\underline{\mathcal{S}}}^{\mathrm{H}}\boldsymbol{\psi}_{s_{i+1}} - \frac{1}{d_{\underline{\mathcal{S}}}}\left(\boldsymbol{\Psi}_{\underline{\mathcal{S}}}^{\mathrm{H}}\boldsymbol{\Psi}_{\underline{\mathcal{S}}}\right)^{-1}\boldsymbol{\Psi}_{\underline{\mathcal{S}}}^{\mathrm{H}}\boldsymbol{\psi}_{s_i}\,\boldsymbol{\psi}_{s_i}^{\mathrm{H}}\,\boldsymbol{\psi}_{s_{i+1}} \\ -\frac{1}{d_{\underline{\mathcal{S}}}}\left[\boldsymbol{\psi}_{s_i}^{\mathrm{H}}\,\boldsymbol{\Psi}_{\underline{\mathcal{S}}}\left(\boldsymbol{\Psi}_{\underline{\mathcal{S}}}^{\mathrm{H}}\boldsymbol{\Psi}_{\underline{\mathcal{S}}}\right)^{-1}\boldsymbol{\Psi}_{\underline{\mathcal{S}}}^{\mathrm{H}}\boldsymbol{\psi}_{s_{i+1}} - \boldsymbol{\psi}_{s_i}^{\mathrm{H}}\,\boldsymbol{\psi}_{s_{i+1}}\right] \end{bmatrix} \tag{A-0-5}$$

$$= \begin{bmatrix} \boldsymbol{\varepsilon}_{\underline{\mathcal{S}}}\left(\boldsymbol{\psi}_{s_{i+1}}\right) + \frac{1}{d_{\underline{\mathcal{S}}}}\boldsymbol{\varepsilon}_{\underline{\mathcal{S}}}\left(\boldsymbol{\psi}_{s_i}\right)\boldsymbol{\rho}_{s_i}\left(\boldsymbol{\Psi}_{\underline{\mathcal{S}}}\right)\boldsymbol{\varepsilon}_{\underline{\mathcal{S}}}\left(\boldsymbol{\psi}_{s_{i+1}}\right) - \frac{1}{d_{\underline{\mathcal{S}}}}\boldsymbol{\varepsilon}_{\underline{\mathcal{S}}}\left(\boldsymbol{\psi}_{s_i}\right)\rho_{s_i}\left(\boldsymbol{\psi}_{s_{i+1}}\right) \\ -\frac{1}{d_{\underline{\mathcal{S}}}}\left[\boldsymbol{\rho}_{s_i}\left(\boldsymbol{\Psi}_{\underline{\mathcal{S}}}\right)\boldsymbol{\varepsilon}_{\underline{\mathcal{S}}}\left(\boldsymbol{\psi}_{s_{i+1}}\right) - \rho_{s_i}\left(\boldsymbol{\psi}_{s_{i+1}}\right)\right] \end{bmatrix}$$

$$\therefore \quad \boldsymbol{\varepsilon}_{\mathcal{S}}\left(\boldsymbol{\psi}_{\mathscr{s}_{i+1}}\right) = \begin{bmatrix} \boldsymbol{\varepsilon}_{\underline{\mathcal{S}}}\left(\boldsymbol{\psi}_{\mathscr{s}_{i+1}}\right) + \dfrac{1}{d_{\underline{\mathcal{S}}}} \boldsymbol{\varepsilon}_{\underline{\mathcal{S}}}\left(\boldsymbol{\psi}_{\mathscr{s}_i}\right) \left[\boldsymbol{\rho}_{\mathscr{s}_i}\left(\boldsymbol{\Psi}_{\underline{\mathcal{S}}}\right) \boldsymbol{\varepsilon}_{\underline{\mathcal{S}}}\left(\boldsymbol{\psi}_{\mathscr{s}_{i+1}}\right) - \rho_{\mathscr{s}_i}\left(\boldsymbol{\psi}_{\mathscr{s}_{i+1}}\right)\right] \\ - \dfrac{1}{d_{\underline{\mathcal{S}}}} \left[\boldsymbol{\rho}_{\mathscr{s}_i}\left(\boldsymbol{\Psi}_{\underline{\mathcal{S}}}\right) \boldsymbol{\varepsilon}_{\underline{\mathcal{S}}}\left(\boldsymbol{\psi}_{\mathscr{s}_{i+1}}\right) - \rho_{\mathscr{s}_i}\left(\boldsymbol{\psi}_{\mathscr{s}_{i+1}}\right)\right] \end{bmatrix} \tag{A-0-6}$$

$$\boldsymbol{\varepsilon}_{\underline{\mathcal{S}}}\left(\boldsymbol{\psi}_{\mathscr{s}_{i+1}}\right) = \left(\boldsymbol{\Psi}_{\underline{\mathcal{S}}}^{\mathrm{H}} \boldsymbol{\Psi}_{\underline{\mathcal{S}}}\right)^{-1} \boldsymbol{\Psi}_{\underline{\mathcal{S}}}^{\mathrm{H}} \boldsymbol{\psi}_{\mathscr{s}_{i+1}} \tag{A-0-7}$$

$$\boldsymbol{\varepsilon}_{\underline{\mathcal{S}}}\left(\boldsymbol{\psi}_{\mathscr{s}_i}\right) = \left(\boldsymbol{\Psi}_{\underline{\mathcal{S}}}^{\mathrm{H}} \boldsymbol{\Psi}_{\underline{\mathcal{S}}}\right)^{-1} \boldsymbol{\Psi}_{\underline{\mathcal{S}}}^{\mathrm{H}} \boldsymbol{\psi}_{\mathscr{s}_i} \tag{A-0-8}$$

$$\boldsymbol{\rho}_{\mathscr{s}_i}\left(\boldsymbol{\Psi}_{\underline{\mathcal{S}}}\right) = \boldsymbol{\psi}_{\mathscr{s}_i}^{\mathrm{H}} \boldsymbol{\Psi}_{\underline{\mathcal{S}}} \tag{A-0-9}$$

$$\rho_{\mathscr{s}_i}\left(\boldsymbol{\psi}_{\mathscr{s}_{i+1}}\right) = \boldsymbol{\psi}_{\mathscr{s}_i}^{\mathrm{H}} \boldsymbol{\psi}_{\mathscr{s}_{i+1}} \tag{A-0-10}$$

# Bibliography

1 Leigsnering, M., Ahmad, F., Amin, M., Zoubir, A.: 'Multipath exploitation in through-the-wall radar imaging using sparse reconstruction'*IEEE Trans. Aerosp. Electron. Syst.*, 2014, **50**, (2), pp. 920–939.

2 Setlur, P., Alli, G., Nuzzo, L.: 'Multipath exploitation in through-wall radar imaging via point spread functions'*IEEE Trans. Image Process.*, 2013, **22**, (12).

3 B., Chakraborty, Y. Li, J.Z., Chakraborty, B., Li, Y., *et al.*: 'Multipath exploitation with adaptive waveform design for tracking in urban terrain', in 'ICASSP, IEEE International Conference on Acoustics, Speech and Signal Processing - Proceedings' (2010), pp. 3894–3897

4 Li, Z., Lingjiang, K., Yong, J., Zhongxing, Z., Lan, F.: 'A novel approach of multi-path suppression based on sub-aperture imaging in through-wall-radar imaging', in 'IEEE Radar Conference (RADAR)' (2013), pp. 4–7

5 Krolik, J.L., Farrell, J., Steinhardt, A., Drive, N.F.: 'Exploiting multipath propagation for GMTI in urban environments', in 'IEEE Conference on Radar' (2006), pp. 65–68

6 Abdalla, A.T., Muqaibel, A.H., Al-Dharrab, S.: ‘Aspect dependent multipath ghost suppression in TWRI under compressive sensing framework’*2015 Int. Conf. Commun. Signal Process. Their Appl. ICCSPA 2015*, 2015.

7 Leigsnering, M., Ahmad, F., Amin, M.G., Zoubir, A.M.: ‘Compressive Sensing-Based Multipath Exploitation for Stationary and Moving Indoor Target Localization’*IEEE J. Sel. Top. Signal Process.*, 2015, **9**, (8), pp. 1469–1483.

8 Yoon, Y.-S., Amin, M.G.: ‘Compressed sensing technique for high-resolution radar imaging’*Proc. SPIE*, 2008, **6968**, p. 69681A–69681A–10.

9 Yoon, Y.S., Amin, M.G.: ‘Imaging of behind the wall targets using wideband beamforming with compressive sensing’*IEEE Work. Stat. Signal Process. Proc.*, 2009, pp. 93–96.

10 Huang, Q., Qu, L., Wu, B., Fang, G.: ‘UWB through-wall imaging based on compressive sensing’*IEEE Trans. Geosci. Remote Sens.*, 2010, **48**, (3 PART2), pp. 1408–1415.

11 Tivive, F.H.C., Bouzerdoum, A.: ‘A compressed sensing method for complex-valued signals with application to through-the-wall radar imaging’*ICASSP, IEEE Int. Conf. Acoust. Speech Signal Process. - Proc.*, 2013, (2), pp. 2144–

2148.

12 Wu, Q., Zhang, Y.D., Amin, M.G., Himed, B.: ‘Multi-task bayesian compressive sensing exploiting intra-task dependency’*IEEE Signal Process. Lett.*, 2015, **22**, (4), pp. 430–434.

13 Wu, Q., Zhang, Y.D., Ahmad, F., Amin, M.G.: ‘Compressive-sensing-based high-resolution polarimetric through-the-wall radar imaging exploiting target characteristics’*IEEE Antennas Wirel. Propag. Lett.*, 2015, **14**, (c), pp. 1043–1047.

14 Yoon, Y.S., Amin, M.G.: ‘Through-the-Wall Radar Imaging using compressive sensing along temporal frequency domain’*2010 IEEE Int. Conf. Acoust. Speech Signal Process.*, 2010, pp. 2806–2809.

15 Leigsnering, M., Amin, M., Ahmad, F., Zoubir, A.M.: ‘Multipath exploitation and suppression for SAR imaging of building interiors: An overview of recent advances’*IEEE Signal Process. Mag.*, 2014, **31**, (4), pp. 110–119.

16 Ahmad, F., Amin, M.G.: ‘Through-the-wall human motion indication using sparsity-driven change detection’*IEEE Trans. Geosci. Remote Sens.*, 2013, **51**, (2), pp. 881–890.

17 Gurbuz, A.C., McClellan, J.H., Scott, W.R.: ‘A compressive sensing data acquisition and imaging method for stepped frequency GPRs’*IEEE Trans. Signal Process.*, 2009, **57**, (7), pp. 2640–2650.

18 Lagunas, E., Amin, M.G., Ahmad, F., Nájar, M.: ‘Joint wall mitigation and compressive sensing for indoor image reconstruction’*IEEE Trans. Geosci. Remote Sens.*, 2013, **51**, (2), pp. 891–906.

19 Tang, V.H., Bouzerdoum, A., Phung, S.L.: ‘Two-stage through-the-wall radar image formation using compressive sensing’*J. Electron. Imaging*, 2013, **22**, (2), p. 21006.

20 Yang, J., Bouzerdoum, A., Tivive, F.H.C., Amin, M.G.: ‘Multiple-measurement vector model and its application to through-the-wall radar imaging’*ICASSP, IEEE Int. Conf. Acoust. Speech Signal Process. - Proc.*, 2011, pp. 2672–2675.

21 Tang, V.H., Bouzerdoum, A., Phung, S.L., Tivive, F.H.C.: ‘Enhanced through-the-wall radar imaging using Bayesian compressive sensing’*Compressive Sens. Ii*, 2013, **8717**, pp. 1–12.

22 Patel, V., Easley, G.: ‘Compressed synthetic aperture radar’*IEEE J. Sel. Top. Signal Process.*, 2010, **4**, (2), pp. 244–254.

23 Duman, M., Gurbuz, A.C.: ‘Analysis of compressive sensing based through the wall imaging’*2012 IEEE Radar Conf.*, 2012, pp. 0641–0646.

24 Duman, M., Gurbuz, A.C.: ‘Performance analysis of compressive-sensing-based through-the-wall imaging with effect of unknown parameters’*Int. J. Antennas Propag.*, 2012, **2012**.

25 He, L., Carin, L.: ‘Exploiting structure in wavelet-based bayesian compressive sensing’*IEEE Trans. Signal Process.*, 2009, **57**, (9), pp. 3488–3497.

26 Parker, J.T., Ieee, M.: ‘Sparsity and Compressed Sensing in Radar Imaging’2010, **98**, (6).

27 Cai, T.T., Wang, L.: ‘Orthogonal matching pursuit for sparse signal recovery with noise’*IEEE Trans. Inf. Theory*, 2011, **57**, (7), pp. 4680–4688.

28 Huan, Y., Wang, J., Tan, Z., Liu, X., Yu, W.: ‘Random-Frequency SAR Imaging based on compressed sensing’*Int. Geosci. Remote Sens. Symp.*, 2011, **51**, (2), pp. 1674–1677.

29 Ahmad, F., Qian, J., Amin, M.G.: ‘Wall mitigation using discrete prolate spheroidal sequences for sparse indoor image reconstruction’*Eur. Signal Process. Conf.*, 2013, **53**, (3), pp. 1549–1557.

30 Setlur, P., Alli, G., Nuzzo, L., *et al.*: 'Multipath Exploitation in Through-the-Wall Radar Imaging using Sparse Reconstruction'*IEEE Trans. Aerosp. Electron. Syst.*, 2014, **50**, (2), pp. 920–939.

31 Xu, J., Pi, Y., Cao, Z.: 'Bayesian compressive sensing in synthetic aperture radar imaging'*IET Radar, Sonar Navig.*, 2012, **6**, (1), pp. 2–8.

32 Wu, Q., Zhang, Y.D., Amin, M.G., Ahmad, F.: 'Through-the-wall radar imaging based on modified Bayesian compressive sensing'*2014 IEEE China Summit Int. Conf. Signal Inf. Process. IEEE ChinaSIP 2014 - Proc.*, 2014, pp. 232–236.

33 Bouzerdoum, A., Tivive, F.H.C., Tang, V.H.: 'Multi-polarization through-the-wall radar imaging using joint Bayesian compressed sensing', in 'International Conference on Digital Signal Processing, DSP' (2014), pp. 783–788

34 Donoho, D.L.: 'Compressed sensing'*IEEE Trans. Inf. Theory*, 2006, **52**, (4), pp. 1289–1306.

35 Candès, E., Romberg, J.: 'Sparsity and incoherence in compressive sampling'*Inverse Probl.*, 2007, **23**, (3), pp. 969–985.

36 Donoho, D.L., Tsaig, Y., Drori, I., Starck, J.L.: 'Sparse solution of

underdetermined systems of linear equations by stagewise orthogonal matching pursuit'*IEEE Trans. Inf. Theory*, 2012, **58**, (2), pp. 1094–1121.

37 Candes, E.J., Romberg, J., Tao, T.: 'Robust uncertainty principles: exact signal reconstruction from highly incomplete frequency information'*IEEE Trans. Inf. Theory*, 2006, **52**, (2), pp. 489–509.

38 Yoon, Y.-S., Amin, M.: 'Compressed sensing technique for high-resolution radar imaging'*Proc. SPIE Signal Process. Sens. Fusion Target Recognit. XVII*, 2008, **6968**, (1).

39 Gurbuz, A.C., McClellan, J.H., Scott, W.R.: 'A compressive sensing data acquisition and imaging method for stepped frequency GPRs'*IEEE Trans. Signal Process.*, 2009, **57**, (7), pp. 2640–2650.

40 Candès, E.J., Romberg, J.K., Tao, T.: 'Stable signal recovery from incomplete and inaccurate measurements'*Commun. Pure Appl. Math.*, 2006, **59**, (8), pp. 1207–1223.

41 Ji, S., Xue, Y., Carin, L.: 'Bayesian compressive sensing'*IEEE Trans. Signal Process.*, 2008, **56**, (6), pp. 2346–2356.

42 Wipf, D.P., Rao, B.D.: 'Sparse Bayesian learning for basis selection'*Signal Process. IEEE Trans.*, 2004, **52**, (8), pp. 2153–2164.

43 Wipf, D.P.: 'Bayesian Methods for Finding Sparse Representations'. University of California San Diego, 2006

44 Wipf, D., Nagarajan, S.: 'Iterative Reweighted –l1 and –l2 Methods for Finding Sparse Solutions'*IEEE J. Sel. Top. Signal …*, 2010, **4**, (2), pp. 317–329.

45 Wipf, D.P., Rao, B.D., Nagarajan, S.: 'Latent Variable Bayesian Models for Promoting Sparsity'*IEEE Trans. Inf. Theory*, 2011, **57**, (9), pp. 6236–6255.

46 Wipf, D.P.: 'Sparse Estimation with Structured Dictionaries', in 'Proceedings of the 24th International Conference on Neural Information Processing Systems' (Curran Associates Inc., 2011), pp. 2016–2024

47 Masood, M., Al-Naffouri, T.Y.: 'Sparse reconstruction using distribution agnostic bayesian matching pursuit'*IEEE Trans. Signal Process.*, 2013, **61**, (21), pp. 5298–5309.

48 Zhang, Z., Rao, B.D.: 'Extension of SBL Algorithms for the Recovery of Block Sparse Signals With Intra-Block Correlation'*IEEE Trans. Signal Process.*, 2013, **61**, (8), pp. 2009–2015.

49 Zhang, Z., Rao, B.D.: 'Recovery of block sparse signals using the framework of block sparse Bayesian learning', in '2012 IEEE International Conference

on Acoustics, Speech and Signal Processing (ICASSP)' (2012), pp. 3345–3348

50 Zhang, Z., Jung, T.P., Makeig, S., Rao, B.D.: 'Compressed Sensing for Energy-Efficient Wireless Telemonitoring of Noninvasive Fetal ECG Via Block Sparse Bayesian Learning'*IEEE Trans. Biomed. Eng.*, 2013, **60**, (2), pp. 300–309.

51 Zhang, Z., Rao, B.D.: 'Sparse signal recovery in the presence of correlated multiple measurement vectors', in '2010 IEEE International Conference on Acoustics, Speech and Signal Processing' (2010), pp. 3986–3989

52 Wan, J., Zhang, Z., Yan, J., *et al.*: 'Sparse Bayesian multi-task learning for predicting cognitive outcomes from neuroimaging measures in Alzheimer's disease', in '2012 IEEE Conference on Computer Vision and Pattern Recognition' (2012), pp. 940–947

53 Zhang, Z., Rao, B.D.: 'Iterative reweighted algorithms for sparse signal recovery with temporally correlated source vectors', in '2011 IEEE International Conference on Acoustics, Speech and Signal Processing (ICASSP)' (2011), pp. 3932–3935

54 Zhang, Z., Rao, B.D.: 'Sparse Signal Recovery With Temporally Correlated Source Vectors Using Sparse Bayesian Learning'*IEEE J. Sel. Top. Signal*

*Process.*, 2011, **5**, (5), pp. 912–926.

55 Zhang, Z., Jung, T.P., Makeig, S., Pi, Z., Rao, B.D.: ‘Spatiotemporal Sparse Bayesian Learning With Applications to Compressed Sensing of Multichannel Physiological Signals’*IEEE Trans. Neural Syst. Rehabil. Eng.*, 2014, **22**, (6), pp. 1186–1197.

56 Masood, M., Afify, L.H., Al-Naffouri, T.Y.: ‘Efficient coordinated recovery of sparse channels in massive MIMO’*IEEE Trans. Signal Process.*, 2015, **63**, (1), pp. 104–118.

57 Zhang, Z., Jung, T.P., Makeig, S., Rao, B.D.: ‘Compressed Sensing of EEG for Wireless Telemonitoring With Low Energy Consumption and Inexpensive Hardware’*IEEE Trans. Biomed. Eng.*, 2013, **60**, (1), pp. 221–224.

58 Qin, S., Zhang, Y., Amin, M.: ‘Generalized Coprime Array Configurations for Direction-of-Arrival Estimation’*Signal Process. IEEE …*, 2015, **63**, (6), pp. 1377–1390.

59 Cohen, S.: ‘Compressive Sensing With Highly Coherent Dictionaries’2012, pp. 1–30.

60 Wipf, D.P., Owen, J.P., Attias, H.T., Sekihara, K., Nagarajan, S.S.: ‘Robust Bayesian estimation of the location, orientation, and time course of multiple

correlated neural sources using MEG'*Neuroimage*, 2010, **49**, (1), pp. 641–655.

61 M.E. Tipping, An.F. (Microsoft R.: 'Fast Marginal Likelihood Maximization for Sparse Bayesian Models'*Igarss 2014*, 2003, (1), pp. 1–5.

62 Ji, S., Xue, Y., Carin, L.: 'Bayesian Compressive Sensing'*IEEE Trans. Signal Process.*, 2008, **56**, (6), pp. 2346–2356.

63 Schniter, P., Potter, L.C., Ziniel, J.: 'Fast bayesian matching pursuit'*2008 Inf. Theory Appl. Work. - Conf. Proceedings, ITA*, 2008, pp. 326–332.

64 Schniter, P., Potter, L.C., Ziniel, J.: 'Fast Bayesian Matching Pursuit: Model Uncertainty and Parameter Estimation for Sparse Linear Models'*IEEE Trans. Signal Process. to be Publ.*, 2009.

65 Masood, M., Al-Naffouri, T.: 'Sparse Reconstruction Using Distribution Agnostic Bayesian Matching Pursuit'*Signal Process. IEEE Trans.*, 2013, **61**, (21), pp. 5298–5309.

66 Alkhodary, M.T.. A.H.M.: 'Low Complexity Sparse Bayesian Estimation for UWB Radar Imaging'*Submitt. to IET Radar, Sonar Navig.*, 2017.

67 Wipf, D.P., Rao, B.D.: 'An Empirical Bayesian Strategy for Solving the

Simultaneous Sparse Approximation Problem'*IEEE Trans. Signal Process.*, 2007, **55**, (7), pp. 3704–3716.

68 Muqaibel, A.H., Abdalla, A.T., Alkhodary, M.T., Alawsh, S.A.: 'Through-the-wall radar imaging exploiting Pythagorean apertures with sparse reconstruction'*Digit. Signal Process.*, 2017, **61**, pp. 86–96.

69 Alkhodary, M.T.. A.H.M.: 'Cooperative Bayesian Estimation for Compressed Indoor Radar Imaging'*to be Submitt. to IEEE Trans. Geosci. Remote Sens.*, no date.

70 AlKhodary, M.T., Abozaid, S., Muqaibel, A.H.: 'Experimental Evaluation of UWB Indoor Radar Imaging', in 'IEEE Asia-Pacific Conference on Applied Electromagnetics (APACE2016)' (2016)

71 Amin, M.G., Ahmad, F.: 'Wideband synthetic aperture beamforming for through-the-wall imaging [Lecture Notes]'*IEEE Signal Process. Mag.*, 2008, **25**, (4), pp. 110–113.

72 Ahmad, F., Amin, M.G., Kassam, S.A.: 'Synthetic aperture beamformer for imaging through a dielectric wall'*IEEE Trans. Aerosp. Electron. Syst.*, 2005, **41**, (1), pp. 271–283.

73 Ahmad, F., Amin, M.G., Kassam, S.A., Frazer, G.J.: 'A wideband, synthetic

aperture beamformer for through-the-wall imaging', in 'IEEE International Symposium on Phased Array Systems and Technology, 2003.' (IEEE, no date), pp. 187–192

74 Amine, M. (Ed.): 'Through-the-Wall Radar Imaging' (CRC Press, 2011)

75 Setlur, P., Amin, M., Ahmad, F., Member, S.: 'Multipath model and exploitation in through-the-wall and urban radar sensing'*IEEE Trans. Geosci. Remote Sens.*, 2011, **49**, (10), pp. 4021–4034.

76 Yoon, Y.-S., Amin, M.G.: 'Spatial Filtering for Wall-Clutter Mitigation in Through-the-Wall Radar Imaging'*Geosci. Remote Sensing, IEEE Trans.*, 2009, **47**, (9), pp. 3192–3208.

77 Gennarelli, G., Vivone, G., Braca, P., Soldovieri, F., Amin, M.G.: 'Multiple Extended Target Tracking for Through-Wall Radars'*IEEE Trans. Geosci. Remote Sens.*, 2015, **53**, (12), pp. 6482–6494.

78 Y.-S. Yoon and M. Amin: 'High resolution through-the-wall radar imaging using extended target model', in 'Radar Conference, 2008. RADAR '08. IEEE' (2008), pp. 1–4

79 Yoon, Y.S., Amin, M.G.: 'High resolution through-the-wall radar imaging using extended target model'*2008 IEEE Radar Conf. RADAR 2008*, 2008.

80 Ahmed, F., Amin, M.G.M.G., Kassam, S.S.A., Ahmad, F., Amin, M.G.M.G., Kassam, S.S.A.: ‘A Beamforming Approach to Stepped-Frequency Synthetic Aperture Through-The-Wall Radar Imaging’, in ‘1st IEEE International Workshop on Computational Advances in Multi-Sensor Adaptive Processing, 2005.’ (IEEE, 2005), pp. 24–27

81 Yoon, Y.-S.Y.-S., Amin, M.G., Y.-S. Yoon and M. Amin, *et al.*: ‘Compressed sensing technique for high-resolution radar imaging’*Proc. SPIE*, 2008, **6968**, (69681), p. 69681A–69681A–10.

82 Vu, D., Xu, L., Xue, M., Li, J.: ‘Nonparametric missing sample spectral analysis and its applications to interrupted SAR’*IEEE J. Sel. Top. Signal Process.*, 2012, **6**, (1), pp. 1–14.

83 Tan, X., Roberts, W., Li, J., Stoica, P.: ‘Sparse learning via iterative minimization with application to MIMO radar imaging’*IEEE Trans. Signal Process.*, 2011, **59**, (3), pp. 1088–1101.

84 Youwen, Z., Diya, W., Tong, W.: ‘Low Complexity Orthogonal Matching Pursuit Algorithm for High-Resolution Imaging Sonar’2016, (1), pp. 0–5.

85 Amin, M.G., Ahmad, F.: ‘Compressive sensing for through-the-wall radar imaging’*J. Electron. Imaging*, 2013, **22**, (3).

86 Alkhodary, M.T., Muqaibel, A.H.: ‘Efficient grouping technique for low mutual-coherence basis matrix in radar imaging’*Electron. Lett.*, 2017, **53**, (2).

87 Yoon, Y.-S., Amin, M.: ‘Spatial filtering for wall-clutter mitigation in through-the-wall radar imaging’*IEEE Trans. Geosci. Remote Sens.*, 2009, **47**, (9), pp. 3192–3208.

88 Leigsnering, M., Amin, M.G., Ahmad, F., Zoubir, A.M.: ‘Multipath exploitation and suppression for SAR imaging of building interiors [An overview of recent advances]’*Signal Process. Mag. IEEE*, 2014, **vol.31**, (4), pp. 110–119.

89 Donoho, D.L., Elad, M.: ‘Optimally sparse representation in general (nonorthogonal) dictionaries via l minimization.’*Proc. Natl. Acad. Sci. U. S. A.*, 2003, **100**, (5), pp. 2197–2202.

90 Browne, K.E., Burkholder, R.J., Volakis, J.L.: ‘Fast optimization of through-wall radar images via the method of lagrange multipliers’*IEEE Trans. Antennas Propag.*, 2013, **61**, (1), pp. 320–328.

91 Patel, V.M., Member, S., Easley, G.R., Healy, D.M.: ‘Compressed Synthetic Aperture Radar’*IEEE J. Sel. Top. Signal Process.*, 2010, **4**, (2), pp. 244–

254.

92 Tang, V.H., Phung, S.L.: ‘Multi-view TWRI scene reconstruction using a joint Bayesian sparse approximation model’2015.

93 Wu, Q., Zhang, Y.D., Amin, M.G., Himed, B.: ‘Multi-static passive SAR imaging based on Bayesian compressive sensing’*SPIE Proc.*, 2014, **9109**, p. 910902.

94 Ren, X.Z., Chen, L.N.: ‘Four-dimensional SAR imaging algorithm using Bayesian compressive sensing’*J. Electromagn. Waves Appl.*, 2014, **28**, (13), pp. 1661–1676.

95 Wu, Q., Zhang, Y.D., Amin, M.G., Himed, B.: ‘Complex multitask Bayesian compressive sensing’, in ‘ICASSP, IEEE International Conference on Acoustics, Speech and Signal Processing - Proceedings’ (2014), pp. 3375–3379

96 Hamran, S.E.: ‘Radar Performance of Ultra Wideband Waveforms’, in Kounemou, G. (Ed.): ‘Radar Technology’ (INTECH, 2009)

97 Zhang, W., Amin, M.G., Ahmad, F., Hoorfar, A., Smith, G.E.: ‘Ultrawideband impulse radar through-the-wall imaging with compressive sensing’*Int. J. Antennas Propag.*, 2012, **2012**.

98 Oyan, M.J., Hamran, S.-E., Hanssen, L., Berger, T., Plettemeier, D.: ‘Ultrawideband Gated Step Frequency Ground-Penetrating Radar’*Geosci. Remote Sensing, IEEE Trans.*, 2012, **50**, (1), pp. 212–220.

99 Raimundo, X.: ‘FMCW Signals for Radar Imaging and Channel Sounding’. Durham University, 2015

100 Lagunas, E.: ‘Compressive Sensing Based Candidate Detector and its Applications to Spectrum Sensing and Through-the-Wall Radar Imaging’2014, (September).

101 Nguyen, L.: ‘Image Resolution Computation for Ultra-Wideband (UWB) Synchronous Impulse Reconstruction (SIRE) Radar’ (2007)

102 Teng, Y., Griffiths, H., Baker, C., Woodbridge, K.: ‘Netted radar sensitivity and ambiguity’*IET Radar, Sonar Navig.*, 2007, **1**, pp. 479–486.

103 Tivive, F., Bouzerdoum, A., Moeness, A.: ‘A Subspace Projection Approach for Wall Clutter Mitigation in Through-the-Wall Radar Imaging’*IEEE Trans. Geosci. Remote Sens.*, 2015, **53**, (4), pp. 2108–2122.

104 Tivive, F., Amin, M.G., Bouzerdoum, A.: ‘Wall clutter mitigation based on eigen-analysisin through-the-wall radar imaging’, in ‘Proc. IEEE Workshop on DSP’ (2011), pp. 1–8

105 Leigsnering, M., Ahmad, F., Amin, M., Zoubir, A.: ‘Compressive sensing based specular multipath exploitation for through-the-wall radar imaging’, in ‘IEEE International Conference on Acoustics, Speech and Signal Processing (ICASSP)’ (2013), pp. 6004–6008

106 Lagunas, E., Amin, M.G., Ahmad, F., Nájar, M.: ‘Wall mitigation techniques for indoor sensing within the compressive sensing framework’*IEEE Trans. Geosci. Remote Sens*, 2013, **51**, (2), pp. 891–906.

107 AlBeladi, A.: ‘Multipath exploitation in through-the-wall radar imaging using sparsity-driven detection’. King Fahd University of Petroleum and Minerals, 2015

108 Candes, E.J., Wakin, M.B.: ‘An Introduction To Compressive Sampling’*IEEE Signal Process. Mag.*, 2008, **25**, (2), pp. 21–30.

109 Candès, E.J., Romberg, J., Tao, T.: ‘Robust uncertainty principles: Exact signal reconstruction from highly incomplete frequency information’*IEEE Trans. Inf. Theory*, 2006, **52**, (2), pp. 489–509.

110 Kutyniok, G.: ‘Theory and Applications of Compressed Sensing’*Pre-Print*, 2012, (July), p. 22.

111 Donoho, D.L.: ‘Compressed sensing’*IEEE Trans. Inf. Theory*, 2006, **52**, (4),

pp. 1289–1306.

112 Chen, S.S., Donoho, D.L., Saunders, M.A.: 'Atomic Decomposition by Basis Pursuit'*SIAM J. Sci. Comput.*, 1998, **20**, (1), pp. 33–61.

113 Tropp, J., Gilbert, A.: 'Signal recovery from random measurements via orthogonal matching pursuit'*IEEE Trans. Inf. Theory*, 2007, **53**, (12), pp. 4655–4666.

114 Elad, M.: 'Optimized projections for compressed sensing'*IEEE Trans. Signal Process.*, 2007, **55**, (12), pp. 5695–5702.

115 Candes, E.J., Tao, T.: 'Near-optimal signal recovery from random projections: Universal encoding strategies'*IEEE Trans. Inf. Theory*, 2006, **52**, (12), pp. 5406–5425.

116 Candes, E.J., Eldar, Y.C., Needell, D., Randall, P.: 'Compressed Sensing with Coherent and Redundant Dictionaries'2010.

117 Schniter, P., Potter, L.C., Ziniel, J.: 'Fast bayesian matching pursuit'*2008 Inf. Theory Appl. Work. - Conf. Proceedings, ITA*, 2008, (January), pp. 326–332.

118 Muqaibel, A.H., Abdalla, A.T., Al-dharrab, S.: 'Aspect Dependent Efficient

Multipath Ghost Suppression in Through the Wall Radar with Compressive Sensing'*J. Radioengineerring,submitted*, 2014.

119 Tang, V.H., Bouzerdoum, A., Phung, S.L., Tivive, F.H.C.: 'Enhanced Wall Clutter Mitigation for Compressed through-the-Wall Radar Imaging Using Joint Bayesian Sparse Signal Recovery'2014, pp. 7854–7858.

120 Lagunas, E., Amin, M.G., Ahmad, F., Nájar, M.: 'Wall mitigation techniques for indoor sensing within the compressive sensing framework'*Proc. IEEE Sens. Array Multichannel Signal Process. Work.*, 2012, pp. 213–216.

121 Keichel, W., Dilsavor, R., Amin, M., *et al.*: 'Experiments on Wideband Through the Wall Imaging'*roc. SPIE Symp. Def. Secur. Algorithms Synth. Aperture Radar Imag. XII Conf.*, 2005, **5808**, p. 196–209 Vol. 5808.

122 Peabody Jr, J.E., Charvat, G.L., Goodwin, J., Tobias, M.: 'Through-Wall Imaging Radar'*Lincoln Lab. J.*, 2012, **19**, (1).

123 Debes, C., Amin, M.G., Zoubir, A.M.: 'Target detection in single- and multiple-view through-the-wall radar imaging'*IEEE Trans. Geosci. Remote Sens.*, 2009, **47**, (5), pp. 1349–1361.

124 Maaref, N., Millot, P.: 'Array-Based Ultrawideband through-Wall Radar : Prediction and Assessment of Real Radar Abilities'2013, **2013**.

125 Abdalla, A.T., Alkhodary, M.T., Muqaibel, A.H.: ‘Extended Targets Modelling and Block Agnostic Sparse Reconstruction in Through-the-Wall Radar Imaging: A Different Perspective’*Submitt. to IET Radar, Sonar Navig.*, 2017.

126 Wang, H., Ping, L., Lin, X.: ‘Gain from Antenna Correlation in Multi-User MIMO Systems’*Proc. Inf. Theory Appl.(ITA) Work.*, 2010, pp. 1–5.

# Vitae

Full Name : Mohammad Tamim Alkhodary

Nationality : Syrian

Date of Birth : 28/11/1985

Email : mohamd2020@hotmail.com

Address : Saudi Arabia, Dhahran

Academic Background : MSc. In Telecommunications, King Fahd University of Petroleum and Minerals, Saudi Arabia, 2012

Research Interest : Radar Imaging, Signal processing, UWB communication, Compressive Sensing theory and applications.

Experience : Alkhodary has joined the electrical engineering department at KFUPM as a lecturer in 2012. In 2015 he joined KAUST for one-year research internship. In 2017 he joined Georgia Tech as a visiting scholar for three months.